STRUCTURAL ANALYSIS, LAYER THICKNESS MEASUREMENTS AND MINERALOGICAL INVESTIGATION OF THE LARGE INTERIOR LAYERED DEPOSIT WITHIN GANGES CHASMA, VALLES MARINERIS, MARS

Alicia Hore, BSc. (Hons.)

MSc, Earth Sciences

Submitted in partial fulfillment
of the requirements for the degree of

Master of Science

Faculty of Earth Sciences, Brock University
St. Catharines, Ontario

Abstract

The interior layered deposit (ILD) in Ganges Chasma, Valles Marineris, is a 4.25 km high mound that extends approximately 110 km from west to east. The deposition, deformation, and erosion history of the Ganges ILD records aids in identifying the processes that formed and shaped the Chasma. To interpret structural and geomorphic processes acting on the ILD, multiple layer attitudes and layer thickness transects were conducted on the Ganges ILD. Mineralogical data was analyzed to determine correlations between materials and landforms.

Layer thickness measurements indicate that the majority of layers are between 0.5 m and 4 m throughout the ILD. Three major benches dominate the Ganges ILD. Layer thicknesses increase at the ILD benches, suggesting that the benches are formed from the gradual thickening of layers. This indicates that the benches are depositional features draping over basement topography. Layer attitudes indicate overall shallow dips generally confined to a North-South direction that locally appear to follow bench topography.

Layering is disrupted on a scale of 40 m to 150 m in 12 separate locations throughout the ILD. In all locations, underlying layering is disturbed by overlying folded layers in a trough-like geometry. These features are interpreted to have formed as submarine channels in a lacustrine setting, subsequently infilled by sediments. Subsequently, the channels were eroded to the present topography, resulting in the thin, curved layering observed.

Data cannot conclusively support one ILD formation hypothesis, but does indicate that the Ganges ILD postdates Chasma formation. The presence of water altered minerals, consistently thin layering, and layer orientations provide strong evidence that the ILD formed in a lacustrine setting.

Acknowledgements

During the data collection and writing stages of this report, I received guidance and support that I am extremely grateful for from Dr. Frank Fueten, Dr. Rick Cheel, and Dr. Robert Stesky. I would also like to thank Dr. Jessica Flahaut for the processed CRISM and mineralogical data pertaining to the Ganges Chasma ILD.

Table of Contents

List of Tables

Chapter 2

Chapter 3

List of Figures

Chapter 1

Chapter 2

Chapter 3

List of Abbreviations

CRISM	Compact Reconnaissance Imaging Spectrometer
CTX	Context Imager
HiRISE	High Resolution Imaging Science Experiment
HRSC	High Resolution Stereo Camera
ILD	Interior Layered Deposit
OMEGA	Observatoire pour la Mineralogie, L'Eau, les Glaces et l'Activitié
TES	Thermal Emission Spectrometer
VM	Valles Marineris

Chapter 1

1.1 Introduction

Mars' close proximity to Earth and potential habitability by terrestrial standards makes it an important research subject in planetary science. The discovery of ice and erosional fluvial features by orbiters, landers and rovers studying the Martin surface has significantly increased the interest of Martian studies.

The geology of the Martian surface is divided into three age epochs: Noachian, the oldest, which ranges in age from 4.55 to 3.7 Gyr ago, Hesperian, which ranges in age from 3.7 to 3.0 Gyr ago, and Amazonian, the youngest, which ranges from ~3.0 Gyr to present [*Hartmann and Neukum,* 2001; *Chapman and Smellie,* 2007] (Figure 1.1). The relative ages of this system are based on the number of impact craters that mark the surface; the more impact craters present, the older the surface is [*Chapman and Smellie,* 2007].

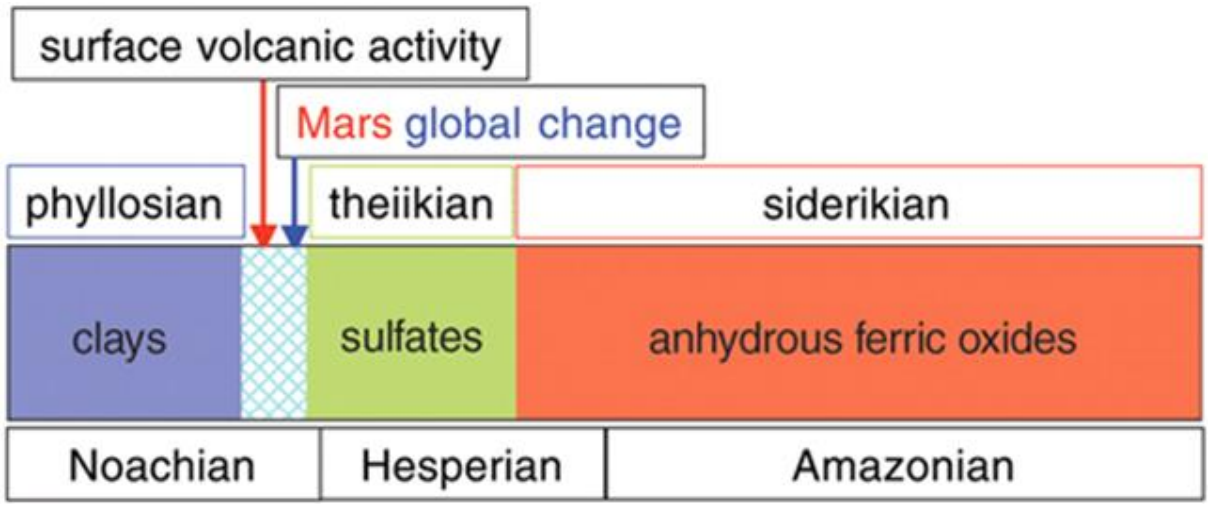

Figure 1.1: The three age systems defined in the Mars timescale and the mineralogical compositions associated with each [*Bibring et al.,* 2006].

The Tharsis region, a broad volcanic topographic high approximately 8000 km across [*Carr,* 1980], dominates the topography in the western Mars hemisphere [*Andrews-Hanna et al.,*

2007]. This area, formed through a combination of intrusive and extrusive volcanism during the Noachian epoch, played a key role in the global geodynamic and hydrologic evolution [*Andrews-Hanna et al.*, 2007]. As part of the Tharsis region (Figure 1.2), it is likely that the Tharsis construction played a key role in the development of the VM canyon system [*Andrews-Hanna et al.*, 2007].

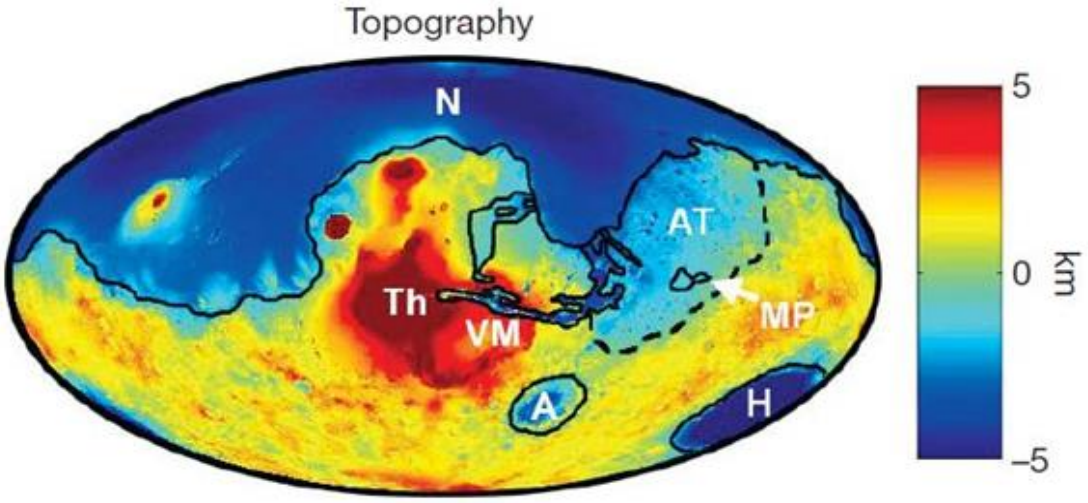

Figure 1.2: Topography of Mars from the Mars Orbiter Laser Altimeter, MOLA. Major features outlined are: Tharsis (Th), Valles Marineris (VM), Hellas (H), Argyre (A), the northern lowlands (N), Arabia Terra (AT), and Meridiani Planum (MP) [*Andrews-Hanna et al.*, 2007].

1.2 Valles Marineris Geological History

This study focuses on a portion of VM which is a 4000 km long system of valleys located at the Martian equator [*Harland*, 2005] (Figure 1.3). This system is made up of multiple chasmata or troughs [*Harland*, 2005] that are hundreds of km in length and width and have relief of 10 km or more [*Blasius et al.*, 1977]. The chasma/chasmata that compose the VM system are defined as elongated, deep, steep sided depressions [*IAU and WGPSN*, 2014]. Within the VM

chasmata are enigmatic layered deposits, or Interior Layered Deposits (ILDs) which also have uncertain origins [*Lucchitta et al.,* 1994; *Fueten et al.,* 2011].

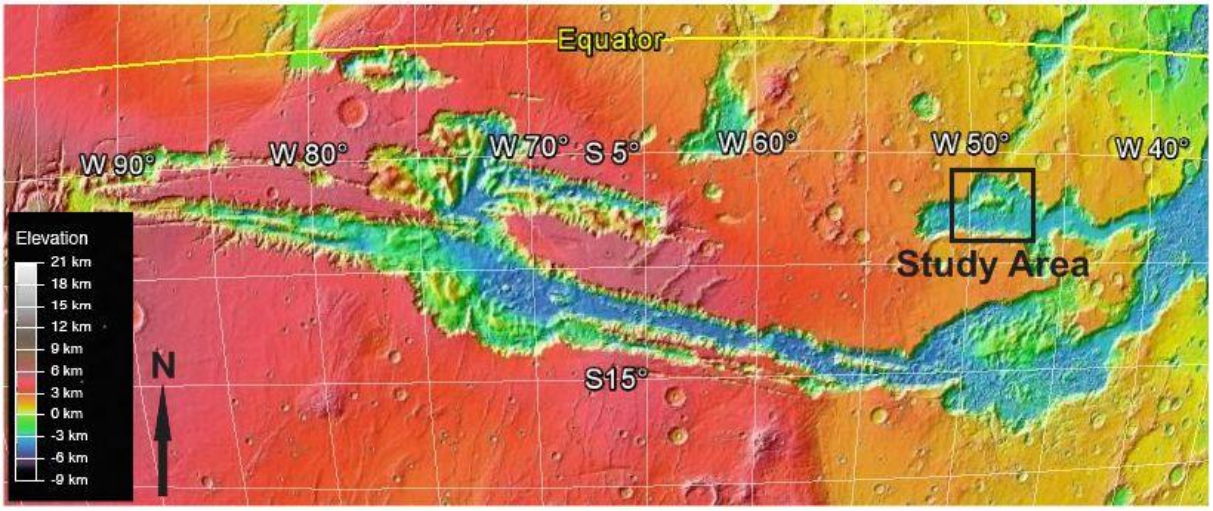

Figure 1.3: MOLA DTM of the Valles Marineris (VM) System. The study area, Ganges Chasma, is indicated by the black box at the eastern edge of the VM system. Image was obtained from Google Earth imagery.

The origin of VM is debated, yet most studies agree that VM began as isolated basins or collapse structures and suggest a tectonic or volcanic formation history [*Lucchitta et al.*, 1994; *Tanaka*, 1997].

1.2.1 Basin Collapse and Linking

Current research indicates that VM was created during a two stage process: 1) ancestral basin formation prior to the opening of VM, and 2) basin connection due to faulting [*Lucchitta et al.*, 1994; *Schultz,* 1998].

Through a combination of collapse [*Lucchitta et al.*, 1994; *Chapman and Smellie*, 2007], subsidence [*Okubo et al*., 2008], and/or structural adjustment, ancestral basins formed along previous structural alignments [*Lucchitta et al.,* 1994]. Regional rift systems developed in the area of VM early in Mars history during the Noachian epoch [*Okubo et al*., 2008]. Later, Tharsis-related stresses [*Chapman and Smellie*, 2007; *Chojnacki and Hynek*, 2008; *Okubo et al.*, 2008]

begun in the late Noachian to early Hesperian [*Fueten et al.*, 2004; *Chapman and Smellie*, 2007; *Okubo et al.*, 2008], may have led to the connection of the ancestral basins with one another [*Lucchitta et al.*, 1994]. Subsequent widening of the basins through erosion and landslides led to their present-day shape and form [*Okubo et al.*, 2008].

Tanaka [1997] supported the collapse and erosion development, based on five criteria: 1) identification of widespread collapse and slump features in troughs where normal faulting would be confined to local interior scarps and narrow plateau grabens [*Tanaka,* 1997]; 2) magma withdrawal and tectonism occurring prior to trough development [*Tanaka,* 1997; *Fueten et al.*, 2004]; 3) the lack of large grabens found in other areas which experienced extension; 4) troughs, chaotic or knobby terrain, outflow channels, and ILDs appear to be temporally and spatially related in the northern plains; and 5) collapse and mass-flow features found in VM typically occur in high relief, volcano-tectonic settings on Mars [*Tanaka,* 1997]. The presence of appropriate crustal materials, erosional and debris transport processes, and triggering mechanisms in VM indicates that large-scale mass movements have occurred [*Tanaka,* 1997].

1.2.2 Tensional Fracturing and Basin Infilling

Tensional fracturing and water-saturated debris removal has also been suggested as a formation mechanism for VM [*Tanaka,* 1997]. Although the present climate of Mars is very cold and dry, there is abundant evidence for a much milder climate during its early history when surface temperatures would be above water's freezing point and liquid precipitation would occur in the mid-latitudes [*Andrews-Hanna et al.*, 2007; *Flahaut et al.*, 2010]. Substantial occurrences of possible fluidization landforms and long-distance transportation, such as chaotic terrains, outflow channels, debris flow, and landslides, are present on Mars [*Tanaka,* 1997], further supporting the idea of liquid water on the early Martian surface.

Mass wasting of wall material and landslides caused chasmata to enlarge to their present forms [*Chojnacki and Hynek,* 2008]. The infilling of sediments creates the mass-wasted materials found at the bottom of the chasma, while volcanic material is found at the top of the plateau [*Lucchitta et al.,* 1994]. The presence of ancestral lakes would explain why emplaced layered deposits are formed from a combination of mass-wasted and volcanic materials [*Lucchitta et al.,* 1994; *Fueten et al.,* 2014]. If these lakes had not been present, or if the VM chasmata connected before lakes could form, the layered deposits would likely also be composed of primarily volcanic material [*Lucchitta et al.*, 1994].

1.3 Interior Layered Deposits

The thick layered deposits that have been identified within numerous craters, inter-crater plains, and in VM chasmata have internal layering and high albedo [*Flahaut et al.,* 2010] (for examples, see Figure 1.4). Within VM, the layered deposits are referred to as Interior Layered Deposits (ILDs) and are widely studied today [e.g. *Flahaut et al.,* 2010] (Figure 1.4). Constructed of horizontal and inclined largely-continuous layers of material, ILDs and flat-topped mesas occur mainly within elliptical chasmata [*Chapman and Smellie,* 2007]. They typically overlie canyon walls and canyon floors, and in some cases show onlap geometry with chaotic terrain in VM [*Komatsu et al.,* 2004]. The ILD layering ranges from a few metres to 10s of metres in thickness and can form hundreds to thousands of metres thick sequences [*Komatsu et al.,* 2004]. A dark capping layer made of fine, unconsolidated material, likely from an aeolian or ash deposit origin, blankets much of the ILD in areas of gentle slope [*Flahaut et al.,* 2010]. Most ILDs are located 1 to 4 km lower than the surrounding canyon rims [*Komatsu et al.,* 2004] and can be clearly distinguished from the surrounding chasma walls due to their fine layering and specific erosional style morphology [*Fueten et al.,* 2006]. Overall, ILDs account for

approximately 17% of the total area of VM and 60% of all chasma deposits [*Lucchitta et al., 1994*]. The VM light-toned layered deposits only account for approximately 5% of the total amount of deposits found in the equatorial regions of Mars [*Chojnacki and Hynek*, 2008].

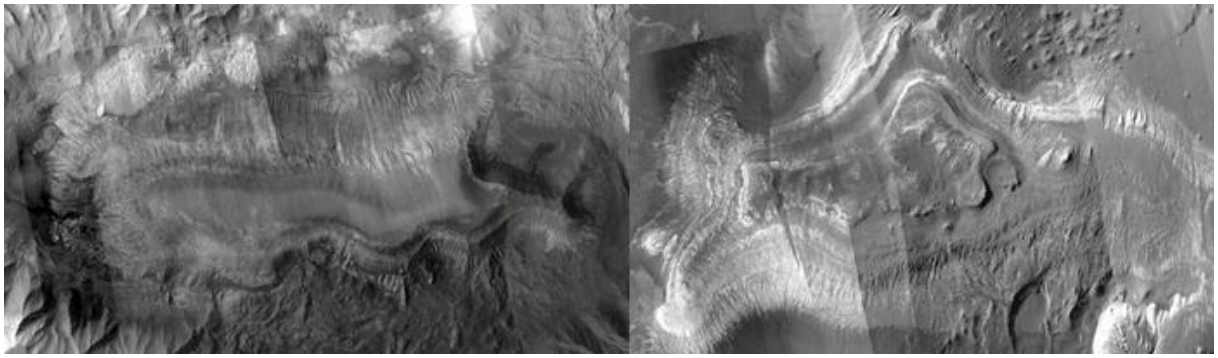

Figure 1.4: Two examples of different ILDs found within VM. Left Image: Hebes ILD; Right Image: Ganges ILD (the focus of this study).

Three classes of outcrop types have been identified, based on visual tone, thickness, texture, and configuration [*Malin and Edgett*, 2000]: 1) layered, 2) massive, and 3) thin mesa. Layered units are thin (a few metres to 200 m) to thick (200-2000 m) units, light to intermediate in tone, and contain 100s of thin beds or sub-units. Massive units are also light to intermediate toned, hundreds of metres to a few kilometres thick, have poor bedding, and in some instances, contain forms that are transitional between layered and massive units. These units are the most common in VM chasmata, especially in Ganges, Ophir, Hebes and Candor chasmata. Lastly, thin mesa units, unlike layered and massive units, consist of dark or intermediate toned mesa-forming materials. Thin mesa units almost always lie over previously eroded massive and/or layered units in smooth, pitted, or intensely ridged surfaces. When these units occur together, massive units always lie above layered units while mesa units are always found on top, indicating a multistage depositional history [*Fueten et al.*, 2006].

The physical attributes, geographical distribution, and Noachian age of the layered and massive units indicate that the processes which deposited the materials originally no longer

occurs on Mars today [*Malin and Edgett*, 2000]. No source regions or transportation paths for the materials are obvious on the Mars surface today [*Malin and Edgett*, 2000]. The mesa units appear to be younger than the Noachian-aged sediments, indicated by their presence on top of eroded layered and massive units [*Malin and Edgett*, 2000]. The draping of the mesa unit over basement topography and VM walls indicates emplacement after chasma formation [*Malin and Edgett*, 2000; *Fueten et al.*, 2011].

1.3.1 Interior Layered Deposits: Formation Mechanisms

That ILDs were emplaced after the connecting of VM basins is the prevailing hypothesis; however, an alternate hypothesis proposes that deposits formed in large impact basins before basin connection in the Noachian epoch and are formed from ancient Martian crust [*Malin and Edgett*, 2000]. Erosional style and layer geometry of ILDs do not support this alternate hypothesis [*Chojnacki and Hynek*, 2008]; geomorphology, geologic mapping and structural analysis studies provide evidence for post-chasma ILD formation [*Okubo et al.*, 2008]. ILD layer variability and stratigraphic sequences [*Komatsu et al.*, 2004] suggest that multiple mechanisms are needed to explain depositional environments and material sources [*Komatsu et al.*, 2004; *Fueten et al.*, 2006]. The majority of ILD layers dip down the topographic slope, possibly suggesting drape morphology over basement topography [*Fueten et al.*, 2006].

Hypotheses for how ILDs form include: subaerial transport [*Malin and Edgett*, 2000; *Fueten et al.*, 2011], subaqueous transport [*Malin and Edgett*, 2000], lacustrine [*Komatsu et al.*, 2004; *Fueten et al.*, 2006; *Chojnacki and Hynek*, 2008; *Flahaut et al.*, 2010], volcanic [*Komatsu et al.*, 2004; *Malin and Edgett*, 2000; *Chojnacki and Hynek*, 2008; *Flahaut et al.*, 2010], sub-ice [*Komatsu et al.*, 2004; *Chojnacki and Hynek*, 2008; *Flahaut et al.*, 2010], aeolian [*Komatsu et al.*, 2004; *Fueten et al.*, 2006; *Chojnacki and Hynek*, 2008; *Flahaut et al.*, 2010], mass wasting

[*Komatsu et al.*, 2004; *Chojnacki and Hynek*, 2008; *Flahaut et al.*, 2010], seasonal snowmelt [*Kite et al.*, 2013; *Fueten et al.*, 2014], and spring deposits [*Pentecost,* 2005; *Rossi et al.,* 2008].

Subaerial and subaqueous transports encompass many different processes. Subaqueous transport processes involve water in alluvial (flowing water), lacustrine (standing water), or deltaic (mixture of flowing and standing water) forms [*Malin and Edgett*, 2000]. Atmospheric and wind effects influence subaerial transport processes include dust storms, dust mantles, volcanic ash fall, impact ejecta, and aeolian processes [*Malin and Edgett,* 2000]. Fine debris is easily transported through the atmosphere and the extensive distribution of light-toned material [*Fueten et al.*, 2011] makes either of these processes likely to have contributed to VM ILDs [*Malin and Edgett,* 2000]. Aerially deposited materials in a wet environment [*Fueten et al.*, 2011] or dry gravity driven flows [*Cheel, Pers. Comm.*, July 2014] can result in the transportation of materials down slope, deposited on the chasma floor in the location of the ILD mounds [*Fueten et al.*, 2011], and subsequently eroded away from the chasma walls.

Volcanic and lacustrine processes appear to be the most plausible mechanisms of ILD emplacement. A lacustrine origin is supported by the horizontal nature of ILD layers and the continuity of bedding seen in the mounds [*Komatsu et al.*, 2004; *Fueten et al.*, 2006; *Chojnacki and Hynek*, 2008; *Flahaut et al.*, 2010]. Some important evidence is lacking that would support lacustrine processes, including: the absence of overland streams, valleys and alluvial processes [*Lucchitta et al.*, 1994; *Malin and Edgett*, 2000], the lack of confining barriers, the separation of ILD from walls by 'moats,' and no clear identifiable shorelines [*Komatsu et al.*, 2004]. Some of the inconsistencies with lacustrine deposition may be explained by erosion, slope processes and depositional history of the area [*Komatsu et al.*, 2004].

Volcanic air fall would account for the draping of sediments over topography [*Komatsu et al.,* 2004; *Chojnacki and Hynek,* 2008; *Flahaut et al.,* 2010] with small silt and clay particles accounting for the majority of draped materials [*Lucchitta et al.,* 1994*; Malin and Edgett,* 2000]. Five main factors support the volcanic origin of ILDs: 1) variable lithologies of different heights and ages; 2) occurrences as massive free-standing mounds; 3) compositions, 4) volcanic/tectonic setting; and 5) low albedo, high competence, and weathering of layers [*Chapman and Smellie,* 2007]. One major issue with the volcanic hypothesis is the very large size of ILDs by terrestrial standards [*Komatsu et al.,* 2004]. The lower atmospheric pressure on Mars causes higher eruption velocities producing deposits in excess of those on Earth [*Komatsu et al.,* 2004; *Malin and Edgett,* 2000], yet no evidence of volcanic vents is observed within the VM system [*Malin and Edgett,* 2000]. Typically, volcanic materials would be localized near the source, but with no visible remnants of volcanic vents within VM, the layered deposits appear too remote from volcanic manifestations to be formed of primarily pyroclastic materials [*Malin and Edgett,* 2000]. The absence of accumulated deposits on plateaus argues against a volcanic origin for ILDs [*Komatsu et al.,* 2004] and indicates a possible impact origin for the apparent airborne sediments [*Cheel, Pers. Comm.,* July 2014]. However, it is possible that plateau deposits were eroded by strong winds and those found in basins were protected by the chasma walls, or that volcanic air fall did not significantly influence ILD formation [*Komatsu et al.,* 2004].

Due to VM's tectonic origin and the similarities between ILDs and Earth glacio-volcanic features, sub-ice processes [*Komatsu et al.,* 2004; *Chojnacki and Hynek,* 2008] and/or sub-ice volcanos [*Chapman and Smellie,* 2007; *Flahaut et al.,* 2010] have been proposed as probable ILD formation processes. Their similarity in composition and morphology to terrestrial basaltic tuyas suggests that ILDs may be formed from sub-ice volcanoes [*Chapman and Smellie,* 2007].

However, if the Mars ILDs are formed primarily through sub-ice processes, the ILD mound shapes would be similar; instead they vary considerably [*Chapman and Smellie,* 2007].

The large number of sand dunes present on and around the ILDs and the additional features thought to be ancient sand dunes support aeolian influence in the area making it likely that similar processes influenced ILD formation [*Komatsu et al.,* 2004; *Fueten et al.,* 2006; *Chojnacki and Hynek,* 2008; *Flahaut et al.,* 2010]. Mass wasting processes have been proposed as possible origin for VM ILDs. These processes have fallen out of favour due to erosional and mineralogical differences between the ILDs and country wall rock [*Komatsu et al.,* 2004; *Chapman and Smellie*, 2007; *Chojnacki and Hynek,* 2008; *Flahaut et al.,* 2010], age and mineralogical discrepancy between ILDs and wall material [*Komatsu et al.,* 2004; *Chapman and Smellie,* 2007], and the limited number of graben-type chasmata found [*Chapman and Smellie,* 2007]. Eroded wall material may have contributed to ILD formation but these materials were not the sole sediment source [*Lucchitta et al.,* 1994; *Komatsu et al.,* 2004].

Spring deposits and seasonal snowmelt have also been proposed for ILD formation mechanisms. Spring deposits consist of chemical precipitates, formed from emerging water or springs, carrying dissolved species which become super-saturated when the water becomes exposed to the ambient atmospheric conditions [*Rossi et al.,* 2008]. In terrestrial settings, these deposits range from several metres to several hundred metres, and up to a few kilometres in relief [*Rossi et al.,* 2008]. The seasonal snowmelt theory considers the seasonal variations in the VM system and implies that the water run-off from seasonal snowmelt contributes to the water formed minerals and geomorphic features [*Kite et al.,* 2013; *Fueten et al.,* 2014].

The diverse stratigraphic sequences seen within the VM deposits suggest diverse depositional environments and sediment sources [*Komatsu et al.,* 1993]. Fluvial action is

theorized to have controlled erosion in the past while slope processes and aeolian deflation appear to be the present controlling factors [*Komatsu et al.,* 2004]. The range of erosional patterns on the ILDs indicates that the materials vary in chemistry, mineralogy, grain size, consolidation, and porosity [*Komatsu et al.,* 2004].

1.4 Water-Altered Mineral Occurrences

Though dust cover is widespread and remote sensing equipment may not be able to detect bedrock composition accurately [*Komatsu et al.,* 2004], three classes of water-altered minerals have been identified within VM: hematite, monohydrated sulfates (kieserite) and polyhydrated sulfates [*Chojnacki and Hynek,* 2008]. These sulfate mineral occurrences are typically associated with the ILDs that occur throughout the VM chasmata [*Gendrin et al.,* 2005; *Chojnacki and Hynek,* 2008].

The widespread occurrence of water-altered minerals such as grey hematite and hydrated sulfates in VM [*Chojnacki and Hynek,* 2008] can be attributed to global atmospheric changes over time and the presence of water as a key formation and alteration mechanism [*Gendrin et al.,* 2005]. Geological evidence indicates an advanced hydrological cycle was supported in Mars early history [*Craddock et al.,* 2013].

Data from the Compact Reconnaissance Imaging Spectrometer (CRISM) [*Wang, Freeman, and Arvidson,* 2008] was used to identify mineral signatures and patterns found on the Ganges ILD using the 1.3-2.5 μm wavelengths [*Gendrin et al.,* 2005]. Hydrated minerals can be identified using the 1.9 μm and 2.2 μm absorption bands, indicating the presence of H_2O and OH [*Milliken et al.,* 2008]. Kieserite, or other monohydrated sulfates, are detected by the presence of the 1.6, 2.1, and 2.4 μm bands [*Gendrin et al.,* 2005; *Chojnacki and Hynek,* 2008], while polyhydrated minerals are detected from the 1.4, 1.9, and 2.4 μ bands [*Gendrin et al.,* 2005].

Figure 1.5 depicts the different spectral signatures of hydrated minerals calculated from CRISM data as observed in Candor Chasma [*Fueten et al.,* 2014].

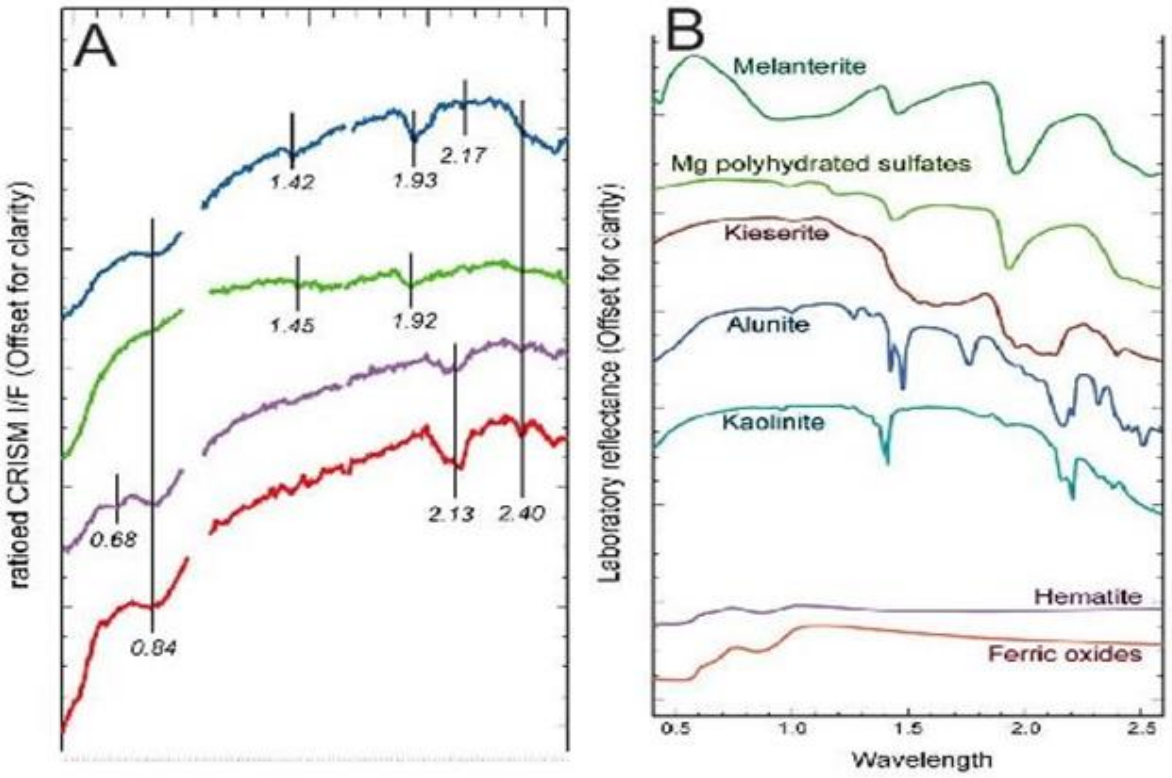

Figure 1.5: A) CRISM ratioed spectra where line markings indicate main absorptions. The 1.4 µm and 1.9 µm bands occur in all minerals containing H_20. The red and purple spectra show strong absorptions at 2.1µm and 2.4 µm. The shift of 1.9 µm to 2.1 µm represents a single H20 molecule and is indicative of Monohydrated Sulfates. The green spectrum is indicative of Polyhydrated Sulfates due to the exact position of the 1.9 µm band and coupling of this band with the 2.4 µm band. The strong decrease from 2.3 µm to 2.5 µm but diagnostic absorptions at 1.44-1.45 µm, 1.93-1.94 µm and 2.4 µm bands create issues with mineralogical identification. This band is most likely a mixture of Mono- and Polyhydrated Sulfates; B) Best library spectral matches given for comparison [*Fueten et al.,* 2014].

Mono- and polyhydrated sulfate deposits occur on steep fluted terrain, flat benches or floors, and buttes [*Chojnacki and Hynek,* 2008]. In VM, kieserite, a monohydrated sulfate, is the most commonly identified mineral [*Chojnacki and Hynek,* 2008]. Kieserite is not stable on the Martian surface where the presence of water ice occurs for long periods of time [*Roach et al.,* 2009; *Fueten et al.,* 2011]. The lack of identified water ice in VM may have led to the high

identification of kieserite in the area. Additionally, monohydrated sulfates generally occur on slopes >5º, at higher elevation ranges, and typically in areas of low dust coverage [*Chojnacki and Hynek,* 2008]. The general identification in areas of low dust coverage could also account for the high identification of kieserite minerals in VM [*Chojnacki and Hynek,* 2008]. Polyhydrated sulfates are generally darker in appearance than other sulfate minerals due to their association with mafic minerals, typically form benches, knobs or hummocky terrains, and are found over a large range of elevations [*Chojnacki and Hynek,* 2008].

Hematite, also a major mineral constituent, is normally detected along the lower flanks of ILDs, on positive relief knobs, and on chasm floor units and is constrained to elevations at or below -2 km [*Chojnacki and Hynek,* 2008]. TES data (for a full description of TES see *Christensen et al*. [1992]) has identified crystalline hematite in central VM, Ganges Chasma [*Chojnacki and Hynek,* 2008], and Eos Chasma, all of which are associated with young dark materials interpreted as having a volcanic origin [*Komatsu et al.,* 2004]. In Ganges, the hematite has sparse outcrops on the ILD, while kieserite minerals have substantial outcrops on the exterior of the ILD [*Chojnacki and Hynek,* 2008]. Along the south flank, hematite deposits occur within an ILD re-entrant or ancient crater formation found at the southern edge of the ILD, just south of H6 [*Chojnacki and Hynek,* 2008].

In VM, the total areal abundance of kieserite, polyhydrated sulfates and hematite are as follows: kieserite= 66% or 10,263 km^2, polyhydrated sulfates= 22% or 3,419 km^2, and hematite= 12% or 1,915 km^2 [*Chojnacki and Hynek,* 2008].

1.4.1 Implications to Global Martian Climate

Liquid water is not stable on the Martian surface under current conditions; nevertheless, in all cases, ILD formation suggests the presence of water [*Flahaut et al.,* 2010]. This conclusion

indicates that ILDs are not currently forming on the Mars surface. Global mineralogy and geomorphology of valley networks provide evidence of a transition from water-abundant conditions where phyllosilicate formation dominated, in the early Noachian epoch, to more arid conditions in the late Noachian and early Hesperian [*Hartmann and Neukum,* 2001; *Andrews-Hanna et al.,* 2007]. These conditions facilitated the formation of layered evaporitic sulfate minerals and diagenetic hematite sediment stacks in Meridiani Planum and associated terrains [*Hartmann and Neukum,* 2001; *Andrews-Hanna et al.,* 2007] such as Valles Marineris.

Valley networks as well as modified impact craters help in the interpretation of past climatic conditions, especially during the Noachian epoch [*Craddock et al.,* 2013]. Valley networks are most commonly cited as evidence for past rainfall and stable liquid water on the Mars surface, but are largely restricted to the end of the Noachian era when climatic conditions would have been optimal [*Craddock et al.,* 2013]. The restriction of valley networks to the equatorial latitudes of Mars also inhibits their usefulness as past climatic conditions whereas impact craters occur at all latitudes [*Craddock et al.,* 2013]. These impact features support the hypotheses that liquid rainfall occurred globally during the Noachian and Hesperian epochs based on the varying degrees of modification seen throughout the craters; modification that is independent from crater size [*Craddock et al.,* 2013]. These modified craters indicate that modification processes were continuously and/or episodically occurring as new craters were continually forming [*Craddock et al.,* 2013]. The occurrence of these craters over the entire Mars surface supports global erosional processes [*Craddock et al.,* 2013].

Outflow channels provide further evidence for the presence of liquid water since they require large releases of water to form and also hint at evidence for an ocean in the northern hemisphere [*Craddock et al.,* 2013]. It is possible that a primordial steam atmosphere controlled

early Mars conditions that then collapsed and precipitated onto the Mars regolith, resulting in lakes and a possible ocean [*Craddock et al.,* 2013]. These water bodies drove a regional hydrological cycle that produced the valley networks seen today [*Craddock et al.*, 2013].

1.4.2 Water-Altered Mineral Formation Hypotheses

Aqueous alteration of Mars lithology results in the formation of sulfate minerals which are important secondary minerals [*Roach et al.*, 2009]. Although a single sulfate-forming mechanism cannot account for all of the sulfate deposits, it is generally agreed that sulfates formed from acid-sulfate weathering of igneous rocks, a process which was likely widespread for the first billion years of Mars history [*Chojnacki and Hynek,* 2008]. They indicate volcanic SO_2 gases or sulfide interactions with crustal materials in the presence of water, possible remnants of a wetter and more acidic early Mars climate [*Roach et al.,* 2009]. The sulfate presence in VM, identified by OMEGA, suggests water as a key component in ILD formation and alteration [*Gendrin et al.,* 2005]. During ILD formation, the possible water which led to the development of sulfate minerals could have been found in many different forms.

Sulfates may form in evaporating bodies of standing water, by precipitation from saturated groundwater, or by acid fog alteration of primary minerals [*Roach et al.,* 2009]. Kite et al. [2013] and Fueten et al. [2014] have suggested that the liquid water needed for sulfate formation was provided during seasonal snowmelt. This model considers the seasonal formation of sulfate minerals by aqueous cementation of aeolian materials and could explain the limited distribution of sulfate materials to specific areas of Mars, such as VM and Terra Meridiani [*Kite et al.,* 2013*; Fueten et al.,* 2014].

Other possible hypotheses explaining various types of sulfate presence in the same deposits are: 1) the conversion of kieserite to a polyhydrated state due to exposure to the surface

environment [*Roach et al.,* 2009], 2) that the sulfates formed elsewhere and subsequently transported through aeolian processes to the ILD [*Roach et al.,* 2009], and/or 3) the chemical weathering of aeolian ash fall by a supply of stagnant water [*Mangold et al.,* 2010; *Fueten et al.,* 2011]. If the primary sulfate material originated from volcanic events, it is likely that sulfur was present in the ash or in the environment at this time [*Fueten et al.,* 2011]. The subsequent alteration of ash deposits into sulfates could lead to sedimentation of the different sulfate deposits at their current locations [*Fueten et al.,* 2011]. It is unlikely that the sulfates were transported through aeolian processes as the cementing process would most likely homogenize the sulfate hydration state; the cementation would make it implausible that there would be distinctions between the locations of the MHS and PHS [*Roach et al.,* 2009].

1.5 Thesis Aims and Goals

This thesis focuses on the geology, geomorphology, and structure of the Ganges Chasma ILD within VM. The studies address two major questions:

1) What does the ILD layering reveal about the formational history of VM ILDs?
2) What information do the irregular sedimentary features of the layering structure provide about the depositional and erosional conditions during formation?

Chapter 2 focuses on the layering that occurs throughout the Ganges ILD. Since ILD formation mechanisms are still inconclusive, understanding the differences in layering throughout an ILD can help draw conclusions about the depositional history of VM ILDs. Measuring the orientations and thicknesses of the ILD layers in Ganges can hopefully reveal patterns leading to the identification of depositional mechanisms. Thickness measurements may reveal an episodic depositional history and numerous depositional mechanisms occurring on the Ganges ILD. Understanding where the sulfate minerals occur on the Ganges ILD will provide

further evidence of the Martian history and help identify which formation mechanisms were present when VM ILDs were formed.

Chapter 3 focuses on large irregular sedimentary features identified within the Ganges ILD. Observations suggest more complicated formation histories for these features that involved erosion of channels, and later infilling. By categorizing the features into three different classes, it is possible to interpret the various shapes in terms of specific forming mechanisms.

Chapter 4 summarizes the results of this work. Using past studies and comparing them to data collected in this study, possible mechanisms can be identified, and mechanisms that led to the formation and deposition of ILDs. The thin layering found throughout the ILD has revealed connections between layering, elevation, bench morphology, and mineralogy. The major presence of sulfates and water-altered minerals suggests the presence of liquid or frozen water during ILD formation and emplacement. The variability of features seen indicate that the Ganges ILD experienced a multistage deformational history.

1.6 References

Andrews-Hanna, J.C., R.J. Phillips, and M.T. Zuber. (2007). Meridiani Planum and the Global Hydrology of Mars, *Nature: Letters, 446*, doi:10.1038/nature05594.

Ansan, V. et al. (2011). Stratigraphy, Mineralogy, and Origin of Layered Deposits inside Terby Crater, Mars, *Icarus, 211*, 273-304, doi:10.1016/j.icarus.2010.09.011.

Bibring, J. P. et al. (2006), Global mineralogical and aqueous Mars history derived from OMEGA/Mars Express data. *Science, 312*, 400–404, doi:10.1126/science.1122659.

Blasius, K.R., J.A. Cutts, J.E. Guest, and H. Masursky. (1977). Geology of the Valles Marineris; first analysis of imaging from the Viking 1 orbiter primary mission, *Journal of Geophysical Research, 82*, 4067–4091.

Carr M.H. (1996). Water on Mars. New York: Oxford University Press

Chapman, M.G., and J.L. Smellie. (2007). Mars Interior Layered Deposits and Terrestrial Sub-Ice Volcanoes Compared: Observations and Interpretations of Similar Geomorphic Characteristics, in *The Geology of Mars: Evidence from Earth-Based Analogs,* pp. 178-210, Cambridge Univ. Press, UK.

Chojnacki, M., and B.M. Hynek. (2008). Geological Context of Water-Altered Minerals in Valles Marineris, Mars, *Journal of Geophysical Research, 113*, E12005, doi: 10.1029/2007JE003070.

Christensen, P. R., et al. (1992). Thermal emission spectrometer experiment: The Mars Observer mission, *Journal of Geophysical Research, 97*, 7719– 7734.

Craddock, R.A., R.P. Irwin III, A.D. Howard, and D.W. Latham. (2013). The History of Water on Early Mars: the Sun, the Wind, and the Rain, *Lunar Planet. Sci. XLIV*, Abstract 1984.

Flahaut, J., C. Quantin, P. Allemand, and P. Thomas. (2010). Morphology and Geology of the ILD in Capri/Eos Chasma (Mars) from Visible and Infrared Data, *Icarus, 207*, 175-185, doi:10.1016/ j.icarus.2009.11.019.

Fueten, F., R.M. Stesky, and P. MacKinnon. (2004). Structural Attitudes of Large Scale Layering in Valles Marineris, Mars, Calculated from Mars Orbiter Laser Altimeter Data and Mars Orbiter Camera Imagery, *Icarus, 175*, 68-77, doi: 10.1016/j.icarus.2004.11.010.

Fueten, F., R. Stesky, P. Mackinnon, E. Hauber, K. Gwinner, F. Scholten, and T. Zegers. (2006). A Structural Study of an Interior Layered Deposit in Southwestern Candor Chasma, Valles Marineris, Mars, Using High Resolution Stereo Camera from Mars Express, *Geophysical Research Letters, 33*, L07202, doi: 10.1029/2005GL025035.

Fueten, F., H. Racher, R. Stesky, P. MacKinnon, E. Hauber, P.C. McGuire, T. Zegers, and K. Gwinner. (2010). Structural Analysis of Interior Layered Deposits in Northern Coprates Chasma, Mars, *Earth and Planetary Science Letters, 294*, 343-356, doi:10.1016/j.epsl.2009.11.004.

Fueten, F., J. Flahaut, L. Le Deit, R. Stesky, E. Hauber, and K. Gwinner. (2011). Interior Layered Deposits within a Perched Basin, Southern Coprates Chasma, Mars: Evidence for their Formation, Alteration, and Erosion, *Journal of Geophysical Research, 116*, E02003, doi: 10.1029/2010JE003695.

Gendrin, A., N. Mangold, J.P. Bibring, Y. Langevin, B. Gondet, F. Poulet, G. Bonello, C. Quantin, J. Mustard, R. Arvidson, and S. LeMouélic. (2005). Sulfates in Martian Layered Terrains: The OMEGA/Mars Express View, *Science, 307*, 1587-1591.

Harland, D.M. (2005). *Water and the Search for Life on Mars,* Praxis Publishing, New York.

Hartmann, W. K. and G. Neukum. (2001). Cratering Chronology and the Evolution of Mars, *Space Science Review*, *96*, 94-165.

International Astronomical Union (IAU) and Working Group for Planetary System Nomenclature (WGPSN). (2014). *Gazetteer of Planetary Nomenclature: Descriptor Terms (Feature Types).* Retrieved from: http://planetarynames.wr.usgs.gov/DescriptorTerms.

Komatsu, G., P.E. Geissler, R.G. Strom, and R.B. Singer. (1993). Stratigraphy and erosional landforms of layered deposits in Valles Marineris, Mars. *Journal of Geophysical Research, 98,* 11, 105–11,121.

Komatsu, G., G.G. Ori, P. Ciarcelluti, and Y.D. Litasov. (2004). Interior Layered Deposits of Valles Marineris, Mars: Analogous Subice Volcanism Related to Baikal Rifting, Southern Siberia, *Planetary and Space Science, 52,* 167-187, doi: 10.1016/j.pss.2003.08.003.

Lucchitta, B.K., N.K. Isbell, and A. Howington-Kraus. (1994). Topography of Valles Marineris: Implications for Erosional and Structural History, *Journal of Geophysical Research, 99 (E2),* 3783-3798.

Malin, M.C., and K.S. Edgett. (2000). Sedimentary Rocks of Early Mars, *Science, 290*, 1927-1937, doi: 10.1126/science.290.5498.1927.

Mangold, N., L. Roach, R. Milliken, S. Le Mouelic, V. Ansan, J. P. Bibring, P. Masson, J. F. Mustard, S. Murchie, and G. Neukum (2010). A Late Amazonian alteration layer related to local volcanism on Mars, *Icarus, 207*, 265–276, doi:10.1016/j.icarus.2009.10.015.

Okubo, C.H., K.H. Lewis, A.S. McEwen, and R.L. Kirk. (2008). Relative Age of Interior Layered Deposits in Southwest Candor Chasma Based on High-Resolution Structural Mapping, *Journal of Geophysical Research, 113*, E12002, doi: 10.1029/2008JE003181.

Roach, L.H., J.F. Mustard, S.L. Murchie, J.P. Bibring, F. Forget, K.W. Lewis, O. Aharonson, M. Vincedon, and J.L. Bishop. (2009). Testing Evidence of Recent Hydration State Change in Sulfates on Mars, *Journal of Geophysical Research, 114*, E00D02, doi: 10.1029é2008JE003245.

Schultz, R.A. (1998). Multiple-process origin of Valles Marineris basins and troughs, Mars. *Planetary Space Science, 46*, 827–834.

Tanaka, K.L. (1997). Origin of Valles Marineris and Noctis Labyrinthus, Mars, by Structurally Controlled Collapse and Erosion of Crustal Materials, *Lunar Planet. Sci. XXVIII*, Abstract 1169.

Chapter 2: Ganges ILD Layer Thickness and Orientation Analysis: Implications for ILD Formation and Deposition

2.1 Introduction

The origin of VM is still debated and several hypotheses for its formation have been proposed. Presently, the majority of studies agree that VM began as grabens, ancestral basins [*Lucchitta, et al.*, 1994], or collapse structures [*Schultz*, 1998] which likely began in the Hesperian (3.7 to 3.0 Gyr ago) or possibly Late Noachian (4.55 to 3.7 Gyr ago) epochs [*Tanaka*, 1997; *Schultz*, 1998; *Chapman and Smellie*, 2007; *Okubo, et al.*, 2008].

Thick deposits, referred to as Interior Layered Deposits (ILDs), have been identified in many chasmata of VM and exhibit internal layering and high albedo [*Lucchitta, et al.*, 1994]. Hypotheses for how the ILDs formed vary greatly but most suggest that ILD placement occurred after trough opening [*Lucchitta, et al.*, 1994; *Chojnacki and Hynek*, 2008]. All of the hypotheses for ILD formation suggest that liquid water was present either on the surface or subsurface [*Flahaut, et al.*, 2010] resulting in the widespread occurrences of water-altered minerals [*Chojnacki and Hynek*, 2008].

This study aims to analyze the layering of one of these infill deposits within the Ganges Chasma near the eastern end of the VM canyon system (Figure 2.1) in order to interpret their depositional mechanisms.

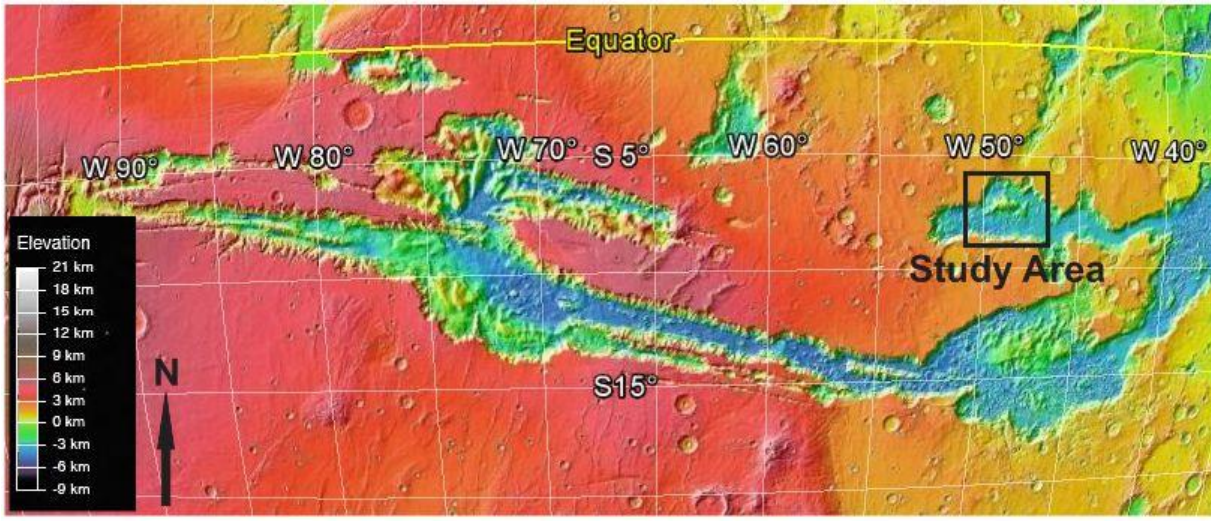

Figure 2.1: MOLA DTM of the Valles Marineris system. The study area, Ganges Chasma, is identified by the black box at the eastern edge of VM. Image obtained from Google Earth

2.2 Geological Background of Ganges ILD

Ganges Chasma (Figure 2.2) is located on the eastern end of VM is a large canyon and has one apparent outflow channel at the northern edge. The Chasma extends approximately 700 km from west to east and ranges in width from 50 to 170 km [*Fenton, et al.*, 2012]; it is approximately 6 km in depth. The potential closure of the narrow outflow channel makes Ganges Chasma a good candidate for a past ancestral basin [*Lucchitta, et al.*, 1994; *Fueten, et al*., 2011; *Ismailos, et al.*, 2012]. A single large ILD is located in the central portion of the chasma with an estimated base elevation of approximately -4000 m with the top estimated at 250 m [*Ismailos, et al.*, 2012] making it a 4.25 km high mound. These elevations are based on the Mars zero-elevation, or areoid [*NASA*, 2007], which is defined as the height at which the mean atmospheric pressure is equal to 6.1 mbar [*Zeitler, et al.*, 2000].

The Ganges ILD is a free-standing mesa containing horizontal and semi horizontal bedded caprock with steeply dipping flank deposits [*Chapman and Smellie*, 2007]. Three separate benches dominate the ILD topography. The ILD overlies chaotic material on the chasma floor [*Lucchitta, et al.*, 1994] and its top is located approximately 1 km below the canyon rim.

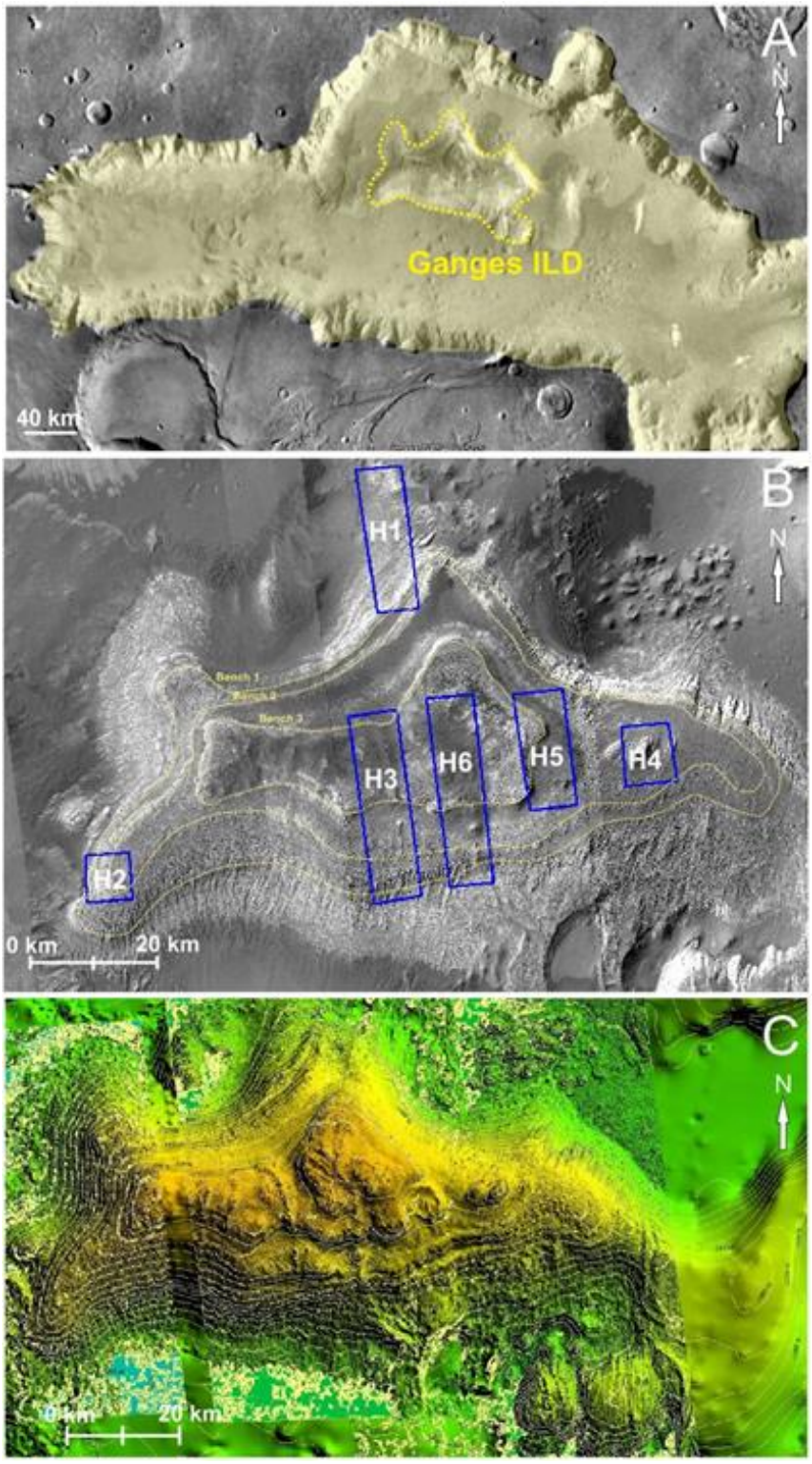

Figure 2.2: A) Ganges Chasma (yellow polygon) with ILD highlighted by the yellow line; B) Locations of the six analyzed HiRISE images (blue boxes, H1-H6) with bench edges marked by dashed yellow lines; C) DTM of Ganges ILD with 200 m contour intervals.

The abrupt termination of flank material around the floor of the Ganges ILD suggests erosion or

confinement against removed materials [*Chapman and Smellie,* 2007]. Light and dark layers of material are exposed on the steep sides of the Ganges ILD [*Lucchitta, et al.,* 1994]. The top of the ILD is relatively flat with a few mounds and knobs [*Lucchitta, et al.,* 1994]. Resistant caprock layers form the top of the Ganges ILD with scalloped edges [*Chapman and Smellie,* 2007]. The absence of large boulders within the ILD suggests that the erosion of wall rock was completed prior to ILD deposition [*Fueten, et al.,* 2011]. Large boulders would be expected in the ILD composition if it was at least partially composed of local wall rock slumps [*Fueten, et al.,* 2011].

Large scale erosional sedimentary structures cutting into otherwise horizontal internal layering have been identified on the ILD surface (Figure 2.3). These will be described in more detail in chapter 3.

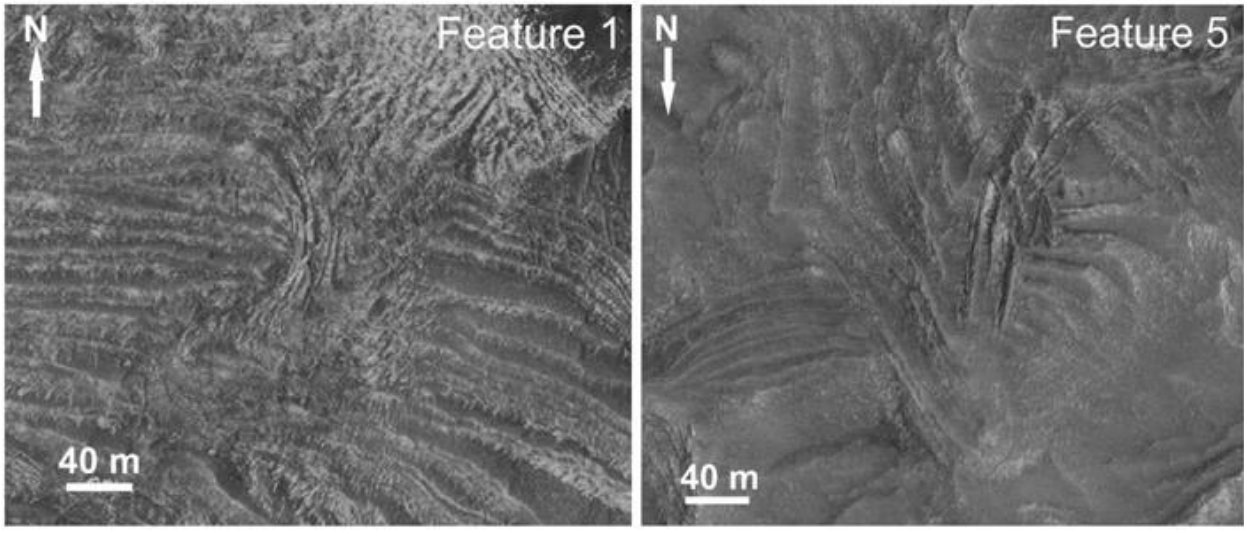

Figure 2.3: Two examples of the large-scale sedimentary features identified in the Ganges ILD HiRISE images. Images are orientated so that the highest elevation is at the top of the image; north is indicated by the arrows. These features are further discussed in Chapter 3.

2.3 Methods

As a base map for the HiRISE images, a CTX mosaic, with a resolution of approximately 6 m/pixel [*Edgett*, 2009], was used. Six HiRISE DTMs (Table 2.1) covering the Ganges ILD at 50 cm/pixel were created from stereo pairs using the NASA Ames Stereo Pipeline [*Broxton and Edwards*, 2008; *Moratto, et al*., 2010]. Individual HiRISE DTM values were adjusted to HRSC topography (Table 2.1) to provide consistent elevation values.

	Image 1	Image 2	Adjustment Used on HiRISE Images
H1	PSP_006519_1730	PSP_007020_1730	+ 727 m
H2	ESP_013059_1725	ESP_012993_1725	+ 831 m
H3	PSP_002550_1725	PSP_003618_1725	+ 728 m
H4	ESP_011648_1730	ESP_011582_1730	+ 828 m
H5	ESP_018162_1730	ESP_018663_1730	+ 778 m
H6	PSP_007877_1725	PSP_007521_1725	+ 876 m

Table 2.1: Six HiRISE stereo pairs used for the Ganges Chasma ILD study and the amount individual HiRISE DTMs were moved to conform to HRSC DTM values

2.3.1 ILD Layer Attitude Measurements

To measure layer orientation, Orion software [*Pangaea Scientific,* 2006-2011] was used. Using 3D coordinates of manually selected points; Orion calculates a best-fit plane using multi-linear regression [*Fueten, et al.,* 2006]. The manually selected points are placed along the trace of the chosen layer (Figure 2.4 A and B), and strike and dip are then calculated based on the point positions (Figure 2.4 C).

Multiple measurements of ILD layering attitudes were conducted in each HiRISE image, repeated in areas of low dust cover to create reliable results [*Fueten, et al.,* 2006]. Ten or more points were used for each layer orientation calculation and the maximum deviation from the layer transect was typically less than 1.0 m over a trace length of 41 m or more. To obtain

accurate results, the points placed along the measured layer were systematically moved along the initial transect until the calculated plane matched the trace of the layer. When the points were adjusted, the uncertainty in the dip value was kept as low as possible, typically ±1 or ±2, and with few exceptions, was kept below the value of the dip. The uncertainty was kept to less than the value of the dip to ensure that the correct dip direction was identified.

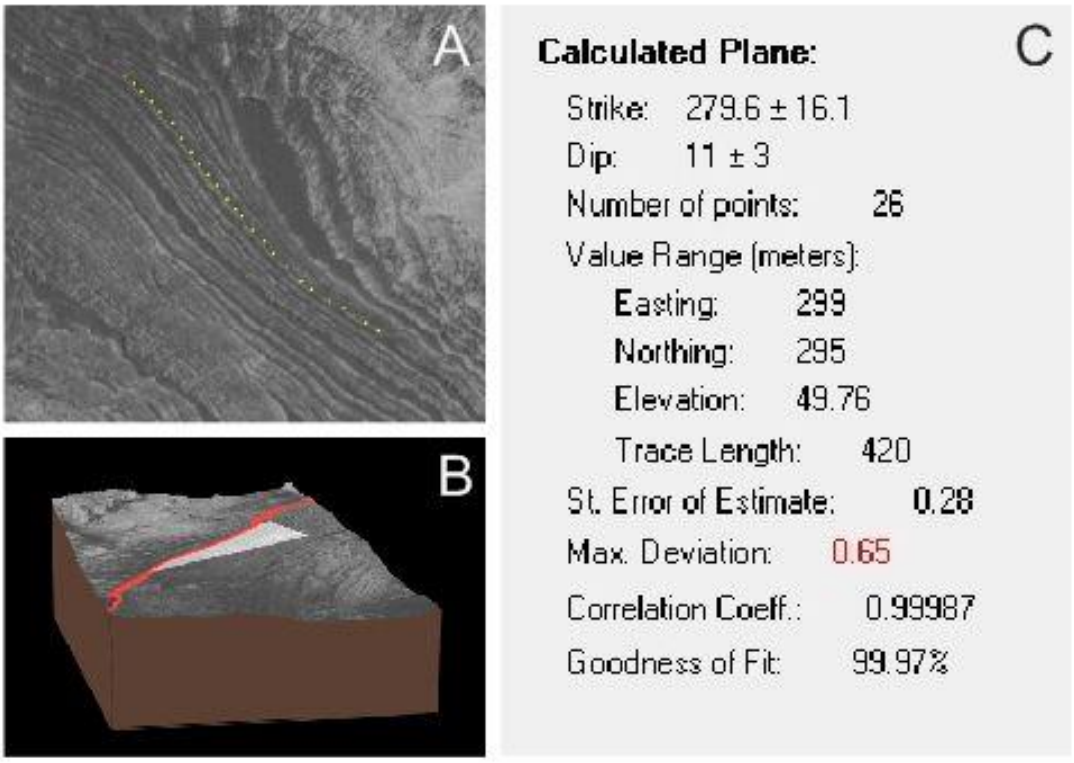

Figure 2.4: A) Placement of points along layer to be analyzed; B) 3D view of calculated strike and dip plane based on point placements in A; C) Orion statistical output of strike and dip of the plane.

Various sets of layers, composed of groupings of contiguous parallel layers, were identified (Figure 2.5). The measurements conducted in layer sets generally depicted small variations in attitude between each layered exposure.

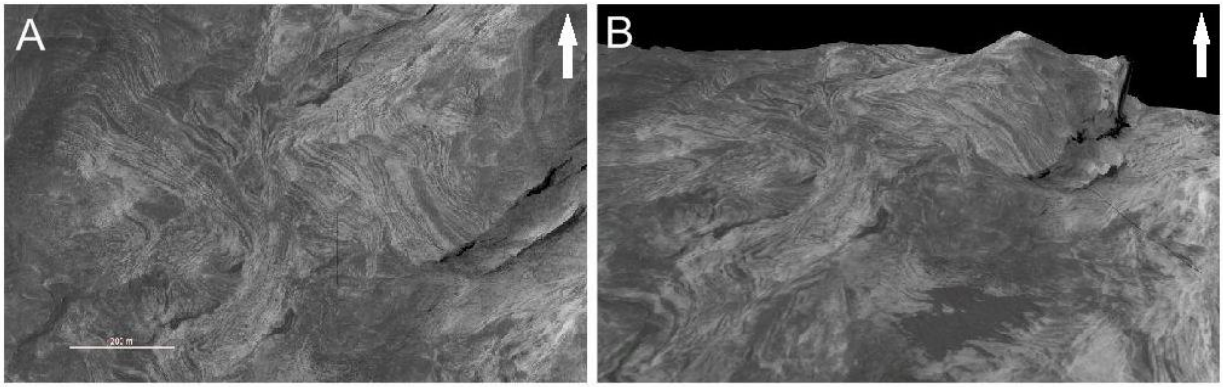

Figure 2.5: Set of layers located in H1; in both images the arrow indicates north and upslope is northeast. A) Plan view looking down at the layer set; B) 3D view of the layer set.

The three benches that dominate the ILD topography represent large scale structures and could not be measured with the same method used for the normal ILD layering and layer sets. Due to the non-planar nature of benches 1 and 2, as well as large anomalous topographic features transecting the ILD, continuous measurements could not be taken along these benches. Multiple measurements had to be taken on the same bench layer in order to obtain accurate orientations (Figure 2.6). The benches were divided into small portions for which accurate localized attitude measurements could be obtained.

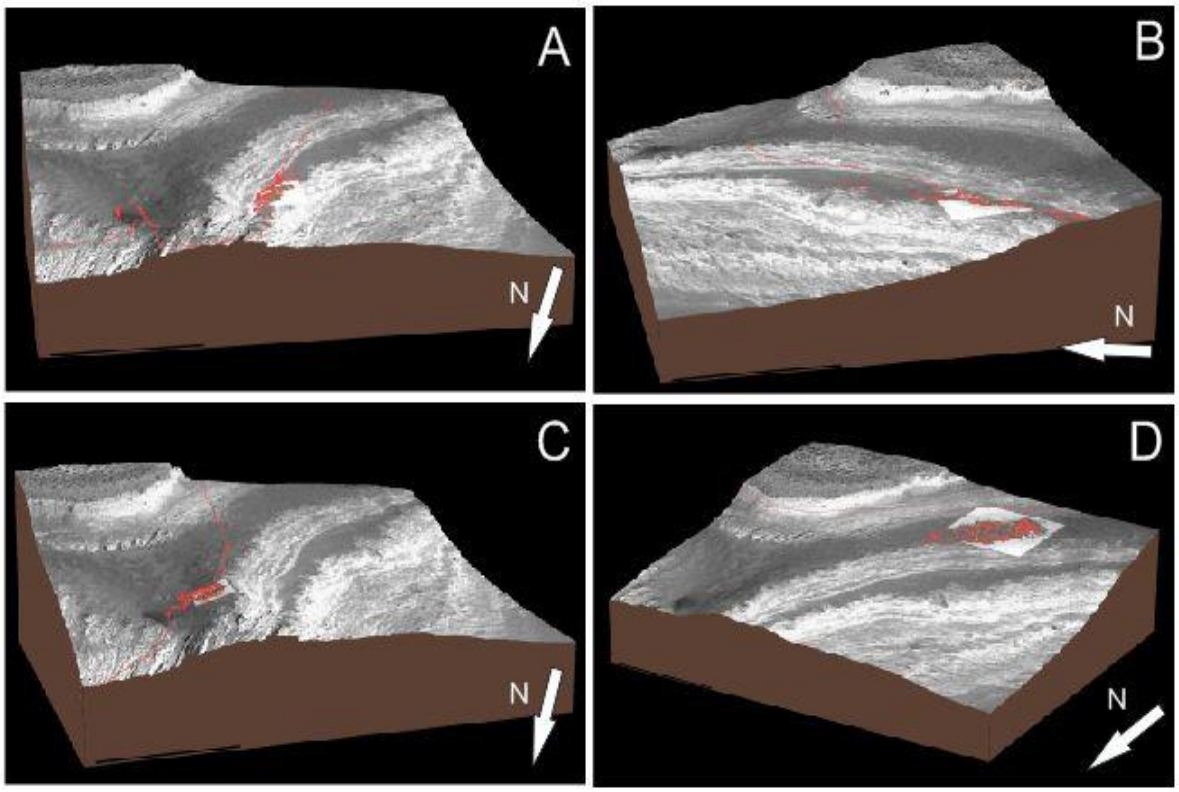

Figure 2.6: A and B) Two 3D images showing two separate strike and dip plane calculations of Bench 1; C and D) Two separate strike and dip plane calculations of Bench 2. The northern corner of each image (bottom left of A, C and D; top left of B) show a large depression above bench 2 which caused the disruption of bench orientation measurements in the northern area of the ILD.

2.3.2 ILD Layer Thicknesses

The Global Mapper [*Blue Marble Geographics*, 1993-2014] program was used to measure layer thicknesses within HiRISE images and derived DTMs. Using this program, point features were placed at each layer boundary of a layer set in a line perpendicular to the local topographic slope (Figure 2.7). The data was then exported to an Excel [*Microsoft Corporation*, 2010] data file where thicknesses were calculated based on elevation differences between point features. Multiple transects for each HiRISE image were measured to obtain multiple thickness measurements for the same elevation range.

The HiRISE DTM provides elevation to the nearest millimeter, while the relative accuracy of the DTM is estimated to be in the range of ~20 cm (*A. Rossi*, Pers. Comm., 2013).

The calculated layer thicknesses in Excel yield layer thickness values on the order of 1 mm, but it can be assumed that these values simply represent layers 50 cm or less in thickness.

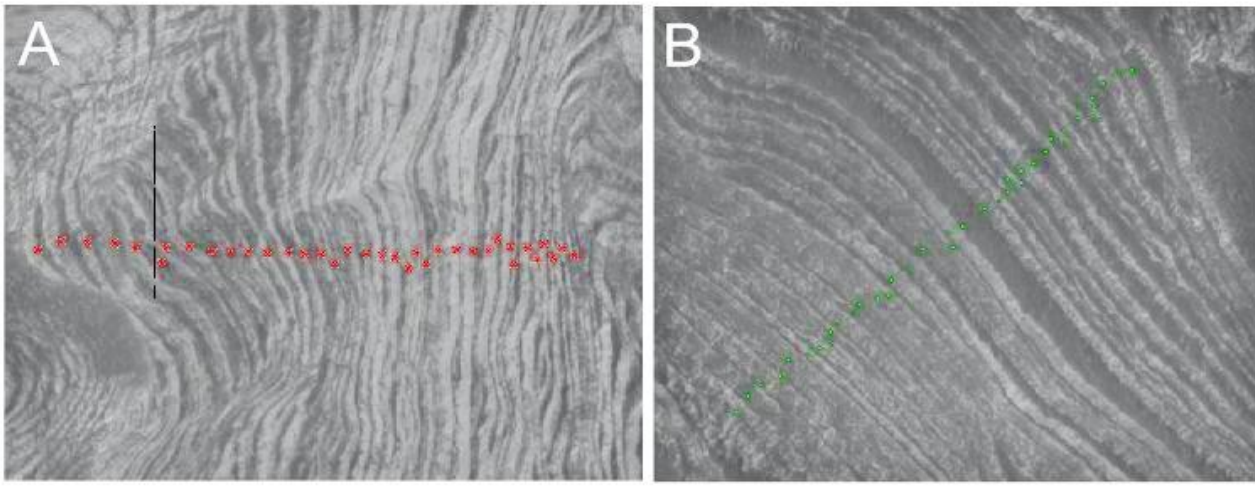

Figure 2.7: Two examples of the layer thickness measurement process. Points are placed on each layer in a linear manner to measure the layer thicknesses over a specified distance.

2.3.3 Presentation of Data

SpheriStat [*Pangaea Scientific*, 2014] orientation analysis software, Microsoft Excel, Corel Draw, and Java Mission-Planning and Analysis for Remote Sensing (JMars) [*Murchie, et al.*, 2007] programs were all used to produce tables and figures. The SpheriStat software provided a method of graphing the strike and dip values obtained from the Orion measurements in Schmidt Net format (Figure 2.15). The number of data points, N, used for each image is recorded in the bottom right hand corner of each histogram. These graphs allowed for easier comparisons of dip direction and magnitude between the different HiRISE images.

Scatterplots and histograms were created using Microsoft Excel software. These graphs allowed for visual analysis of layer orientations, layer thicknesses, and layer frequencies while Corel Draw provided a means to visually enhance the images, graphs, and charts.

2.4 Results

2.4.1 Large Features: ILD Benches and Anomalous Topographic Features

2.4.1.1 ILD Benches

The Ganges ILD is dominated by three semi-horizontal bench features at three separate elevations (Figure 2.8). Five of HiRISE images cover at least two of the three benches.

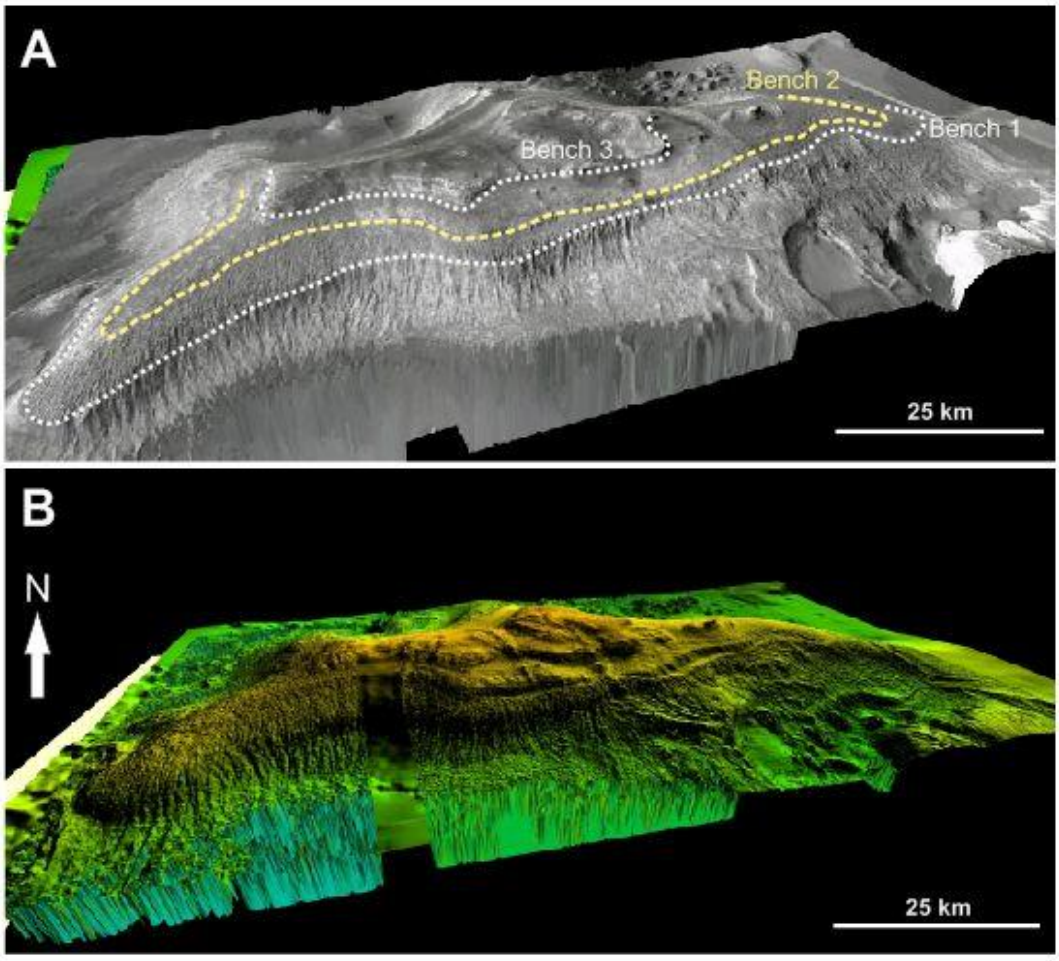

Figure 2.8: 3D depiction of the Ganges ILD. A) DTM composite overlain with CTX mosaic. The approximate edges of all three benches are marked with dashed lines and labelled accordingly; B) DTM colour composite for visual comparison with CTX overlay in A.

These benches separate the ILD into four distinct levels and appear to be controlled by sedimentological processes. All three benches are distinguished by plateaus and edges. Three

edges are present, found at the boundaries of the benches, and are characterized by a steep slope or cliff face (Figure 2.9). On average, the bench edges have slopes of approximately 26°, with the steepest slope observed at 38°. The plateaus of each bench are defined as the areas found above the bench edge to the bottom of the next bench edge (Bench 3 plateau, Bench 2 plateau, Bench 1 plateau, and below Bench 1 plateau) (Figure 2.9).

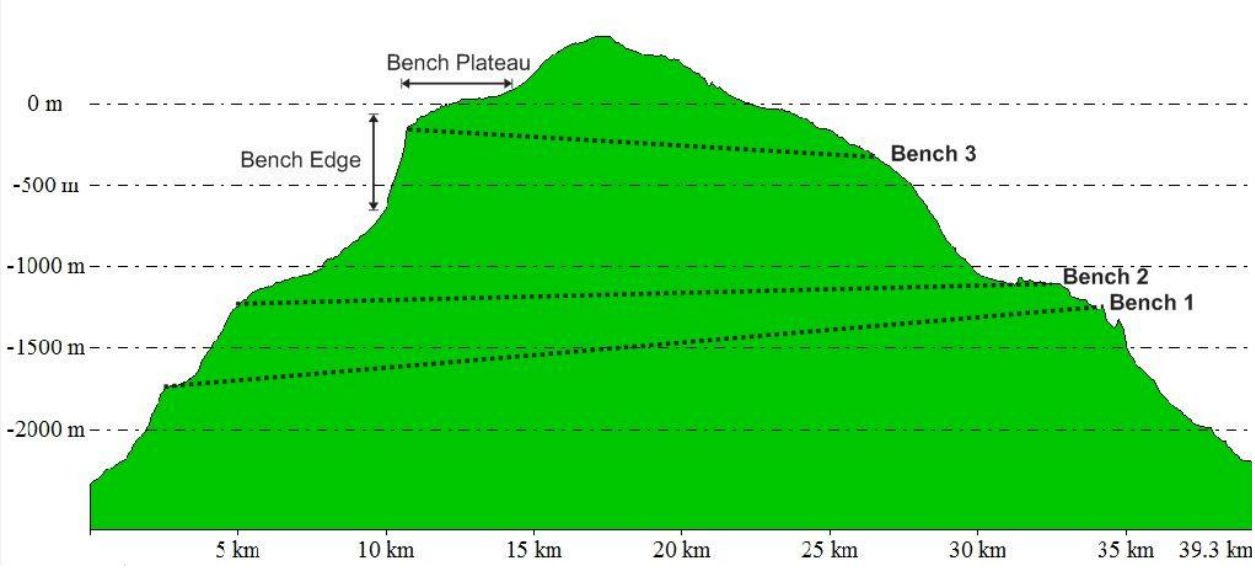

Figure 2.9: Central cross section (North to South) of the ILD mound depicting the three benches and defining the bench edges and plateaus.

Although the bench edge elevations vary, the elevation range for individual benches decreases with increased elevation; an 1100 m elevation range for bench 1 at the bottom of the ILD and only a 550 m elevation range for bench 3 at the top of the ILD (Table 2.2).

Benches	Lowest Elevation Observed	Highest Elevation Observed	Elevation Range
3	-650 m	-100 m	550 m
2	-1600 m	-700 m	900 m
1	-2400 m	-1300 m	1100 m

Table 2.2: Bench elevation values

Due to the non-planar morphology of benches 1 and 2, multiple localized strike and dip measurements were taken of each bench at the bench edges (Figure 2.10). Nine measurements were taken for the edge of bench 3, 13 were taken for bench 2, and 13 were taken for bench 1 (Figure 2.10). Bench 3 is sufficiently planar to be measured using a single strike and dip measurement (Figure 2.11 A), but multiple local bench attitudes were measured for bench 3 to be consistent (Figure 2.10).

Bench 3, located at the top of the mound, is nearly horizontal (Figure 2.11 B), while bench 1 located near the bottom of the mound is the most inclined. As depicted by Figure 2.10, the bench dips generally north along the northern portion of the ILD. The large elevation ranges can primarily be attributed to the steepening of the bench surfaces at the northern tip of the ILD just east of the H1 HiRISE image. Along the southern margin of the ILD, benches generally dip down due to the areas of localized anomalous topographic features which transect the benches (Figure 2.6; Figure 2.12). These features are discussed further in the next section.

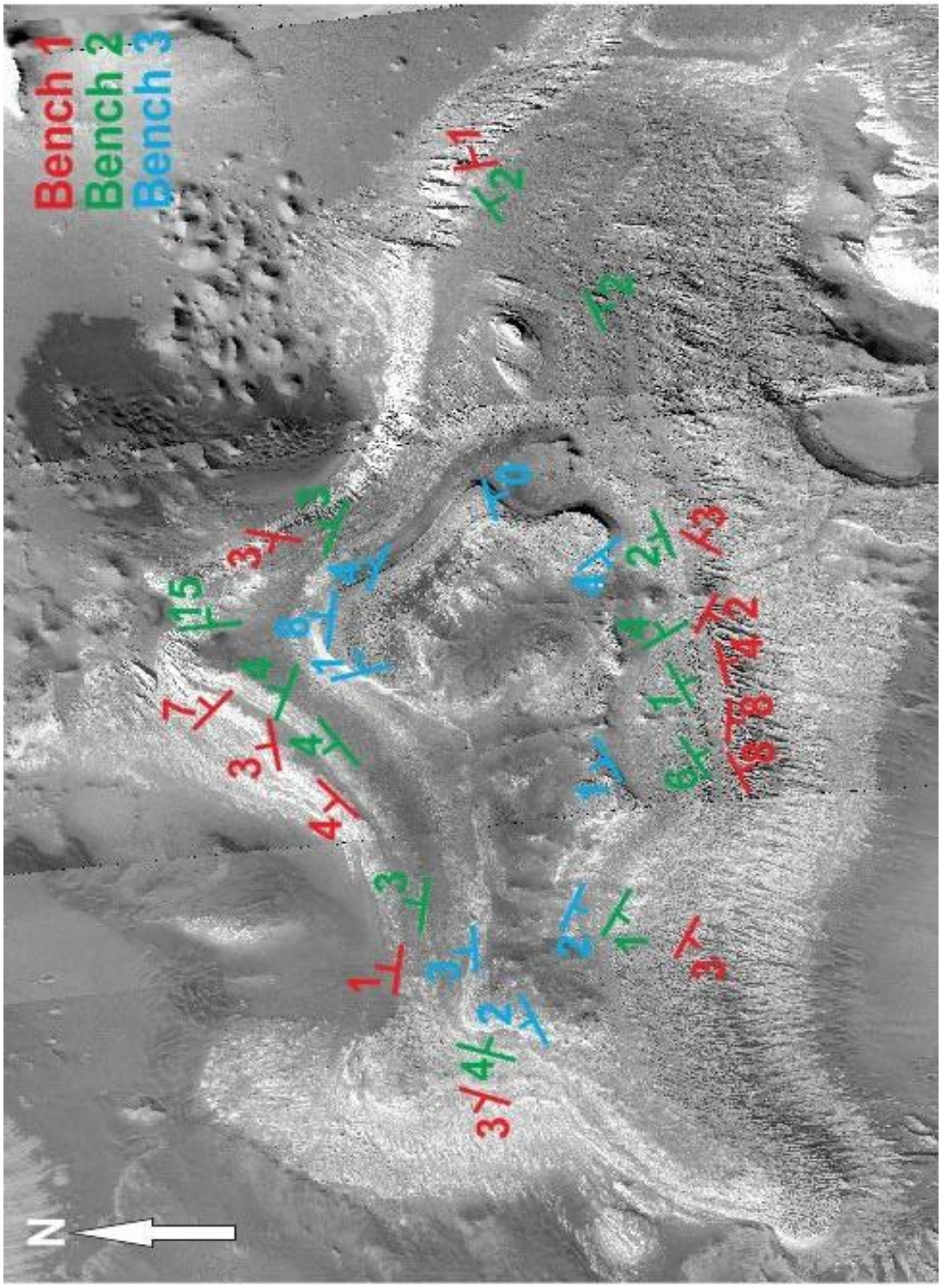

Figure 2.10: Strike and dip orientation measurements of the ILD benches. Cyan represents bench 3 measurements, green represents bench 2 measurements, and red represents bench 1 measurements .

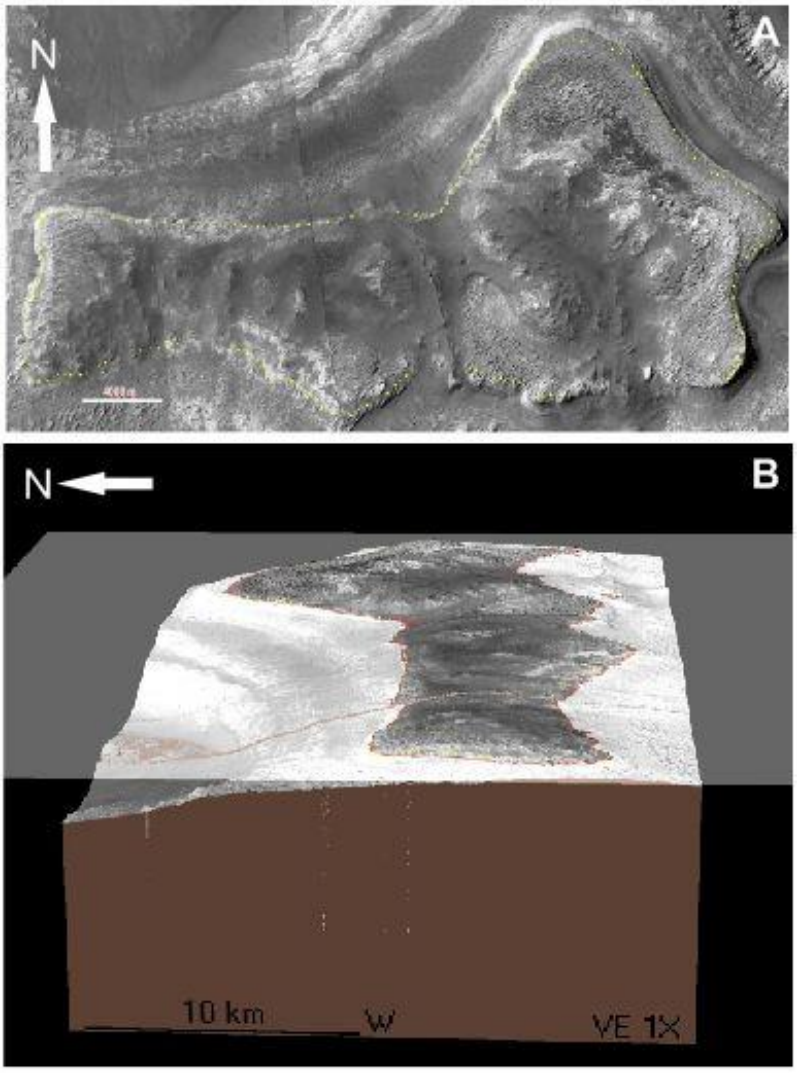

Figure 2.11: Horizontal nature of bench 3. A) Yellow points placed along bench to measure layer attitude; B) 3D depiction of the layer plane.

2.4.1.2 Anomalous Topographic Features

Transecting north-south across the short axis of the mound, are two localized topographic features, identified primarily through the use of a CTX DTM (Figure 2.12 B). These features extend from the apex of the ILD on the plateau above bench 3 and continue down the southern portion of the mound interrupting the layering of all three benches (Figure 2.13). Both features can be traced in a north-south direction and each feature separates into shorter segments

northwards of the edge of bench 3 (Figure 2.12, Figure 2.13). The western feature extends approximately 16 km north-south across the ILD. 10.5 km from the northern tip of the feature, a gap of approximately 1.6 km appears at the edge of bench 3 before the feature reappears to the south as a smaller ridge (W2). The eastern feature extends approximately 19 km along a north-south transect. 12 km from the north tip of the feature at the edge of bench 3, after a gap of 1.3 km, the feature separates into two short segments (E2 and E3) that appear as elongate north-south mounds. The widths of the features from the lowest elevation on the west side to the lowest elevation on the east side ranges from ~1 km to ~4 km.

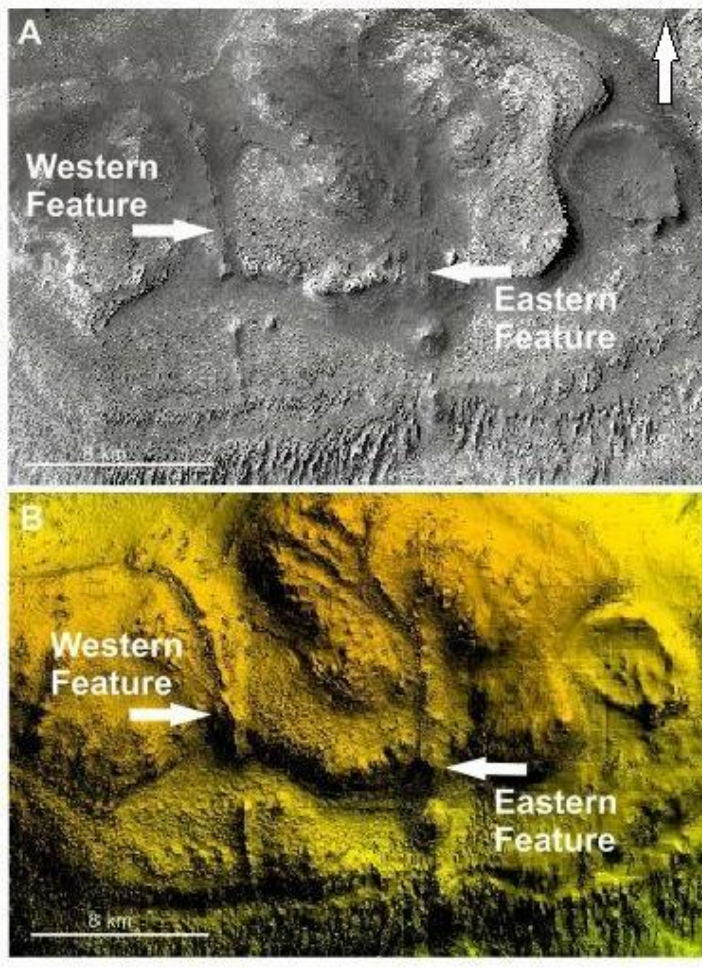

Figure 2.12: CTX (A) and DTM (B) plan view images of the two transecting deformation features on the Ganges ILD. Arrow indicates north.

Cross sections were used to determine the height of the two features. The eastern feature above bench 3 (E1) showed positive relief of ~20 m up to ~115 m above the surrounding topography. The first of the separate mounds located along the eastern feature below bench 3 (E2) had a positive relief of ~300 m above the surrounding topography at the peak of the feature and a very rounded overall shape. The second separation (E3) had a positive relief of ~250 to ~300 m. The western feature above bench 3 (W1) showed a positive relief of ~75 m to ~190 m above the surrounding topography while the separate feature below bench 3 (W2) showed a smaller positive relief of 60-70 m.

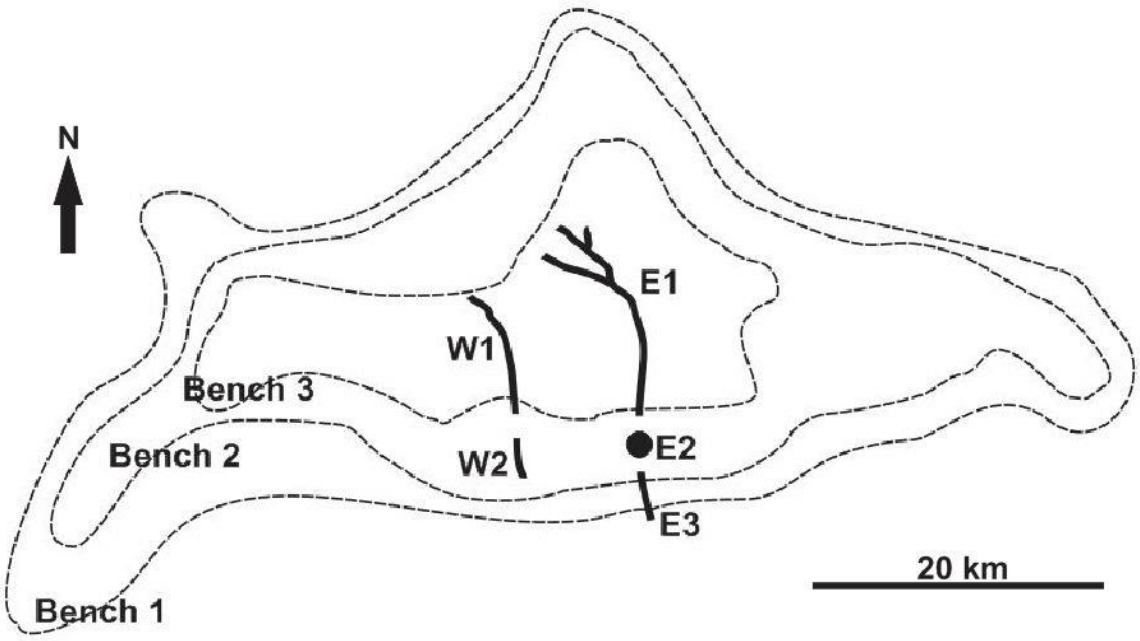

Figure 2.13: A sketch of the relationship seen between the three benches and two anomalous topographic features. Feature segments are labelled for easy identification; benches are represented by the dashed lines and identified accordingly. The ILD shows deformation at the north and south extents of the deformation features.

On both sides of each feature, the benches dip inwards towards the features causing areas of deformation. At these points, the eastern feature forms steep slopes above surrounding topography of approximately 6° to 21°, while the western feature has more gradual slope

changes above surrounding topography of 5º to 8º. The western feature is restricted in width (1 km to less than 2 km) making it thinner than the eastern feature which is 2 km or more in width in most areas.

Overall the eastern feature showed a positive relief range of almost 300 m with steeper slopes than the western feature which had a smaller relief range of 130 m and gradual slope changes. The eastern feature also has more rounded and flat topped profiles than the sharper peaks of the western feature.

2.4.2 Layer Attitudes

Throughout the six HiRISE images, a total of 504 strike and dip measurements were taken of ILD layers and bench positions (Table 2.3). Layer attitudes measured within the HiRISE DTMs indicate an overall shallow dip for the ILD layering, with an average dip angle of 10.5º and an average strike of 201º. Table 2.4 depicts the dips in each HiRISE image.

Stereo Pair Images	Number of Orientation Measurements
H1	234
H2	53
H3	67
H4	83
H5	25
H6	33

Table 2.3: Number of orientation measurements conducted in each stereo pair image

This data indicates that the layering observed in the two images located on the edges of the ILD, lower in elevation, (H1 and H2; Figure 2.14) have slightly steeper average dips than the other four locations. Figure 2.14 depicts all layer dips measured against the ILD elevations. H1 and H2 at the lowest elevations (Figure 2.14, Figure 2.15) have larger maximum dip values then images H3 to H6, located at the highest elevations (Table 2.4). This suggests that while most dips are

shallow, the maximum dip decreases with increased elevation. The average dip direction of layering in each HiRISE image parallels the ILDs topographic slope.

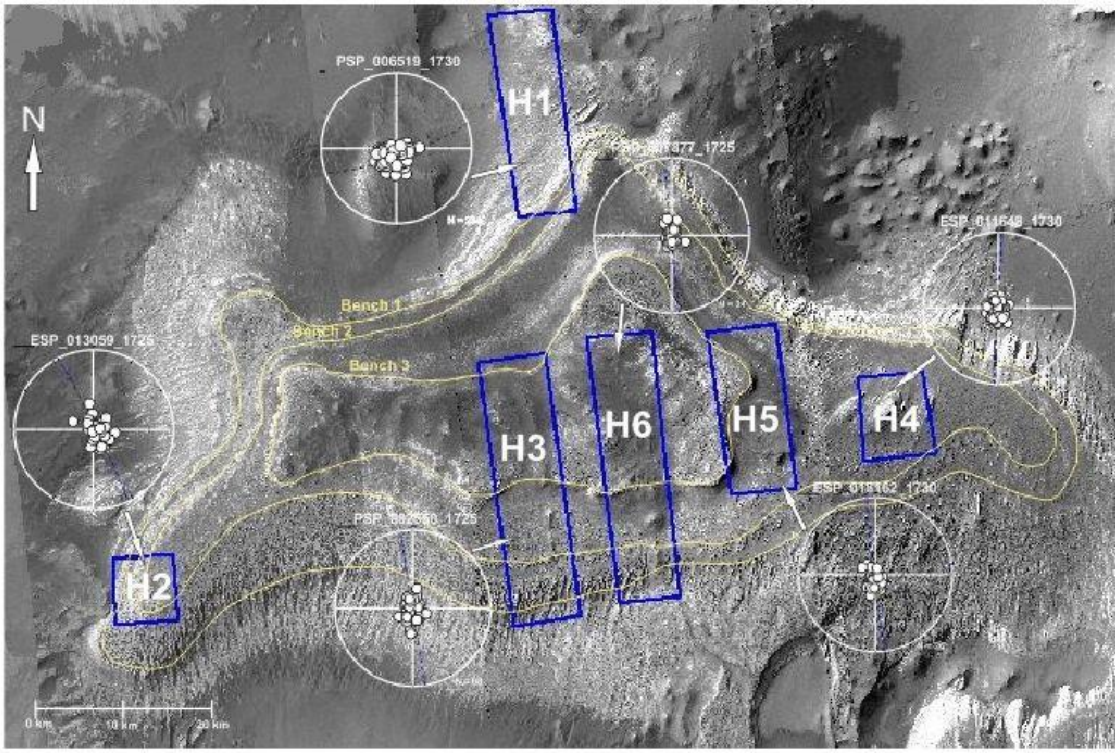

Figure 2.14: HiRISE image locations with labels (H1-H6). Stereonet insets depict strike and dip directions.

Image H4, on top of the plateau of bench 2, shows two distinct dip directions: a northern dip in the northern portion of the image, and a southern dip in the southern portion of the image. The bimodal nature of image H4 resulted in two average strike calculations, one for the northern half and one for the southern half of the image. The layering in the majority of the HiRISE images (five of six; H2-H6) show a north-south strike direction; only H1, the northern most image found at the lowest elevations, shows a significant east-west spread of layer strike (Figure 2.14; Figure 2.16). Generally, the layer attitudes appear to follow the ILD and bench topography. In most instances, layers appear to dip in the same direction of the slope or nearly downslope of the ILD and parallel the bench topography.

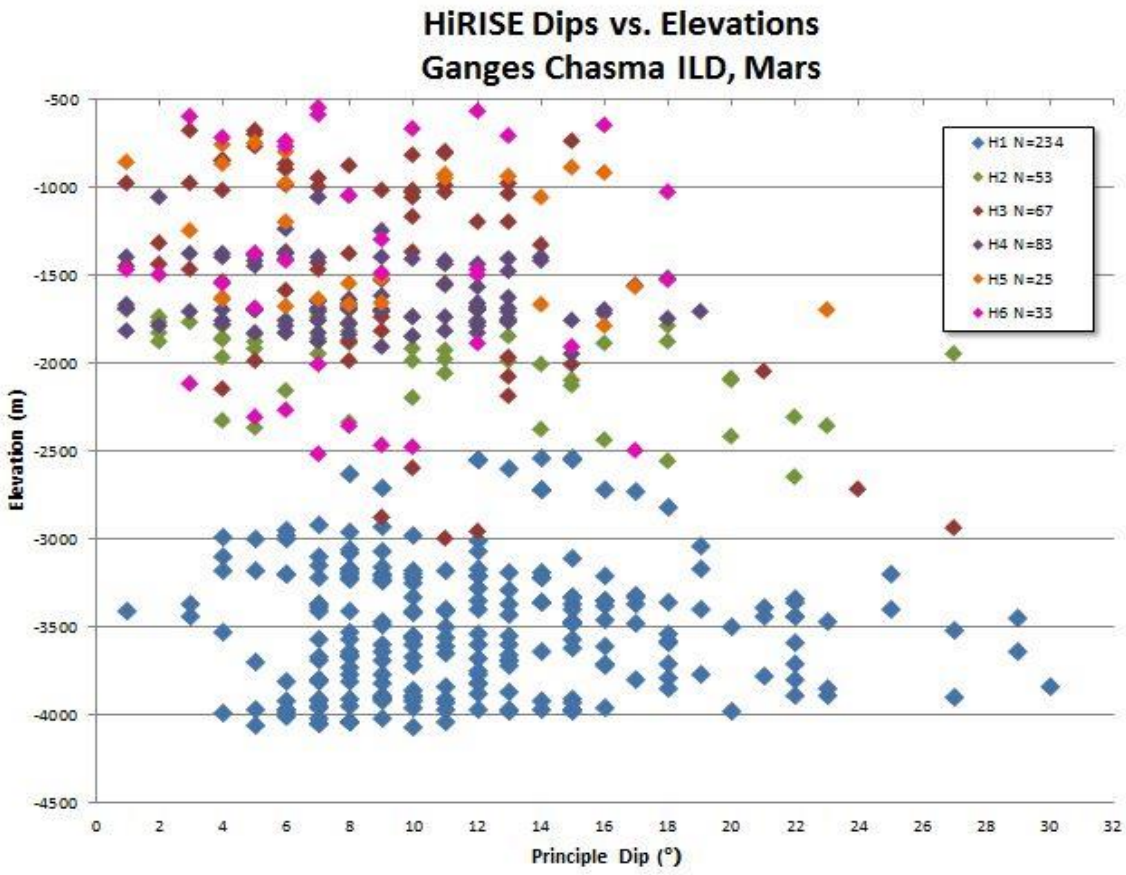

Figure 2.15: Dip vs. Elevation of the various layers measured in the Ganges ILD.

Stereo Pair Images	Average Dip	Dip Range (Max/Min)	Average Strike	Strike Range (Max/Min)	Primary Dip Direction
H1	12º	30º/1º	260º	359º/29º	Northwest
H2	10º	27º/1º	180º	277º/5º	West-Northwest
H3	8.9º	27º/1º	167º	359º/2º	South-Southwest
H4	8.7º	19º/1º	N: 252º S: 165º	337º/2º	North/South
H5	9º	23º/1º	209º	334º/28º	East-Southeast
H6	8.5º	18º/1º	169º	344º/44º	South-Southwest

Table 2.4: Average strike, average dip, strike and dip ranges, and primary dip direction for the analyzed Ganges HiRISE images.

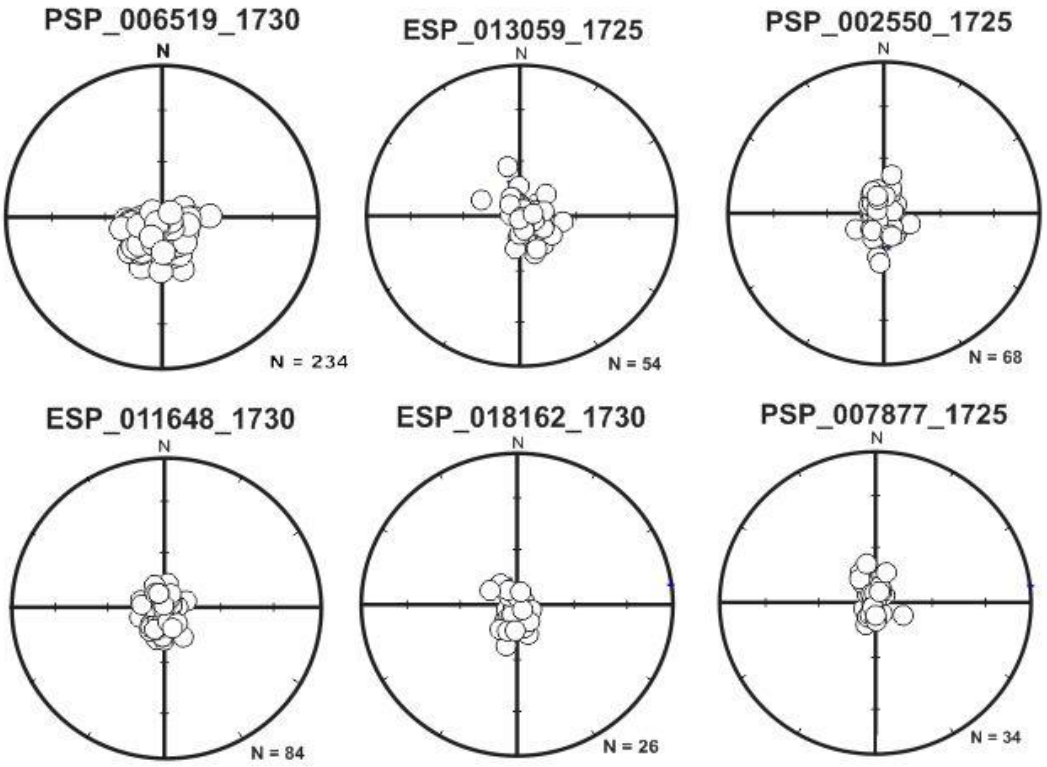

Figure 2.16: Stereonet compilation of the six HiRISE images.

Each of the six HiRISE images had multiple layer sets, each composed of exposures of multiple contiguous parallel layers. In image H1, one major layer set (Figure 2.17) located below bench 1 has multiple distinct erosional surfaces or layer truncations, and it was possible to measure the different layer attitudes (Figure 2.18 B). Seven strike and dip measurements were taken in this layer set ranging from 7º to 25º in dip, all dipping northeast (Figure 2.18 A). A cross section along the measured transect (Figure 2.18 C) illustrates the complexity of the layer attitudes at this location.

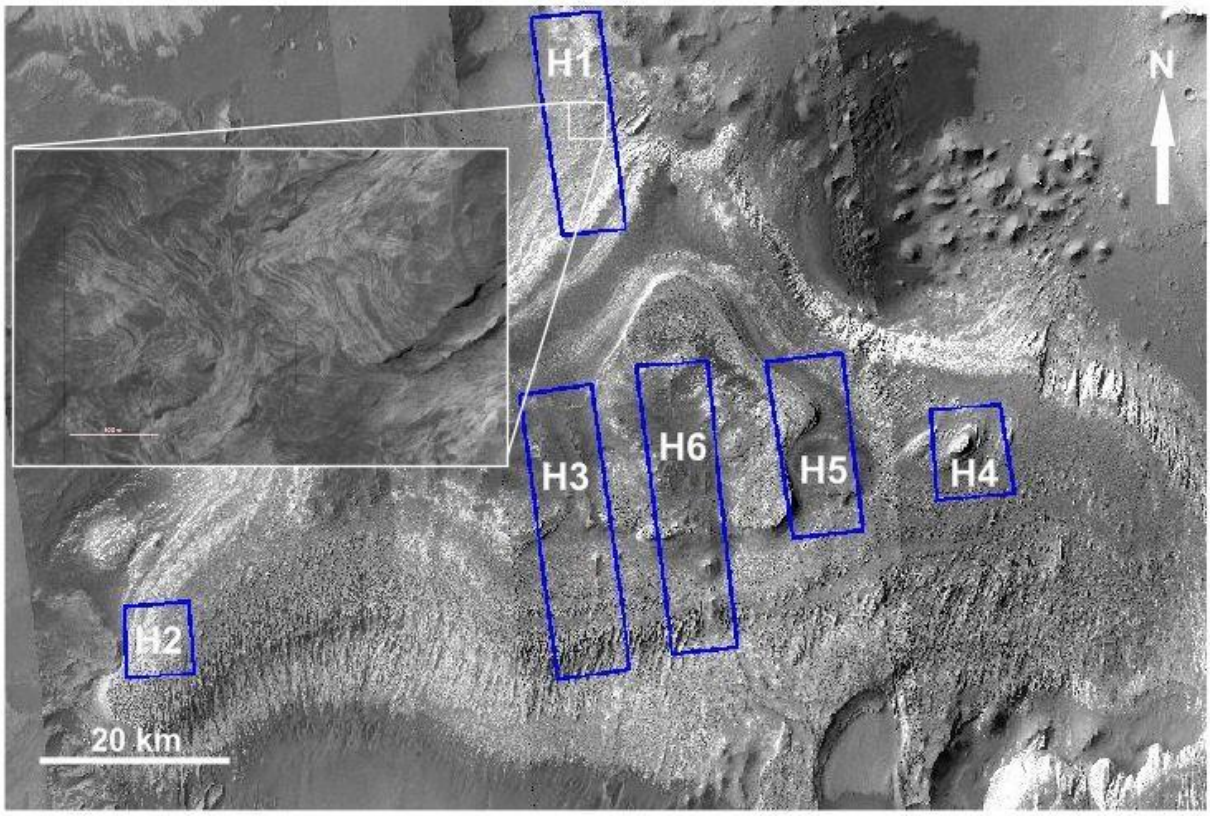

Figure 2.17: Major set of layers (inset outlined by white box) observed in H1. This layer set was used to analyze the complexity of differing layers in one location.

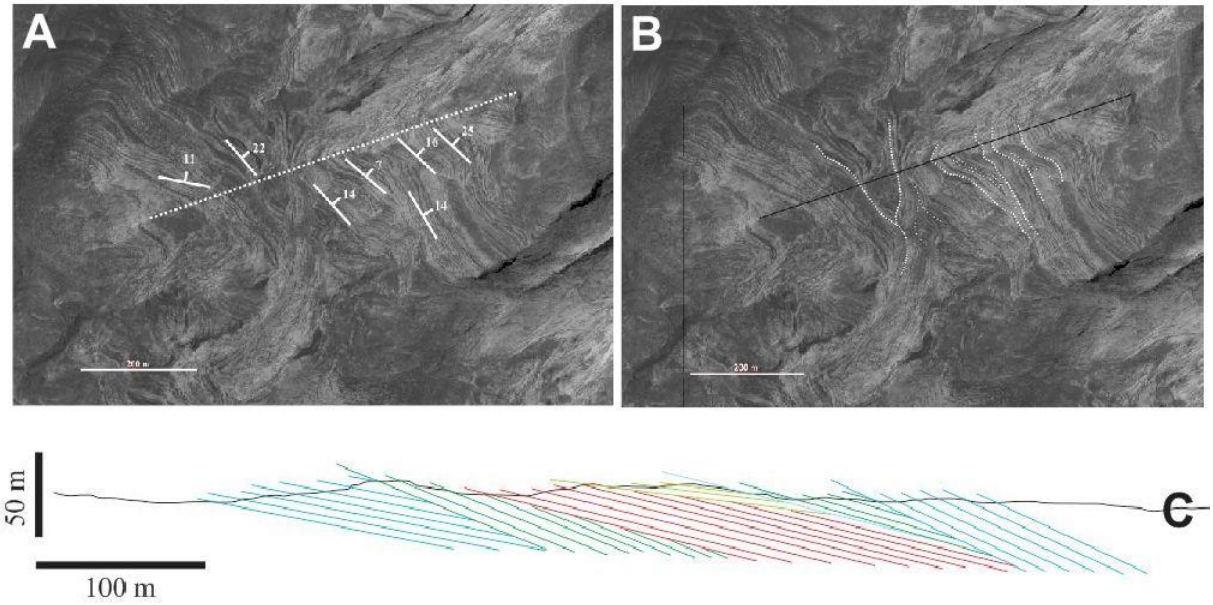

Figure 2.18: A) Strike and dip measurements of the layers within the set of layers; B) Outlined truncation boundaries (white dashed lines) found; C) Interpreted cross section based on the dipping angle of each layered section.

2.4.3 Layer Thicknesses

118 layer thickness transects were measured throughout the six images, with each image containing a different number of transects (Table 2.5), dictated by the availability of distinguishable layers. Normally, twelve or more sample points were chosen for each transect, as described in section 2.3.2, with few exceptions; six transect points was the minimum for one transect.

Image	Number of Layer Thickness Transects Taken
H1	27
H2	18
H3	17
H4	27
H5	14
H6	15

Table 2.5: Number of layer thickness transects conducted in each of the six HiRISE images.

A total of 2082 layer thicknesses were measured. The average layer thicknesses within the individual images varied from 0.7 m to 1.7 m (Table 2.6) with an overall average thickness of 1.04 m. The majority of the layers are thinner than 1.5 m; 99% of the layers are thinner than 12 m (Figure 2.19). Only 11 measurements of the 2082 measurements exceeded 10 m; all occurring in the H6 and H5 images. In all images, the thinnest layers are millimetres in thickness which as discussed above are below the measurement precision (Table 2.6). The thickest layer measured was 16.7 m in H6. The HiRISE images covering the higher elevations of the ILD have a larger amount of dark mesa sediment covering creating difficulties in distinguishing layering. Due to this covering, layers may have been missed resulting in 11 layers with thickness values of > 10 m. While these layers may represent a few isolated significant events, it is more likely that they are the result of measurement error due to missed intermediate layers.

Stereo Pair Images	Mean Layer Thickness (m)	Minimum Layer Thickness (m)	Maximum Layer Thickness (m)	Standard Deviation
H1	0.7	0.001	8.8	0.96
H2	1.2	0.003	6.3	0.99
H3	1.4	0.008	5.4	0.87
H4	0.8	0.002	4.6	0.75
H5	1.7	0.004	13.4	1.80
H6	1.4	0.005	16.7	2.84

Table 2.6: Mean, Minimum, Maximum, and Standard Deviation layer thickness values for the six analyzed stereo pair images. Minimum layer thicknesses are well below the measurement precision and are therefore assumed as skewed.

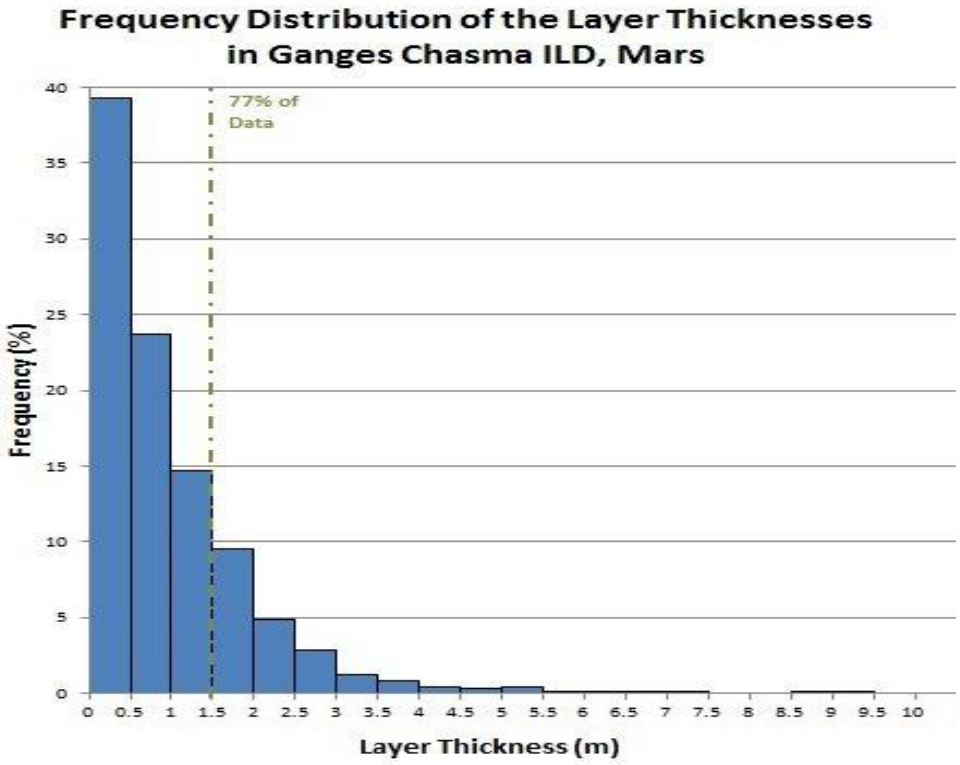

Figure 2.19: Histogram analysis of the layer thickness measurements. 77% of the data shows a layer thickness of 1.5 m or less, with 99% of the data below 12 m in thickness.

To investigate whether layer thicknesses correlate with benches, the layer thickness measurements were categorized based on the bench elevation ranges. 574 of the 2082

measurements are taken of the layers on the slopes between benches while the remaining 1508 measurements were taken of the layers on the bench platforms (Figure 2.20).

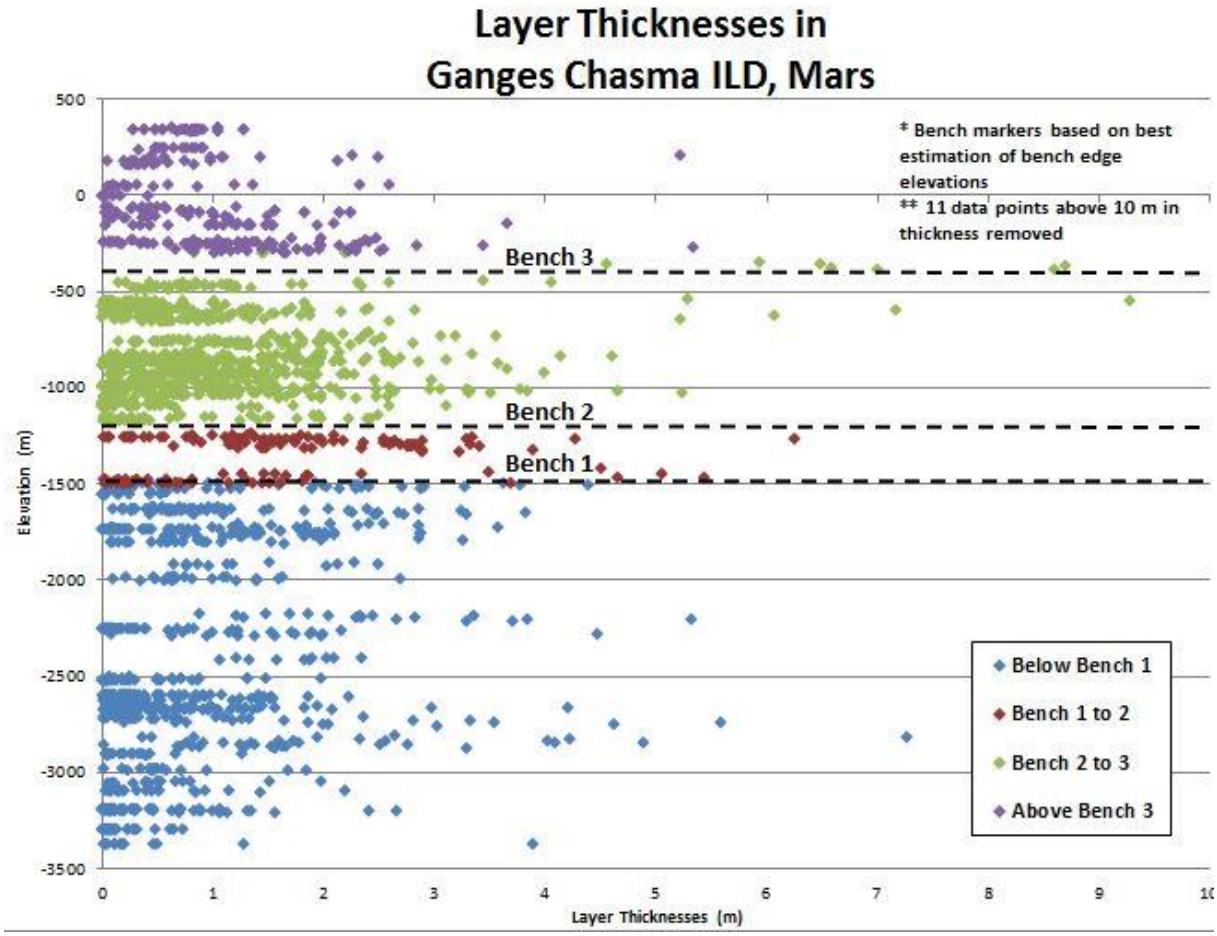

Figure 2.20: Layer thickness measurements taken during analysis of the six HiRISE images used for this study. The 11 data points above 10m were removed due to their outlier nature; these data points were determined to be anomalously thick due to the indistinguishable layering. Eliminating these layers allowed for more differentiation between the thinner layers.

2.4.3.1 Moving Averages of Layer Thickness Data

The large number of layer thickness measurements did not immediately display any apparent trends such as overall thickening or thinning upwards through the ILD. Moving averages (MA) were calculated for the complete ILD layer thickness data and for individual

HiRISE images in order to smooth the data. For all HiRISE images, a 25 m, 50 m, and 100 m moving averages was calculated to check for trends in the thickness data.

In all instances, the 25 m MA proved to be the best method for recognition of trends. The 25 m MA, calculated for the complete set of layer thicknesses, showed two peaks at approximately -300 m and -1350 m (Figure 2.21). These peaks fall within the estimated height ranges of benches 2 and 3. No data peak was seen at the estimated elevation range of bench 1.

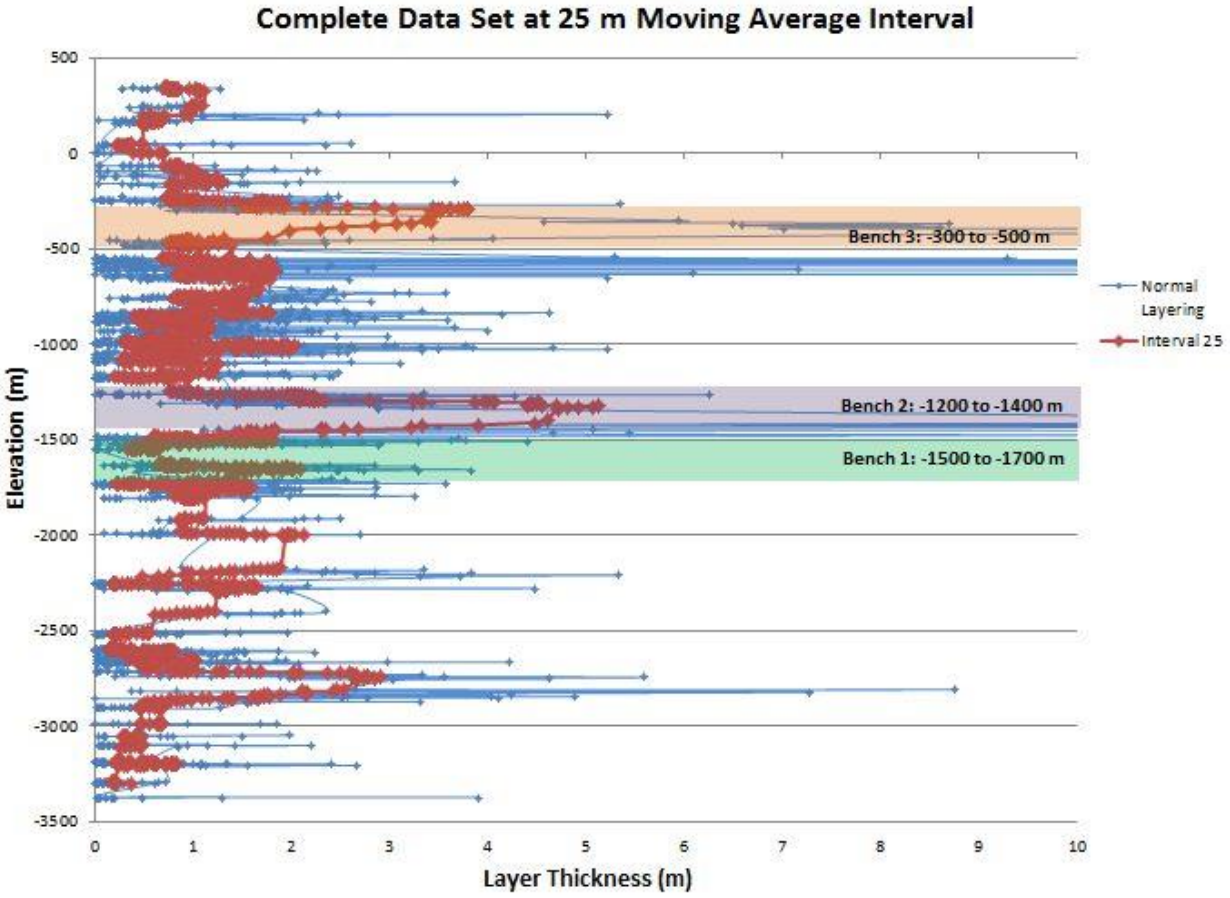

Figure 2.21: Graphed data for the 25 m moving average interval calculated on the complete HiRISE data set. The original layer thickness data is represented by the thin blue line; the moving average calculation is represented by the thick red line. The elevation ranges for all three benches are represented by the coloured rectangles (green: bench 1, purple: bench 2, orange: bench 3).

The data peaks observed in the complete set of layer thicknesses appear to correlate with the different benches, however, the varying elevations of the benches limit the ability to assign

each bench to a specific, consistent elevation. The varying bench elevations make it difficult identifying whether the data peaks are actually correlated with bench locations. To investigate this possibility, the data was further subdivided. The three southern most HiRISE images (H3, H5, and H6) are all located parallel to one another at the southern edge of the ILD and the elevations for all three benches are quite consistent. Data from each of these images contains significant gaps that which does not lend itself to individual analysis. However, due to the consistency of bench elevation and proximity of HiRISE images justifies combining their data (Figure 2.22). Significant data peaks occur at the elevations corresponding with benches 1 and 3 (Figure 2.22). There may be a possible peak at the elevation range for bench 2, however, the lack of data between the elevations of 900 m to 1000 m creates a 100 m data gap that coincides with the elevation range of bench 2 (Figure 2.22). Data from images H3, H5, and H6 were also graphed individually to determine consistency with bench correlations. H3 reflects the same patterns as the three combined images with a small data peak at the elevation ranges for bench 1 and 3 and a large gap through the area of bench 2. Limited data resulted in major data gaps for H5 and H6. No peaks or patterns are present in H5 while H6 shows the beginning and ending of possible peaks for benches 1 and 3, reflecting the overall pattern of the three southern HiRISE images.

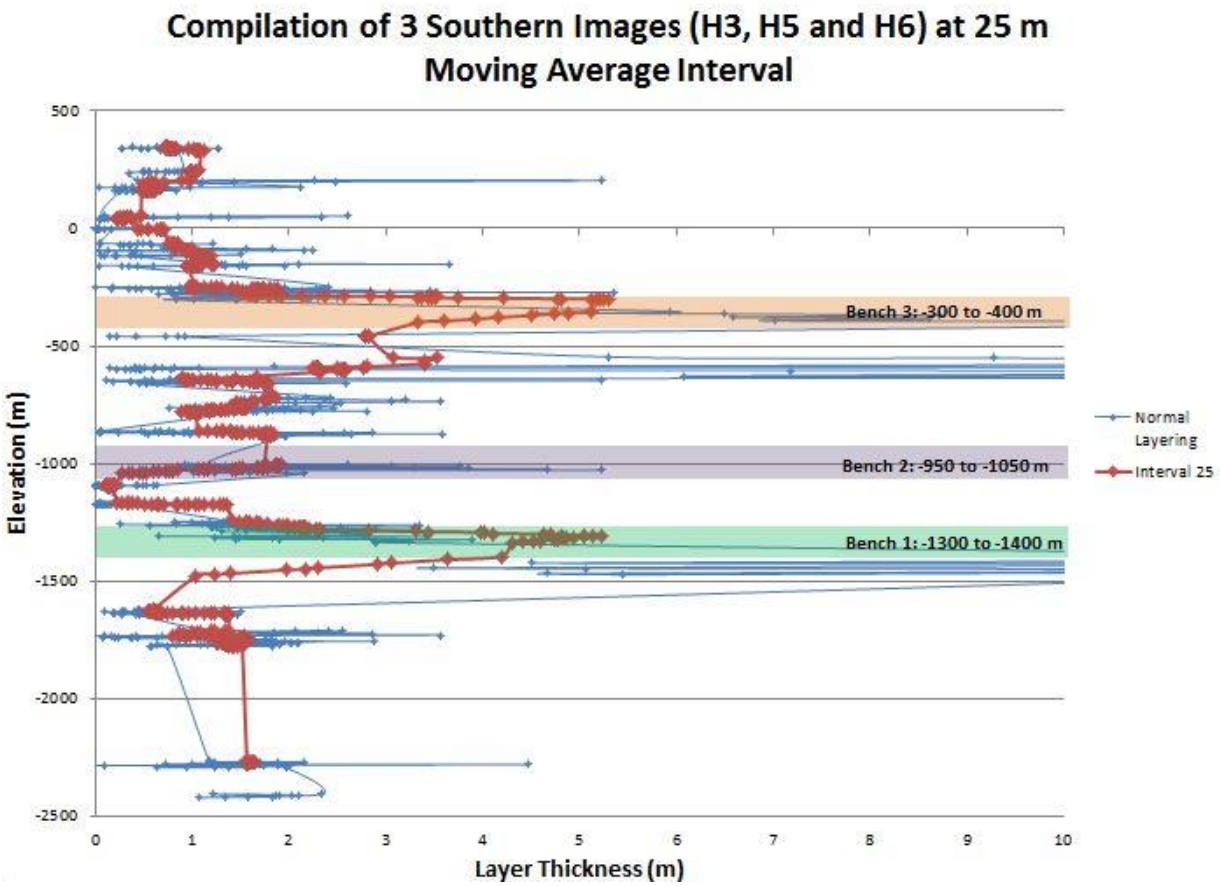

Figure 2.22: Graphed data for the 25 m moving average interval calculated on the three southern images. The original layer thickness data is represented by the thin blue line; the moving average calculation is represented by the thick red line. The elevation ranges for all three benches are represented by the coloured rectangles (green: bench 1, purple: bench 2, orange: bench 3).

Data from the northern image H1 was also plotted individually. This image does not cross bench 3, and barely crosses bench 2, but does show some interesting trends (Figure 2.23). No peak is present for bench 2 due to limited data available, and the formation of a possible peak for bench 1 (Figure 2.23). In addition, at approximately -2750 m an obvious peak is present in the data; this elevation is above the chasma floor and below bench 1. H1 is the only HiRISE image that covers this low elevation; the data peak does not correlate with any obvious large scale topographic feature.

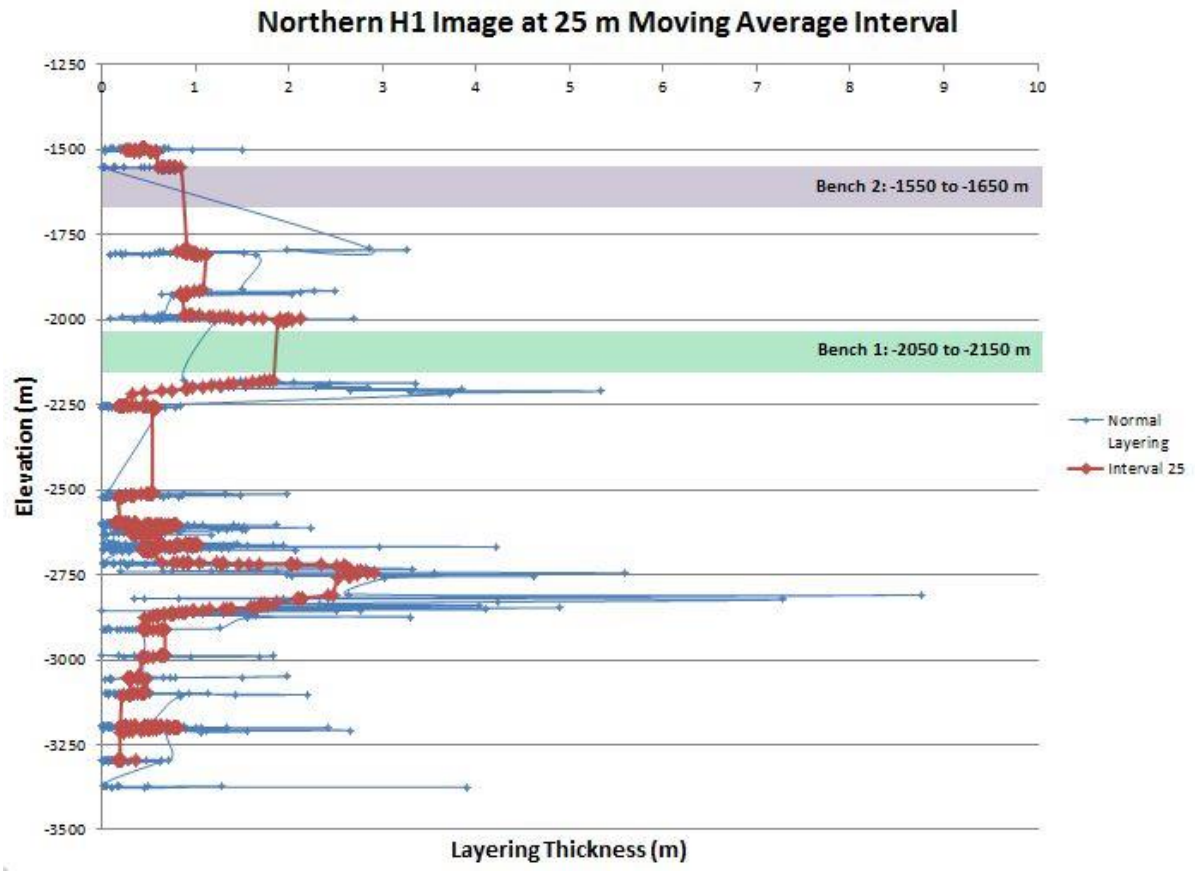

Figure 2.23: Graphed data for the 25 m moving average interval calculated for the H1 HiRISE image. The original layer thickness data is represented by the thin blue line; the moving average calculation is represented by the thick red line. The elevation ranges for the two benches are represented by the coloured rectangles (green: bench 1, purple: bench 2). At -2750 m, a data peak is observed which does not correlate with any of the ILD benches.

2.4.4 Mineralogy

CRISM data was analyzed by J. Flahaut, Murchie *et al.* [2007], and through personal use of JMars software [*Christensen, et al.,* 2009]. The data indicates the presence of monohydrated (MHS) and polyhydrated sulfates (PHS) in the ILD. Although limited CRISM data is available for the Ganges ILD, Figure 2.24 depicts the lower elevations (below bench 2) as dominated by MHS, represented in yellow, while the higher elevations (above bench 2) appear to be dominated by PHS, represented in purple. The contact of the two units shows a mixture of the two sulfates rather than a sharp distinction (Figure 2.24). This mixed-phase contact occurs between the top of

the first and bottom of the second benches. The MHS and PHS dominated areas can be clearly identified in the western CRISM images in Figure 2.23.

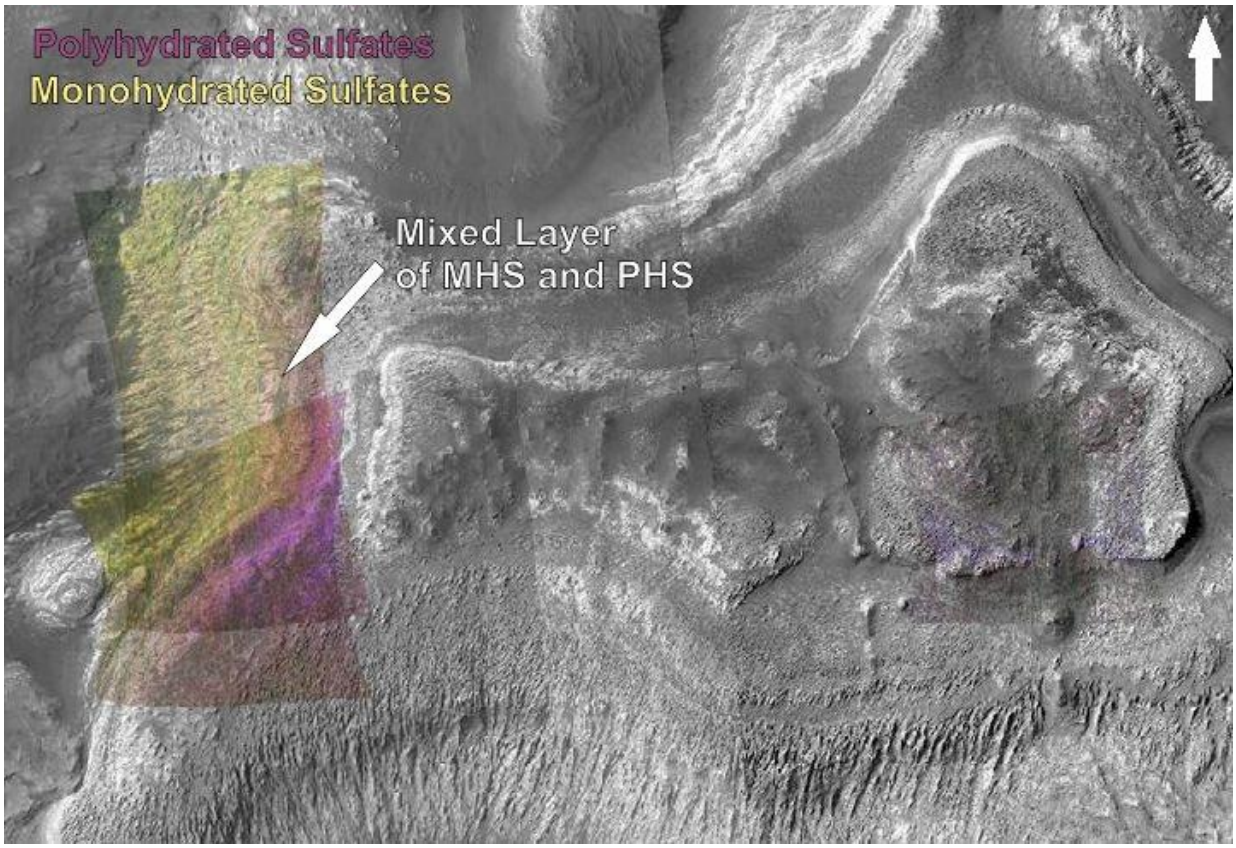

Figure 2.24: Three (2 west images, 1 east image) CRISM data overlays on the Ganges ILD. The yellow colour represents monohydrated sulfates (MHS) while the purple colour represents polyhydrated sulfates (PHS). The pink colour seen between the MHS and PHS represents a mixed phase of the two sulfates. White arrow indicates north.

In the eastern portion of the ILD in Figure 2.24 depicts a slight PHS signature represented in a pale purple colour. The dark capping mesa layer that is largely present on the top of the ILD creates difficulty in identifying sulfates present above the third bench. The eastern identification is minor due to the interference of this dark mesa layer. However, this minor signature still

correlates with the western images in Figure 2.24 where PHS dominate the top portion of the ILD above bench 2.

2.5 Discussion

The data covers approximately 2.5 km of cumulative sequences of strata on the Ganges ILD. Each HiRISE image was used to calculate and analyze bench attitudes, deformation features, layer attitudes, layer thicknesses, and mineralogical composition.

2.5.1 Layer Attitudes

Layering was generally parallel and showed an overall shallow dip of 10.5°. In most instances the ILD layering of the E-W orientated ILD strikes approximately E to W and dips approximately N or S, coinciding with the downslope direction. Prior data analysis supports these findings by indicating that ILD layers generally dip into adjacent chasma and parallel the E-W VM canyon axis [*Fueten et al.*, 2004]. A few sample locations near the eastern and western ends of the Ganges ILD show N-S strikes rather than the typical E-W trends, suggesting a differing sedimentary setting at these stratigraphic layers. In general, layers dipped away from the centre of the mound and become flatter at higher elevations. This flattening of layers suggests that a topographic high was present on the chasma floor before deposition of the ILD sediments.

The cross section constructed from the large layer set in H1 provides a possible scenario of the 3D geometry of the sediment at the lower elevation. The strikes and dips in this layer set all dip in the same direction, yet have varying degrees of dip (7°-25°) (Figure 2.18).

2.5.2 Layer Thicknesses

Layering thicknesses appear consistent throughout the ILD. At all elevations, the majority of the layers remained relatively thin (<2 m). Overall, there is a very slight thinning of the layers upwards through the ILD.

Compared to other VM chasmata, the Ganges Chasma layer thicknesses appear to be consistently low with averages in all HiRISE images below 2 m. In Juventae Chasma, layer thicknesses average 2.6 m, 3.2 m, and 83.5 m for the three mounds [*Novakovic, et al*., 2013], Capri Chasma has layer thickness averages between 2 m and 7.5 m [*Calvert, et al.*, 2013], and Candor Chasma shows layer thickness between 2 m and 11 m overall, with 4 m to 13 m averages in the lower unit and less than 4 m on average in the upper unit [*Fueten et al.,* 2014]. Variations between these ILDs could be attributed to numerous processes and sedimentology characteristics such as sediment composition and size. The thinner layers observed in Ganges Chasma may be attributed to short-lived depositional events where numerous layers of sediment were deposited in quick succession, or to a reduced volume of sediment influx, leading to the thin layers observed. Additional data for the Juventae, Capri, and Candor Chasma ILDs is needed for further comparisons.

It was noted that layering measured on the bench edges, was typically thicker than layering measured on the bench plateaus. In addition, several data sets include anomalous thickness values (>10 m in thickness), primarily along bench outcrops, though these may be due to lack of layer definition along the bench edge topography (Figure 2.25).

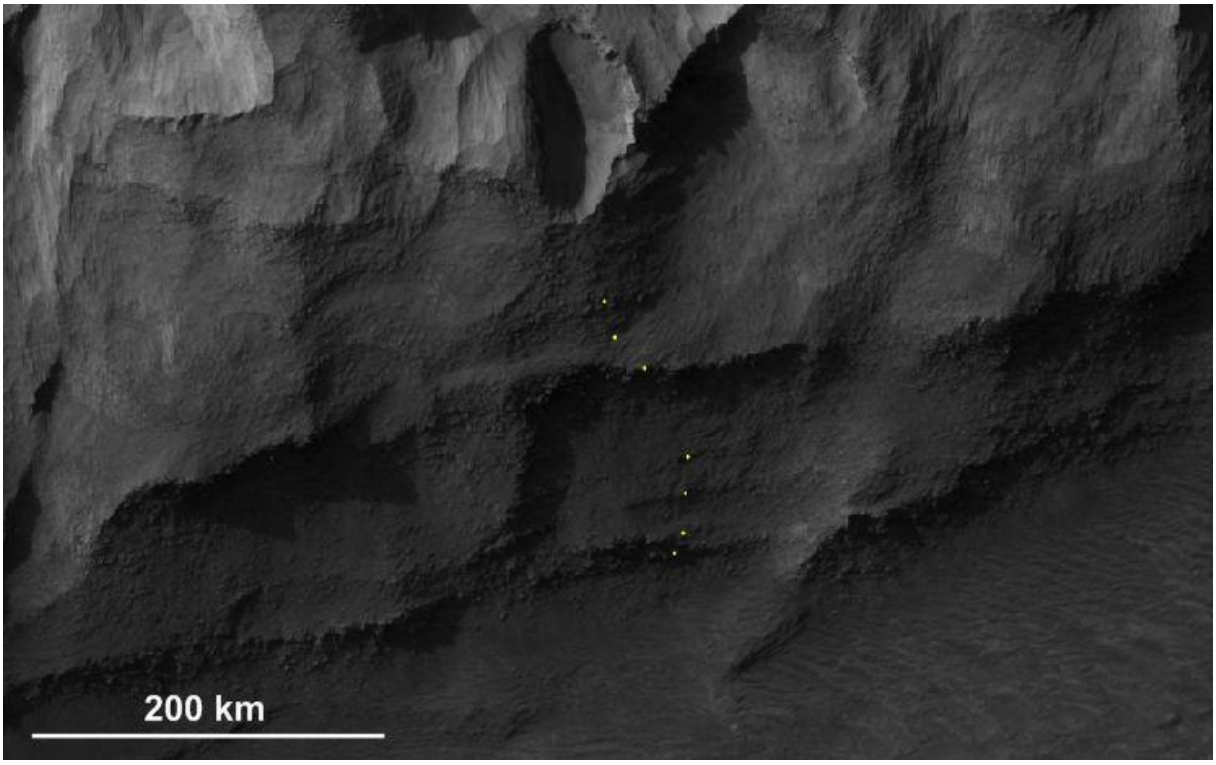

Figure 2.25: Bench edge morphology (H5; bench 3). This image depicts the difficulty in distinguishing between different layers found on the bench edges. In many areas, layers are obscured or indistinguishable; points (small yellow dots) were placed along the layers that could be seen, but resulted in anomalously thick values, likely due to missing certain layers.

2.5.3 Bench Attitudes

The lower benches (1 and 2) were much more steeply inclined and curved than bench 3. In contrast bench 3 has sharp, steep boundaries and is almost horizontal. The elevation ranges of the benches decrease with increased elevation resulting in the more planar nature of bench 3.

Measured bench dips followed the low dip trends set by the ILD layering measured throughout the mound. Generally, the measured strikes followed the bench edges and dipped away from the apex of the ILD (Figure 2.10). The benches could not be attributed to a single layer, but the multiple layer attitude measurements did indicate that the benches parallel the ILD layering.

Moving averages of the layer thicknesses resulted in data peaks coinciding with bench elevations. These peaks suggest that the existence of a bench is controlled by the layer thicknesses and therefore layer thicknesses control the locations of benches. In all instances where these data peaks occur, the layer thicknesses gradually increase upwards in the elevation until they reach the bench edges where they then rapidly decrease (Figure 2.21, 2.22, 2.23). This suggests that layer thickness correlates with layer competency; producing benches near thicker layers within the stratigraphy. These benches therefore cannot be linked to a single layer due to the need for a set of thick layers to form.

2.5.4 Truncations and Irregular Sedimentary Features

Truncations and enigmatic sedimentary features can be identified throughout the Ganges ILD. These truncations can be seen in every HiRISE multiple sets of layers intersect with one another combining into a single set of contiguous layering (examples given in Figure 2.18). These features cannot be linked to a specific sedimentary process but do indicate some form of environmental change.

Twelve large-scale enigmatic sedimentary features (Figure 2.3) were also identified in the HiRISE images. These features disrupt the internal layering of the ILD below in a u-shaped formation and are discussed in more detail in Chapter 3.

2.5.5 Implications for the Formation of the Ganges ILD

The Ganges ILD appears to contain much thinner layering than the other ILDs studied in VM. Overall, layering displayed generally shallow dips with progressively shallower dip angles at the higher elevations. Variations in dip angles also decreased with the increased elevation. The higher dip angles and larger variation in dips at the lower elevations suggests that a topographic high was present on the chasma floor when ILD deposition occurred. These larger dips as well as

the non-horizontal nature of benches 1 and 2 are likely attributed to the draping of sediments over hummocky or built-up basement topography. The hummocky chasma floor or possible topographic high present at the base of the ILD could be due to periodic sediment influxes from different areas. After the sediments were draped over the basement topography, the infilling of sediments appears to have occurred, resulting in the horizontal nature of bench 3 and the shallower dip angles.

Sediment draping and infilling would suggest a depositional nature of the benches, rather than erosional formation mechanisms. Erosional processes likely helped shape the benches after their deposition, resulting in the rough edges of bench 3. These benches cannot be directly linked to a single layer; instead they are linked to sets of increased layer thicknesses. These thicker layers appear to be the result of several large scale depositional cycles occurring in the Ganges Chasma. As demonstrated by the MA calculations (Figures 2.21, 2.22, and 2.23), at least three large scale cycles occurred which coincide with the three benches. One other possible depositional cycle occurred below bench 1 where a large data peak occurred at -2750 m (Figure 2.23). These thick layer sets appear to result in more resistant and competent layering, leading to the defined bench features seen.

The truncations in the sets of layers throughout the Ganges ILD further support the idea that multiple depositional events occurred during ILD formation. A single depositional event would not result in so many layer sets throughout the ILD and the dip attitudes would not vary as drastically.

The large anomalous topographic features that cut through the benches could not be positively defined. In appearance, these features resemble large dykes due to their linear geometry in a north-south transect across the ILD. However, the labelling of the Ganges features

as dykes is contradicted by other studies conducted in VM. The north-south trend of the Ganges features is perpendicular to the standard east-west trends of the VM system [Andrews-Hanna, 2012]. These features resemble dyke formations, but do not follow the volcanic and extensional trends of VM. Due to the cross-cutting of bench morphology, it can be assumed that they were formed after the ILD layering and benches were deposited. These features resulted in the curved and altered ILD form. The separation of the features into shorter segments after the edge of the third bench indicates that erosional processes helped to shape these features into their present configuration.

The majority of the sediments that form the lower two benches, benches 1 and 2, appear to consist of monohydrated sulfates (MHS) while bench 3 sediments consist mainly of polyhydrated sulfates (PHS). Different compositions and hardnesses between the sediments and bench locations could result in differing morphologies and appearances. The PHS composition of bench 3 may be more resistant to erosional mechanisms, aiding in the horizontal nature and rough edges.

The mineralogical composition of the Ganges ILD provides substantial evidence of past hydration due to the water-altered minerals present [*Gendrin, et al.,* 2005; *Bibring, et al.,* 2006]. The abundance of sulfate minerals in the Ganges Chasma implies the presence of a water supply during ILD formation. It seems likely that deposition of the ILD layering occurred in an enclosed basin filled with a shallow lake or ice [*Fueten, et al.,* 2014]. It can be assumed that initially the infill mimicked the possible hummocky basin topography but as stratigraphy built up, the infill became more planar and horizontal. If periodic melting of the ice occurred, it would allow for sediments trapped within and on top of the ice to form thin sediment layers which would be deposited during the seasonal melts. Substantial hiatus' in depositions of hydrated sediments

could result in the thicker layers that appear to form the bench features. Varying hydrated states could have led to differing sediment sizes and resistances.

In Candor Chasma, studies conducted on the dark top layer of the ILD indicated hydrated mineral signatures [*Fueten, et al.*, 2014]. These signatures could indicate that hydrated minerals were imported from an external source after ILD formation or that after volcanic materials were deposited, alteration occurred [*Fueten, et al.*, 2014]. The dark mesa layer on the top of the Ganges ILD has not been studied, however based on similarities between most VM ILDs it can be assumed that the same processes that occurred in Candor Chasma would have also occurred in Ganges Chasma.

2.6 Conclusions

The structure, stratigraphy, geomorphology and mineralogy of the prominent ILD in Ganges Chasma were studied primarily through the use of six HiRISE images and derived digital elevation models. The Ganges layering is overall substantially thinner than other VM ILDs, interrupted by multiple sets of thicker layering. These thick layer sets, identified through the use of moving average calculations, indicate that multiple large scale depositional cycles occurred. These cycles are highly significant due to their repetitive nature, isolated occurrences to Ganges Chasma, and the resulting competent benches identified.

The depositional sediments which form the Ganges ILD appear to originate from a combination of lacustrine and/or snowmelt mechanisms based on the thin layering and large amount of sulfate minerals present. If these processes occurred, it would support the hypothesis theorized by Lucchitta *et al.* [1994] where early, isolated ancestral basins where filed with liquid or frozen lakes. After the linking of these basins through collapse, fluvial, aeolian, and erosional processes [*Tanaka*, 1997*; Fueten, et al.*, 2004; *Grotzinger and Milliken*, 2012] shaped the

mound. The dark capping layer would have accumulated on the top layers of the ILD through the deposition of airborne dust or ash [*Fueten, et al.,* 2014].

The thick layered outcrops, hydrated minerals and extensive geological history record contained within the ILDs and chasma walls of VM create a large interest for future lander missions on Mars [*Chojnacki and Hynek*, 2008] due to ILDs close link to the question of liquid water on Mars [*Flahaut, et al.,* 2010]. Liquid water is a key component in understanding the Martian climate enigma [*Flahaut, et al.,* 2010], causing VM and ILDs to become a target for future missions due to their association with water-altered minerals [*Chojnacki and Hynek*, 2008]. This study demonstrates a strong support for the draping and infilling of sediments through subaqueous and/or lacustrine processes.

2.6.1 Proposed Future Research

Additional HiRISE coverage of the Ganges ILD as well as CRISM data is needed to conduct further layer thickness measurements and mineralogical investigations to obtain a larger database for the entire area. The six HiRISE images used for this analysis provide enough data to suggest possible models and form theories for ILD origin, but many locations on the ILD, such as the median elevations and eastern half, are not represented well with imagery. More image coverage of the eastern ILD could yield more layer thickness and orientation information pertaining to the high elevations where dust cover is an issue presently. Additionally, more coverage of the median elevations could help to fill in some of the data gaps found which may reveal specific trends. Further CRISM data coverage is greatly needed and would help to create a complete mineralogical map of the Ganges ILD allowing for in-depth analysis. For this study, very little of the ILD was represented by imagery making mineralogical investigation difficult.

Comparisons of layer thicknesses and orientations with other VM ILDs as well as ILDs and mounds found in craters and chasmata outside of VM would help to validate any findings and theories discovered in Ganges. By comparing the layer data from this report to layer data from other ILDs could unearth conclusive ILD formation processes and mechanisms. These comparisons could clarify whether the Ganges Chasma ILD is an anomaly with thin layering in VM as suggested by the limited comparisons available presently, or whether the thin layering seen occurs more frequently across the Mars surface.

2.7 References

Andrews-Hanna, J.C., R.J. Phillips, and M.T. Zuber. (2007). Meridiani Planum and the Global Hydrology of Mars, *Nature: Letters, 446*, doi:10.1038/nature05594.

Andrews-Hanna, J.C. (2012). The Formation of Valles Marineris: 1. Tectonic Architecture and the Relative Roles of Extension and Subsidence, *Journal of Geohpysical Research, 117, E03006*, doi: 10.1029/2011JE003953.

Ansan, V., *et al.* (2011). Stratigraphy, Mineralogy, and Origin of Layered Deposits inside Terby Crater, Mars, *Icarus, 211*, 273-304, doi:10.1016/j.icarus.2010.09.011.

Bibring, J. P., Y. Langevin, J.F. Mustard, F. Poulet, R. Arvidson, A. Gendrin, B. Gondet, N. Mangold, P. Pinet, F. Forget, and the OMEGA Team. (2006), Global mineralogical and aqueous Mars history derived from OMEGA/Mars Express data, *Science, 312*, 400–404, doi:10.1126/science.1122659.

Blasius, K.R., J.A. Cutts, J.E. Guest, and H. Masursky. (1977). Geology of the Valles Marineris; first analysis of imaging from the Viking 1 orbiter primary mission, *Journal of Geophysical Research, 82*, 4067–4091.

Blue Marble Geographics. (1993-2014). *Global Mapper, LLC [computer software]*. Developed by Mike Childs in 2011, Gardiner, Maine.

Broxton, M. J. and L. J. Edwards (2008) The Ames Stereo Pipeline: Automated 3D Surface Reconstruction from Orbital Imagery, *Lunar Planet Sci. XXXIX*, Abstract 2419.

Calvert, L., F. Fueten, J. Flahaut, R. Stesky, A.P. Rossi, E. Hauber, and C. Quantin-Nataf. (2013). Layer Attitude and Thickness Measurements of Three Interior Layered Deposits within Capri Chasma, Mars. *Lunar Planet Sci. XLIV*, Abstract 1069.

Chapman, M.G., and J. L. Smellie. (2007). Mars Interior Layered Deposits and Terrestrial Sub-Ice Volcanoes Compared: Observations and Interpretations of Similar Geomorphic Characteristics, in *The Geology of Mars: Evidence from Earth-Based Analogs*, pp. 178-210, Cambridge Univ. Press, UK.

Chojnacki, M., and B. M. Hynek. (2008). Geological Context of Water-Altered Minerals in Valles Marineris, Mars, *Journal of Geophysical Research, 113*, E12005, doi: 10.1029/2007JE003070.

Christensen, P.R., E. Engle, S. Anwar, S. Dickenshied, D. Noss, N. Gorelick, and M. Weiss-Malik. (2009). JMARS – A Planetary GIS, *American Geophysical Union*, Abstract IN22A-06.

Christensen, P., *et al.* (2001). Mars Global Surveyor Thermal Emission Spectrometer experiment: Investigation description and surface science results, *Journal of Geophysical Research, 106 (E10)*, 23823–23871.

Craddock, R.A., R.P. Irwin III, A. D. Howard, and D. W. Latham. (2013). The History of Water on Early Mars: the Sun, the Wind, and the Rain, *Lunar Planet. Sci. XLIV*, Abstract 1984.

Edgett, K. S. (2009). Mars Reconnaissance Orbiter (MRO) context camera (CTX) observations regarding volcanic landforms on Mars, *Geological Society of America, 41 (E7)*, 708.

Fenton, L.K., T.I. Michaels, and R.A. Beyer. (2012). Aeolian Sediment Sources and Transport in Ganges Chasma, Mars: Morphology and Atmospheric Modeling, *Lunar Planet. Sci. XLIII*, Abstract 2441.

Flahaut, J., C. Quantin, P. Allemand, and P. Thomas. (2010). Morphology and Geology of the ILD in Capri/Eos Chasma (Mars) from Visible and Infrared Data, *Icarus, 207*, 175-185, doi:10.1016/j.icarus.2009.11.019.

Fueten, F., R.M. Stesky, and P. MacKinnon. (2004). Structural Attitudes of Large Scale Layering in Valles Marineris, Mars, Calculated from Mars Orbiter Laser Altimeter Data and Mars Orbiter Camera Imagery, *Icarus, 175*, 68-77, doi: 10.1016/j.icarus.2004.11.010.

Fueten, F., R. Stesky, P. Mackinnon, E. Hauber, K. Gwinner, F. Scholten, and T. Zegers. (2006). A Structural Study of an Interior Layered Deposit in Southwestern Candor Chasma, Valles Marineris, Mars, Using High Resolution Stereo Camera from Mars Express, *Geophysical Research Letters, 33*, L07202, doi: 10.1029/2005GL025035.

Fueten, F., R. Stesky, P. MacKinnon, E. Hauber, T. Zegers, K. Gwinner, F. Scholten, and G. Neukum (2008), Stratigraphy and structure of interior layered deposits in west Candor Chasma, Mars, from High Resolution Stereo Camera (HRSC) stereo imagery and derived elevations, *Journal of Geophysical Research, 113*, E10008, doi:10.1029/2007JE003053.

Fueten, F., H. Racher, R. Stesky, P. MacKinnon, E. Hauber, P.C. McGuire, T. Zegers, and K. Gwinner. (2010). Structural Analysis of Interior Layered Deposits in Northern Coprates Chasma, Mars, *Earth and Planetary Science Letters, 294*, 343-356, doi:10.1016/j.epsl.2009.11.004.

Fueten, F., J. Flahaut, L. Le Deit, R. Stesky, E. Hauber, and K. Gwinner. (2011). Interior Layered Deposits within a Perched Basin, Southern Coprates Chasma, Mars: Evidence for their Formation, Alteration, and Erosion, *Journal of Geophysical Research, 116*, E02003, doi: 10.1029/2010JE003695.

Fueten, F., J. Flahaut, R. Stesky, E. Hauber, and A. P. Rossi (2014), Stratigraphy and mineralogy of Candor Mensa, West Candor Chasma, Mars: Insights into the geologic history of Valles Marineris, *Journal of Geophysical Research Planets, 119*, doi:10.1002/2013JE004557.

Gendrin, A., N. Mangold, J.P. Bibring, Y. Langevin, B. Gondet, F. Poulet, G. Bonello, C. Quantin, J. Mustard, R. Arvidson, and S. LeMouélic (2005). Sulfates in Martian Layered Terrains: The OMEGA/Mars Express View, *Science, 307*, 1581-1591.

Harland, D.M. (2005). *Water and the Search for Life on Mars*, Praxis Publishing, New York.

Ismailos, C., F. Fueten, R. Stesky, J. Flahaut, A. Rossi, and E. Hauber. (2012). Layer Thickness Determination of the Interior Layered Deposit within Ganges Chasma, Mars, *Lunar Planet. Sci. XLIII,* Abstract 1533.

Kite, E. S., I. Halevy, M. A. Kahre, M. J. Wolff, and M. Manga (2013), Seasonal melting and the formation of sedimentary rocks on Mars, with predictions for the Gale Crater mound, *Icarus, 223,* 181-210, doi:10.1016/j.icarus.2012.11.034.

Komatsu, G., G.G. Ori, P. Ciarcelluti, and Y.D. Litasov. (2003). Interior Layered Deposits of Valles Marineris, Mars: Analogous Subice Volcanism Related to Baikal Rifting, Southern Siberia, *Planetary and Space Science, 52,* 167-187, doi: 10.1016/j.pss.2003.08.003.

Lucchitta, B. K., A. S. McEwen, G. D. Clow, P. E. Geissler, R. B. Singer, R. A. Schultz, and S. W. Squyres (1992). The canyon system on Mars, in Mars, pp. 453–492, Univ. of Ariz. Press, Tucson.

Lucchitta, B.K., Isbell, N.K., and Howington-Kraus, A. (1994). Topography of Valles Marineris: Implications for Erosional and Structural History, *Journal of Geophysical Research, 99 (E2),* 3783-3798.

Malin, M.C., and K. S. Edgett. (2000). Sedimentary Rocks of Early Mars, *Science, 290,* 1927-1937, doi: 10.1126/science.290.5498.1927.

Microsoft Corporation. (2010). *Microsoft Office: Excel [Computer Software*]. Redmond, Washington.

Milliken, R.E., G.A. Swayze, R.E. Arvidson, J.L. Bishop, R.N. Clark, B.L. Ehlmann, R.O. Green, J.P. Grotzinger, R.V. Morris, S.L. Murchie, J.F. Mustard, and C. Weitz. (2008). Opaline Silica in Young Deposits on Mars, *Geology, 36 (E11),* 847-850, doi: 10.1130/G24967A.1.

Moratto, Z. M., M. J. Broxton, R. A. Beyer, M. Lundy, and K. Husmann (2010) Ames Stereo Pipeline, NASA's Open Source Automated Stereogrammetry Software, *Lunar Planet. Sci. XLI,* Abstract 2364.

Murchie, S., *et al.* (2007), Compact Reconnaissance Imaging Spectrometer for Mars (CRISM) on Mars Reconnaissance Orbiter (MRO), *Journal of Geophysical Research, 112,* E05S03, doi:10.1029/2006JE002682.

NASA (2007). *Mars Global Surveyor: MOLA MEGDRs.* Obtained from: http://geo.pds.nasa.gov/missions/mgs/megdr.html.

Novakovic, N., F. Fueten, J. Flahaut, R. Stesky, A.P. Rossi, and E. Hauber. (2013). Layer Attitude and Thickness Measurements of the Three Interior Layered Deposits Mounds within Juventae Chasma, Mars. *Lunar Planet. Sci. XLIV,* Abstract 1068.

Okubo, C.H., K.H. Lewis, A.S. McEwen, and R.L. Kirk. (2008). Relative Age of Interior Layered Deposits in Southwest Candor Chasma Based on High-Resolution Structural Mapping, *Journal of Geophysical Research, 113*, E12002, doi: 10.1029/2008JE003181.

Pangaea Scientific (2006-2011). *Orion: Orientation Hunter [computer software]*. Supported by Canada Centre for Remote Sensing, Natural Resources Canada. Brockville, Ontario, Canada.

Pentecost, A. (2005). Travertine. 445 pp., Springer-Verlag, New York.

Roach, L.H., J.F. Mustard, S.L. Murchie, J.P. Bibring, F. Forget, K.W. Lewis, O. Aharonson, M. Vincendon, and J.L. Bishop. (2009). Testing Evidence of Recent Hydration State Change in Sulfates on Mars, *Journal of Geophysical Research, 114*, E00D02, doi: 10.1029/2008JE003245.

Rossi, A. P., G. Neukum, M. Pondrelli, S. van Gasselt, T. Zegers, E. Hauber, A. Chicarro, and B. Foing (2008), Large-scale spring deposits on Mars?, *Journal of Geophysical Research, 113*, E08016, doi:10.1029/2007 JE003062.

Schultz, R.A. (1998). Multiple-process origin of Valles Marineris basins and troughs, Mars. *Planetary Space Science, 46*, 827–834.

Pangaea Scientific. (2014). *Spheristat 3.2 [computer software]*. Obtained from: http://www.pangaeasci.com.

Tanaka, K.L. (1997). Origin of Valles Marineris and Noctis Labyrinthus, Mars, by Structurally Controlled Collapse and Erosion of Crustal Materials, *Lunar Planet. Sci. XXVIII*, Abstract 1169.

Wang, A., Freeman, J.J., & Arvidson, R. (2008). Study of Two Structural Polymorphs of MgSO4•H2O by Raman, IR, XRD, and Humidity Buffer Experiments- Implication for Martian Kieserite, *Lunar Planet. Sci. XXXIX*, Abstract 2172.

Zeitler, W., T. Ohlhof, & H. Ebner. (2000). Recomputation of the Global Mars Control-Point Network, *Photogrammetric Engineering & Remote Sensing, 66 (2*), 155-161.

Chapter 3: Origin and Formation of Enigmatic Sedimentary Features Identified in Ganges Chasma, Valles Marineris, Mars

3.1 Introduction

The Valles Marineris (VM) canyon system, located in the equatorial region of Mars [*Harland,* 2005], contains numerous Interior Layered Deposits (ILDs) in many of its chasmas [*Flahaut, et al*., 2010]. Ganges Chasma, at the far eastern end of VM (Figure 3.1) [*Fenton, et al.,* 2012], contains one large free standing ILD which is dominated by water-altered minerals such as hematite and hydrated sulfates [*Chapman and Smellie,* 2007; *Chojnacki and Hynek,* 2008; *Ismailos, et al.,* 2012]. Within the generally parallel layering of the ILD, several features were observed in which sequences of parallel, non-horizontal layering disrupts the general ILD layering. These features are the focus of this study.

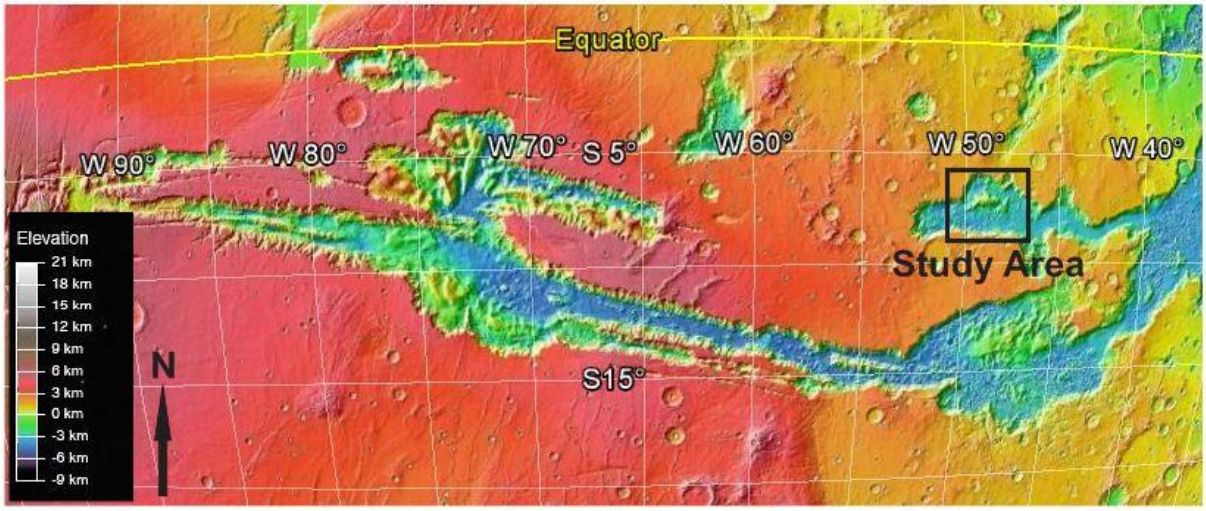

Figure 3.1: MOLA DTM of the Valles Marineris Canyon system. The study area, Ganges Chasma, is identified by the black box at the eastern edge of VM. Image was obtained from Google Earth.

Within the six HiRISE images used for this study, twelve large-scale enigmatic sedimentary features were identified in four of the images (Figure 3.2, Figure 3.3). This paper reports observations of these features and compares them to similar terrestrial deposits in order to propose formation mechanisms for these Ganges ILD features.

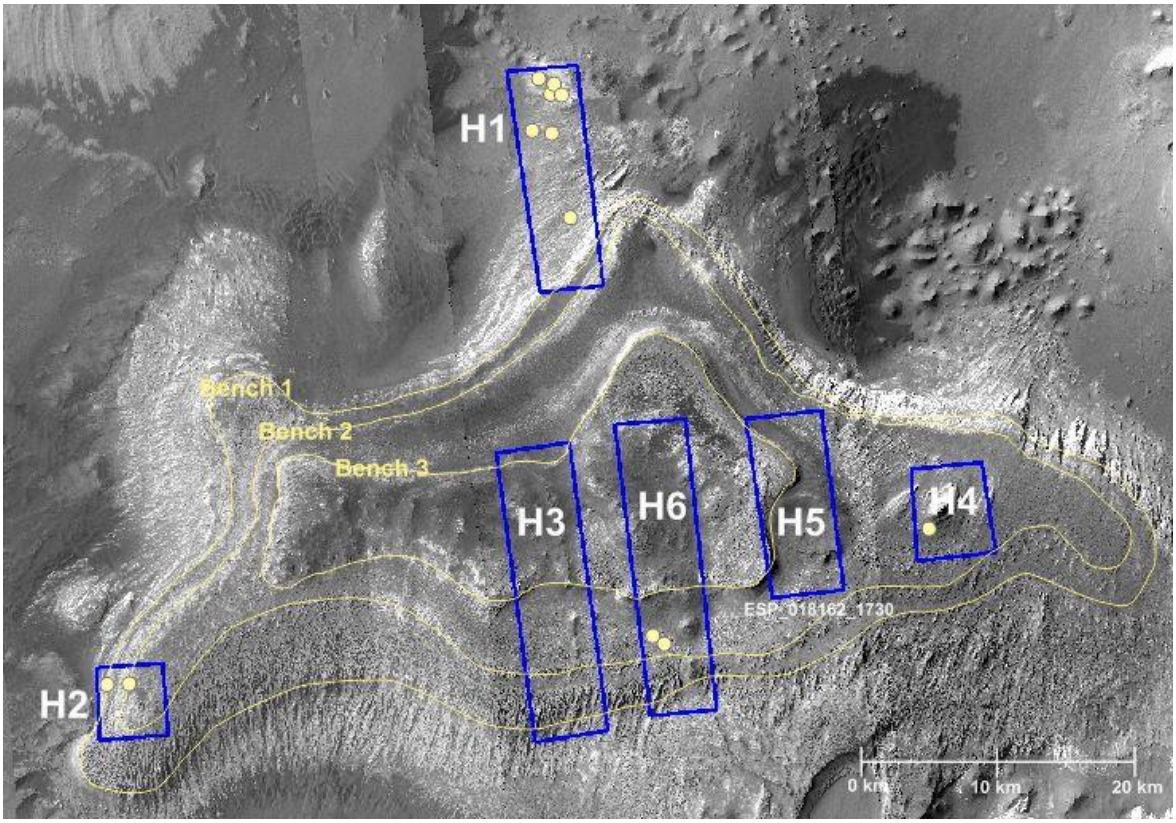

Figure 3.2: Ganges Chasma ILD with HiRISE image footprints. The locations of the twelve slump features are represented by yellow points. The three ILD benches are represented by yellow dashed lines.

3.2 Methodology

Six HiRISE stereo pairs (1 m/pixel) were overlain on a CTX image mosaic; PSP_006519_1730/ PSP_007020_1730 (H1), ESP_013059_1725/ESP_012993_1725 (H2), PSP_002550_1725/ PSP_003618_1725 (H3), ESP_011648_1730/ESP_011582_1730 (H4), ESP_018162_1730/ ESP_018663_1730 (H5), and PSP_007877_1725/PSP_007521_1725 (H6). These images were used to calculate 50 cm/pixel HiRISE DTMs from each image using the NASA Ames Stereo Pipeline [*Broxton and Edwards*, 2008; *Moratto, et al.*, 2010].

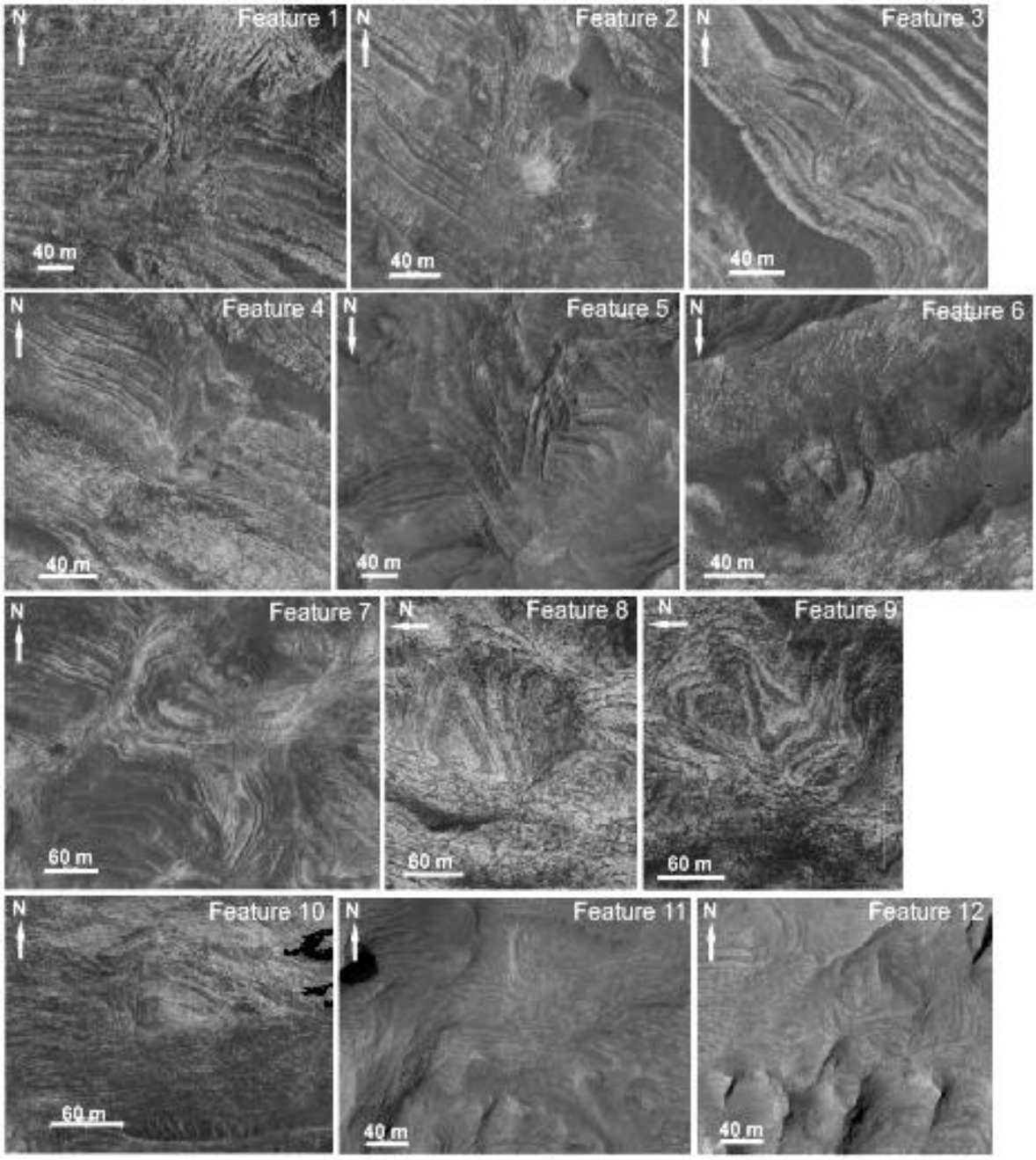

Figure 3.3: All twelve identified features. Features 1-7 found in HiRISE image H1, features 8 and 9 found in HiRISE image H2, feature 10 found in HiRISE image H4, and features 11 and 12 found in HiRISE image H6. All images are arranged so that the highest elevation is at the top of each image; north arrows indicate direction. Elevations, widths, directions, degrees of slope, and classification are recorded in Table 3.1.

The programs Orion [*Pangaea Scientific*, 2006-2011], Global Mapper [*Blue Marble Geographics*, 1993-2014], Microsoft Excel [*Microsoft Corporation*, 2010] and CorelDraw [*Corel*, 1989-2014] were used to obtain, analyze, and present the data. Initially, the features were

discovered when Orion was used to calculate layer orientation measurements. After initial recognition, all six HiRISE images were systematically searched for additional similar features, resulting in the identification of twelve such features (Figure 3.2, Figure 3.3). Current topographic slope angles of the features were estimated in cross-sections using Global Mapper. Global Mapper was also used to measure the apparent widths of each feature by using the basic measuring tool (Figure 3.4).

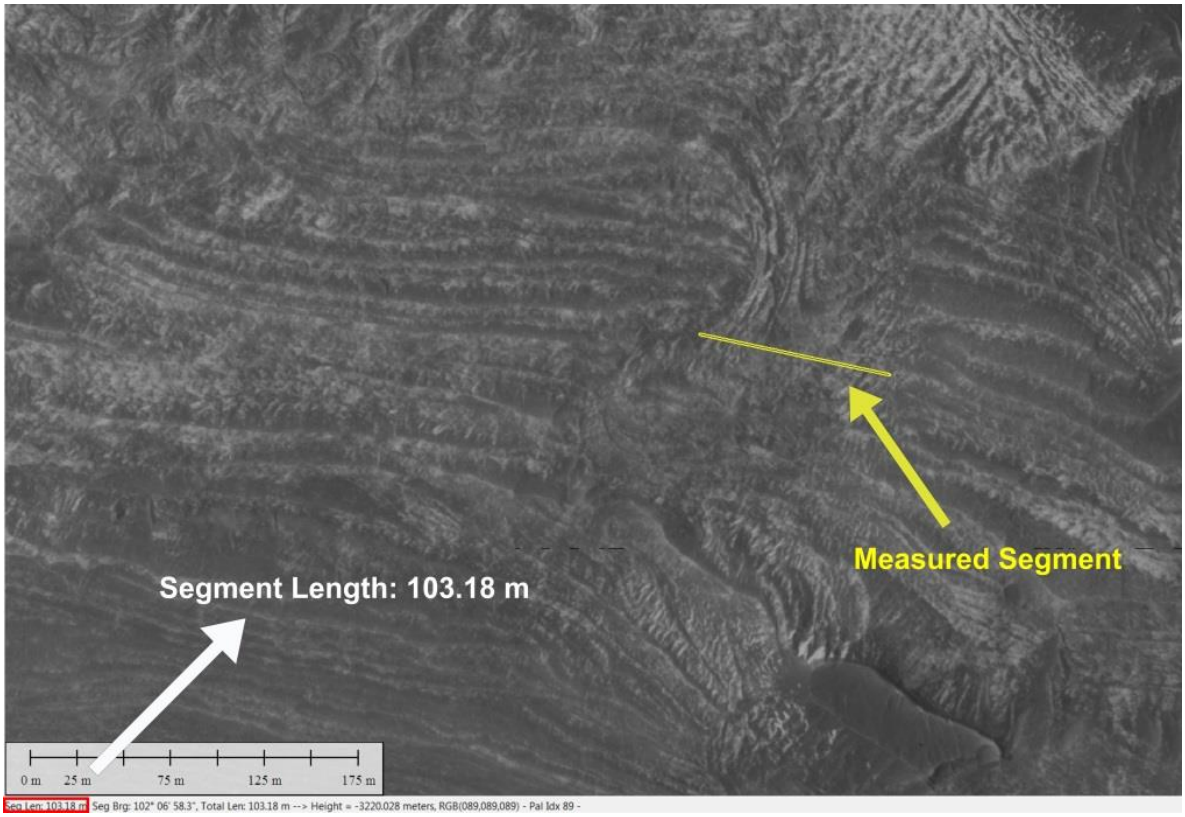

Figure 3.4: Width measurement process of features conducted in Global Mapper. The measurement segment (yellow line) is placed across the feature while the program calculates the segment length (red box, bottom left).

3.3 Enigmatic Sedimentary Features

A total of twelve isolated enigmatic sedimentary features were identified (Figure 3.3) in four of the six HiRISE images (Figure 3.2). The features generally occur along the margins of the ILD at lower elevations, typically in areas of low dust cover and low topographic slope where they can be easily identified.

As seen in plan view, each feature consists of parallel, non-horizontal layering resulting in a u-shaped geometry which truncates the underlying horizontal ILD layering. The widths of the features range from 10s to 100s of metres. The features are not the result of a local topographic effect, as local topography around the features is smooth and planar in most instances.

3.4 Detailed Description of Enigmatic Feature

3.4.1 Locations, Sizes and Geometry

Seven of the twelve enigmatic features were identified (Figure 3.2, Figure 3.3) within image H1. They occur at elevations ranging from -3108 m to -705 m. Seven of the features are within approximately 750 m of elevation of each other (from -3108 m to -2379 m) while the other five occur within approximately 800 m of elevation of each other (-1481 m to -705 m). All of the features are below an elevation of -700 m elevation, while the elevation at the top of the ILD is about 250 m.

With respect to the benches discussed in chapter 2, seven of the features are below the lowest bench 1, two are between benches 1 and 2, and three are on the plateau of bench 2; no features were found above bench 3.

Table 3.1 summarizes the statistics for each feature, including the width, depth, elevation, and classification. The elevation for each feature was identified using the Global Mapper program. The widths were measured across the u-shaped form parallel to the trace of the normal ILD layering and ranged from 48 m to 152 m (Table 3.1, Figure 3.4). The apparent width values are estimates of each feature and could be statistically skewed. The true long axes of the features and the angle at which the features are located in relation to the current topography are unknown; if the current topography is transecting the features at a wide angle, the features could appear much wider than they actually are. The depths of the features were measured by calculating the difference in elevation between the top layer and the bottom layer of each feature.

Feature	Image	Elevation at Slump Centre (m)	Depth of Feature (m)	Apparent Width (m)	Depth to Width Ratio	Classification
1	H1	-3108	6	103	1:17.2	Basic U-Shaped
2	H1	-3072	10	66	1:6.6	Basic U-Shaped
3	H1	-3003	0.3	49	1:163.3	Basic U-Shaped
4	H1	-3069	68	48	1.4:1	Basic U-Shaped
5	H1	-3036	10	120	1:12	Basic U-Shaped
6	H1	-2944	16	68	1:4.3	Minimal or Understated
7	H1	-2379	5	152	1:30.4	Basic U-Shaped
8	H2	-1481	28	105	1:3.8	Bi-Directional
9	H2	-1237	18	74	1:4.1	Bi-Directional
10	H4	-705	13	60	1:4.6	Minimal or Understated
11	H6	-1024	2	126	1:63	Basic U-Shaped
12	H6	-1067	2	86	1:43	Basic U-Shaped

Table 3.1: Size and Elevation statistics for individual features. Data collected from Global Mapper, Excel and Orion software.

These measurements were important to be able to compare the Ganges features with similar features identified in terrestrial and other Martian studies. The shape of each feature was classified according to a system discussed in detail below (Table 3.1).

A possible correlation between feature width and feature elevation was expected, such as an increased width with increased elevation, yet no correlation was found (Figure 3.5). This concludes that elevation does not appear to be a controlling factor in forming these features.

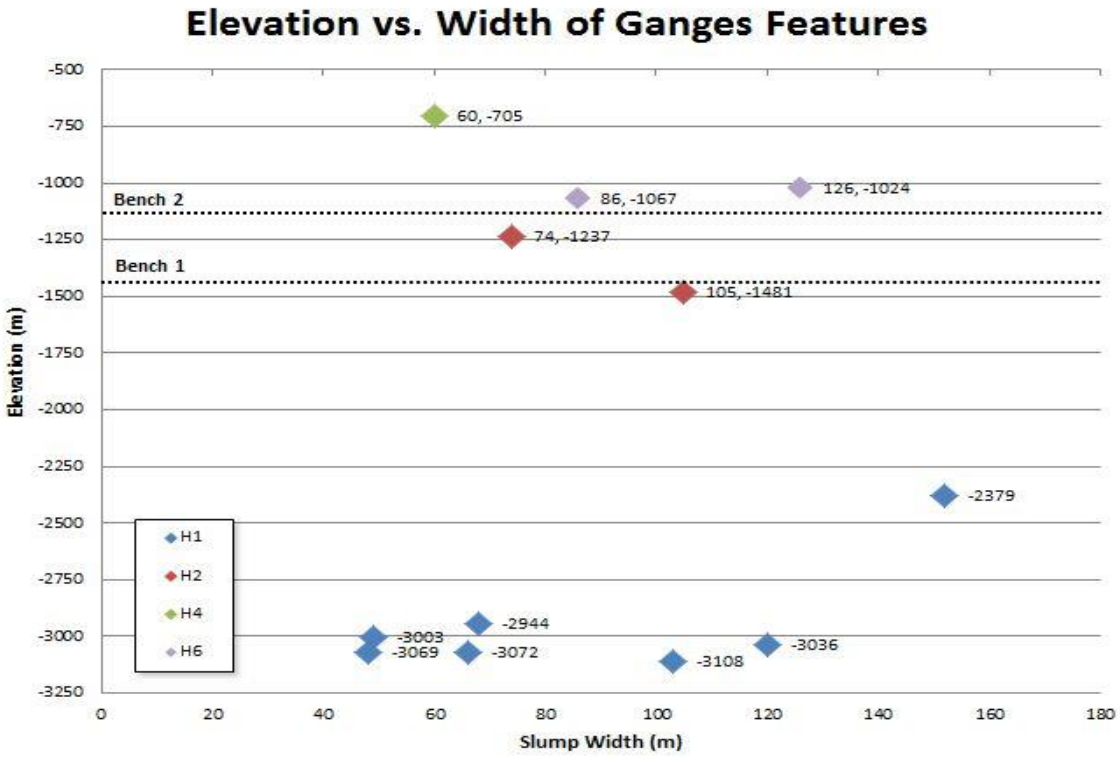

Figure 3.5: Graphed widths and elevations of individual features.

In Table 3.2, the current and paleo-slopes of the features are summarized to understand what controlled the formation of the features. Paleo-slope, defined as the topographic slope at the time of ILD formation, is approximately parallel to the deposited layering and is assumed to have not undergone rotation. Current topographic slope of the surrounding areas of the features is generally low; ranging from less than 6º where the topography appears flat, up to a maximum of

15º. Providing that no layer rotation occurred, the paleo-slope can be estimated by the attitude of the layers surrounding the feature locations (Figure 3.6). Figure 3.6 depicts the measured layering surrounding three of the features (Features 1, 3, and 4); these layers were measured for all possible features. An average of the measured dip values surrounding each feature was calculated (Table 3.2). The paleo-dips ranged from approximately 8.5º to 23º; the paleo-slope of three of the features could not be estimated. In five instances, the current and paleo-slopes have similar values (features 1-3, 5, and 10), three features show very different degrees of slope between the current and paleo-slopes (features 4, 8, and 9), and in four instances, the current and paleo-slopes could not be compared because the current and/or paleo-slopes could not be measured (features 6, 7, 11, and 12) (Table 3.2).

Feature	Image	Approximate Paleo-Slope	Paleo-Slope Direction	Current Topographic Slope	Current Topographic Direction (Down)
1	H1	10.5º	Northwest	8º	West
2	H1	13.5º	North	15º	West
3	H1	11º	North	13º	West
4	H1	14.5º	North	6º	West
5	H1	8.5º	West	12º	Northwest
6	H1	--	--	15º	North-Northwest
7	H1	18º	East-Northeast	--	Chaotic terrain; no definitive direction
8	H2	23º	West	8º	West
9	H2	18º	Northwest	10º	Southwest
10	H4	10.5º	South	11º	South-Southwest
11	H6	--	--	8º	East (minor)
12	H6	--	--	--	Feature located in depression; no definitive direction

Table 3.2: Slope statistics obtained for individual features. Data collected from Global Mapper, Excel and Orion software.

For five of the features (features 1-4, and 8), the dip direction of bedding in the areas surrounding the features is approximately parallel to the vertical axis which runs through the center of each feature. In these areas, the features point downslope and sit at 180º to the paleo-

slope direction. Three of the twelve features sit perpendicular to the paleo-slope direction. Feature 10 is the only feature where the downslope direction of the curved portion of the feature coincides with the paleo-slope.

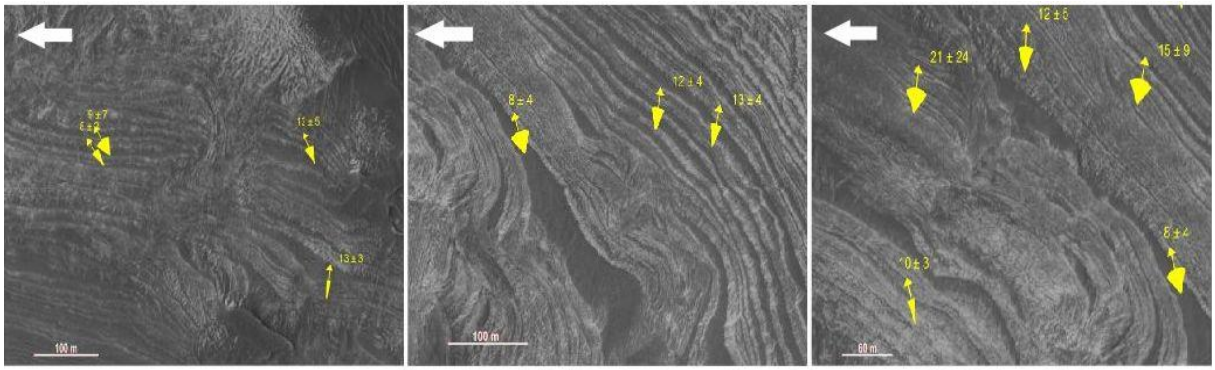

Figure 3.6: Strike and dip values measured in layering surrounding three slump features to obtain approximation of paleo-slope. White arrow indicates downslope direction.

To better understand the 3D geometry of the features, a schematic cross-section was constructed for the best developed example, feature 1 (Figure 3.7). This cross-section demonstrates that the features are not just constructed of surface sediments; they are much more complex in nature. The sediments that comprise the features interact with and cut through the normal ILD layering. The majority of features identified are found in two major elevation ranges (Figure 3.8). This limitation indicates that the features are controlled either by elevation or by identification difficulties due to obscured ILD layers or limited HiRISE data. In the region where features 1-4 are located, the topographic slope dips towards the main ILD mound, in contrast to the normal trend where the layering dips away from the main ILD. There is no distinction that this area is a subsidiary mound; topographic lows and highs are normal at the furthest reaches of the ILD where these features are located.

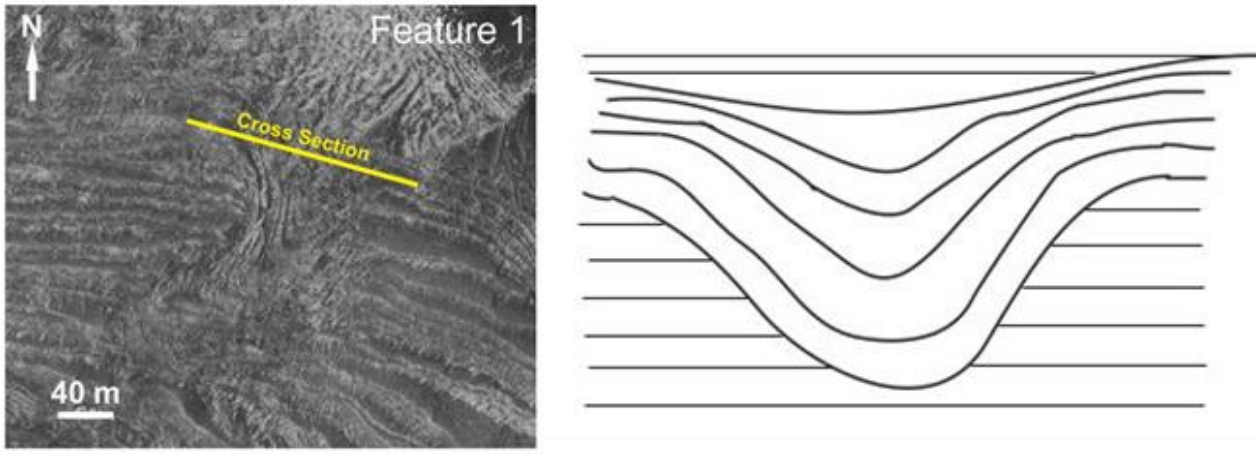

Figure 3.7: Schematic cross section analysis of the first Ganges feature. The left image is a HiRISE image of the feature where the yellow line represents where the cross section occurs. The right image is a constructed cross section schematic that represents what the Ganges features would look like under the surface.

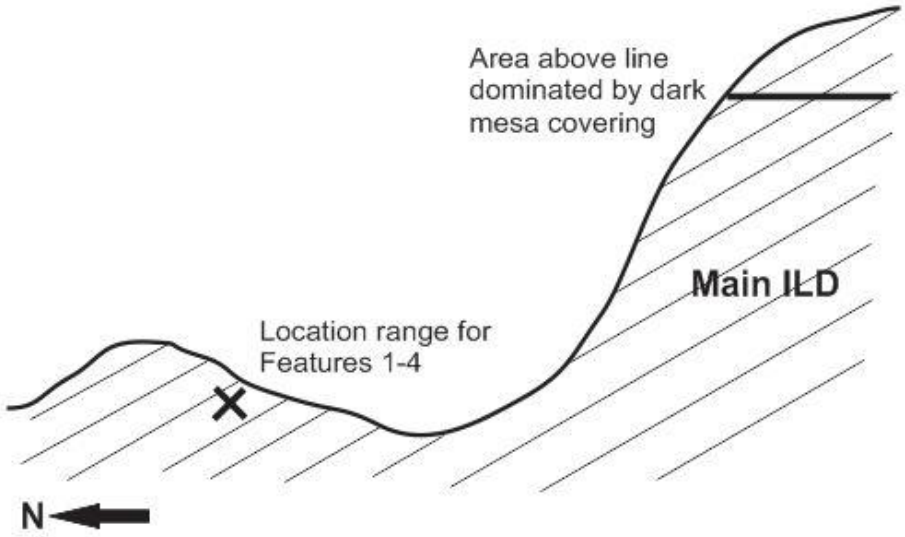

Figure 3.8: Schematic topographic cross-section depicting the location of the four main features (Features 1-4) in relation to the main ILD. Approximate level of where dark mesa dominates is also depicted. Above this line, no features were identified.

3.4.2 Feature Classifications

To gain a better understanding of the variability of the enigmatic features, they were grouped into three classes. Overall, the features display the same general appearance of folded or curved bedding which truncate the layering stratigraphically below them (Figure 3.9), but three distinct types of features were identified.

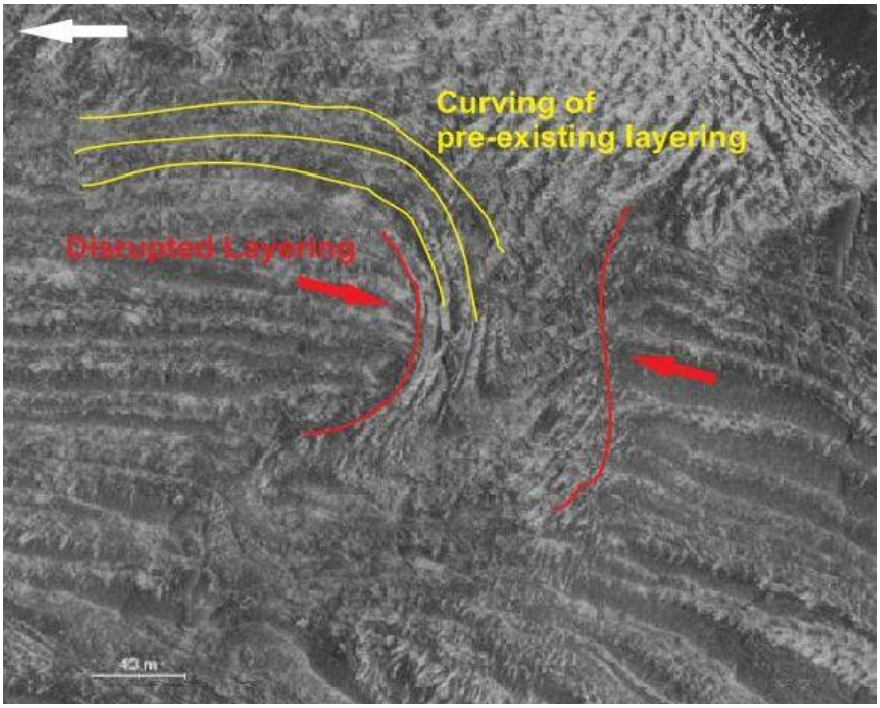

Figure 3.9: The curved nature of the pre-existing layering and the disrupted layering due to the sediments of the Ganges features. White arrow indicates downslope direction.

Three broad classes were recognized based on differing appearances and compositions of the features: 1) Basic U-Shaped, 2) Bi-Directional, and 3) Minimal or Understated (Table 3.1; Figure 3.10). Class 1 features have well-defined boundaries, distinguished layering, and an overall U, or sometimes V, shape. This class contains the majority of the identified features based on the relative ease with which they can be recognized. The second class is represented by features that appear to curve in two separate directions. This class may be the remnants of

multiple features directly adjacent to one another which have been eroded and obscured, resulting in the dual feature. The layers are much less defined than those in Class 1 and generally have a more rounded layer trace. The features in Class 3 have the same general appearance and shape as those in Class 1; however, the feature boundaries are much less defined and the surrounding topography and layering is minimally disturbed (Figure 3.10). The less defined layering in this class could be due to a lack of exposed layering or a high dust cover.

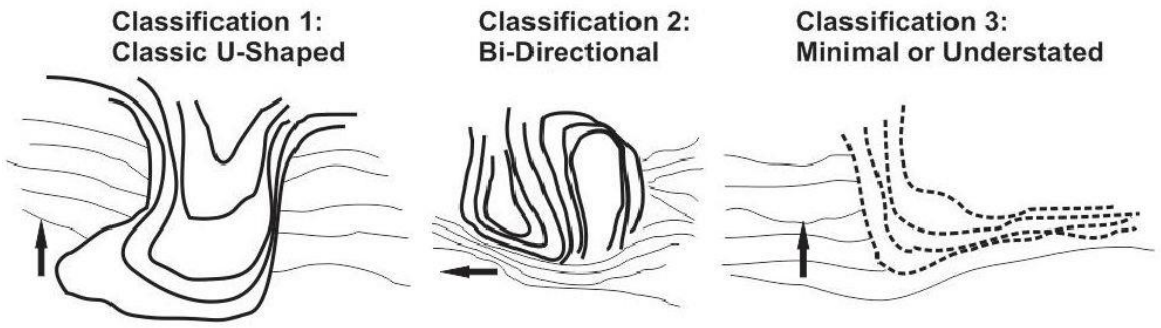

Figure 3.10: Representations of the three feature classifications. The dark, bold lines represent the features and the thin lines represent the surrounding layering. Dashed lines were used in Classification 3 to represent the hazy boundaries between the features and surrounding layering. All representations are arranged so that the highest elevation as at the top of the image; black arrows indicate north.

Figure 3.11 depicts the layering geometry of each of the three classifications. The U-Shaped classification (Figure 3.11, A-D) can be easily identified. Feature 10 (Figure 3.11, E and F) representing the Minimal or Understated class, is difficult to identify without enhancing the differing layer types. The Bi-Directional Classification (Figure 3.11 G and H) are easy to identify without the enhanced boundaries, but Figure 3.11 illustrates their overall shape better. The overall appearance of the features in Classifications 1 and 3 are very similar, as the defined boundary layers in classification 1 are comparable to the hazy or blurred boundaries in classification 3 (Figure 3.11).

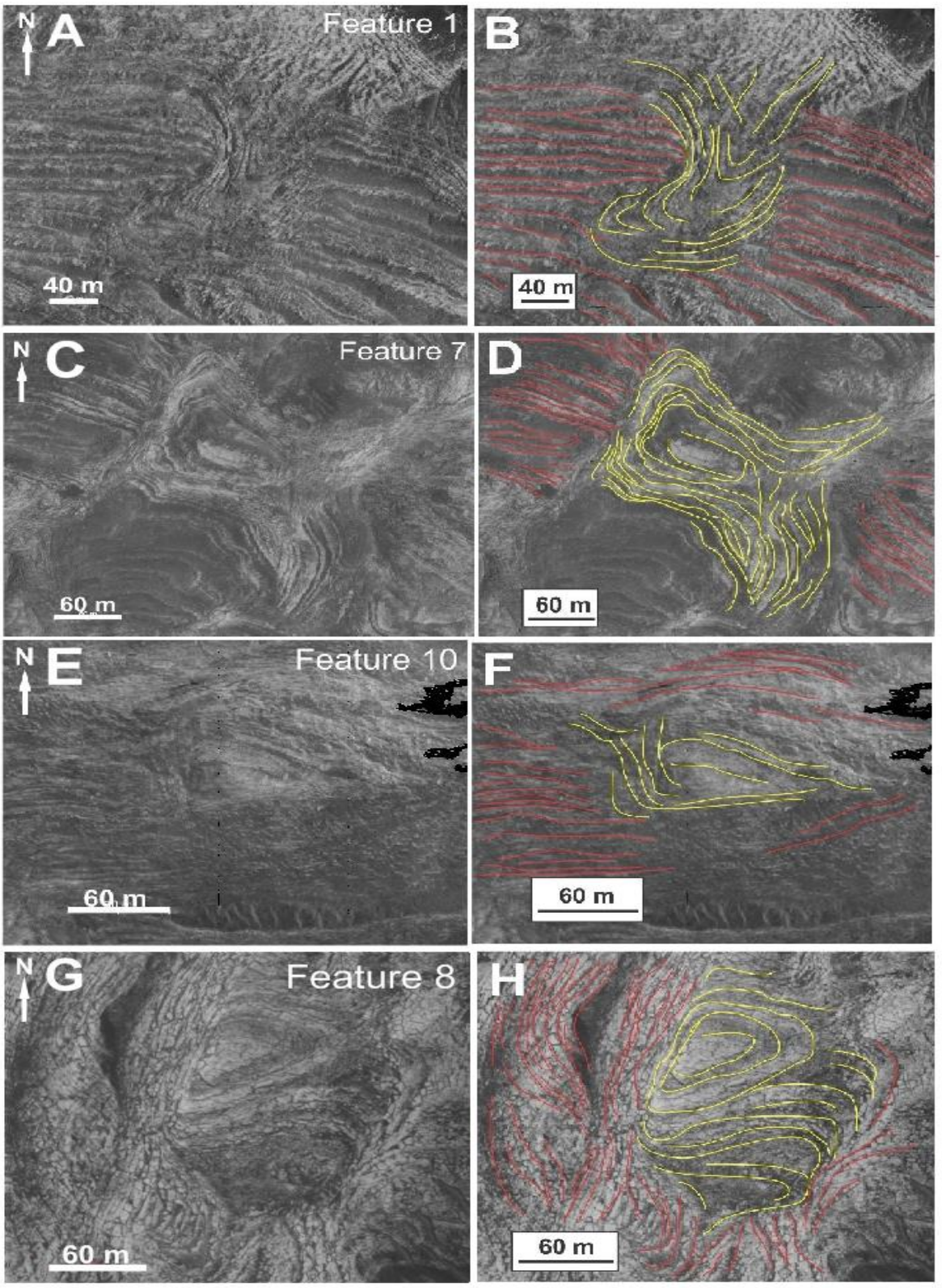

Figure 3.11: Four outlined features comparing normal ILD layering to feature layering. Feature 1 (A & B) and Feature 7 (C & D) represent the Classic U-Shaped form. Feature 10 (E & F) represent the Minimal or Understated slump form. Feature 8 (G & H) represents the Bi-Directional slump form. Red lines represent normal layering; yellow lines represent layering in the Ganges features; white arrows represent the downslope direction.

Features 1-5, 7, 11 and 12 are Class 1 structures; all show clear U/V shaped forms and have distinctive boundaries. Feature 1 is the most distinctive of all features found and serves as the "best example" of Class 1. Feature 8 and 9 are Class 2 structures. Feature 9 shows especially prevalent bi-directional features. Features 6 and 10 are categorized as Class 3 structures due to their indistinct feature boundaries as well as the minimal disturbance of surrounding layering. These two features were the most difficult to identify.

Other features throughout the six HiRISE sites were similar in appearance, yet did not truncate layering around or below them and were therefore not included (Figure 3.12).

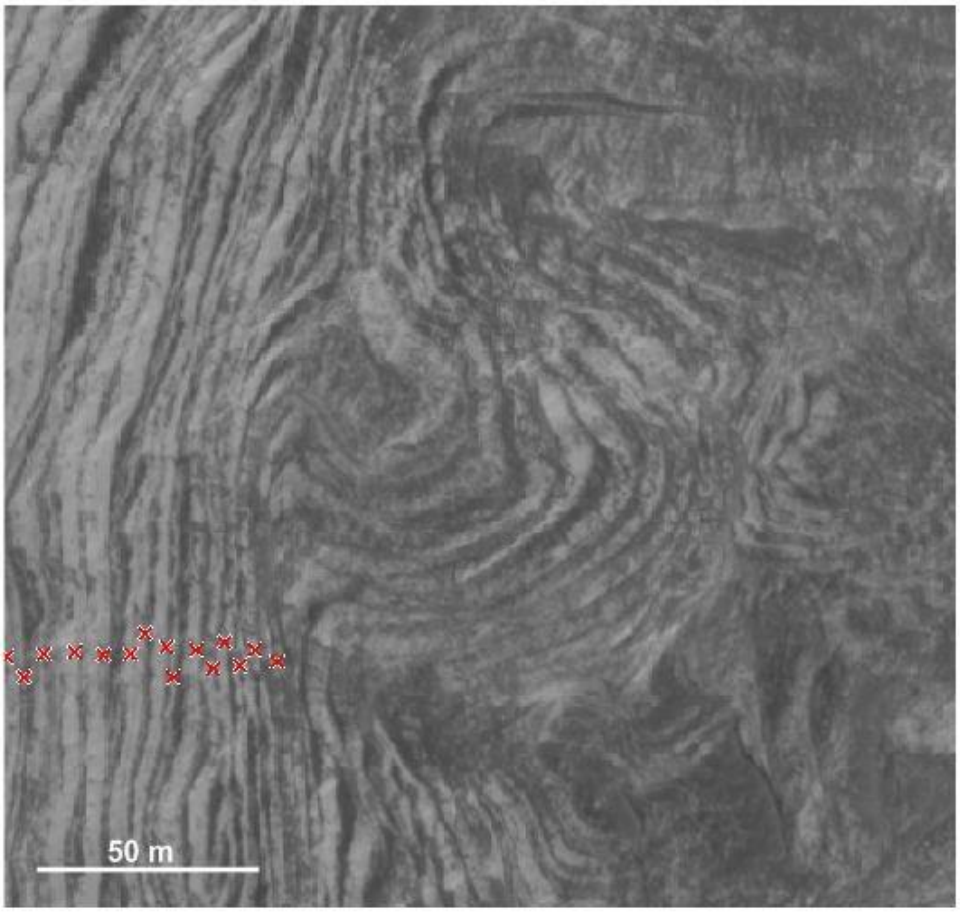

Figure 3.12: Additional site displaying a slump-like feature. Underlying layering was not disrupted at this site or others like it so the sites were therefore not included in the analysis.

3.5 Comparison of Previously Described Similar Features to those within Ganges Chasma

3.5.1 Martian Features

Within the chasms of VM, very few similar features have been identified. Within some of the VM deposits, post depositional modifications have occurred due to the offset of layering by faults [*Komatsu, et al.,* 2003]. In both Hebes and Juventae chasmata, possible slump structures have been reported that are comparable in size to the Ganges features [*Komatsu, et al.,* 2003]. The features in both locations have the same general u-shaped form as the Ganges features; however, they do not appear to disrupt or truncate the surrounding layers.

Two studies [*Okubo et al.,* 2009; *Guallini et al.,* 2013] conducted in two separate locations on the Mars surface provide evidence that features superficially resembling those in Ganges have been found. In both articles, primary and secondary features are identified and described. The primary features do not resemble those in Ganges; however, the secondary features as well as the controlling processes indicate similarities.

Guallini et al. [2013] focused on large scale deformation features found in the South Polar layered deposits of Mars and their implications for the deformational history of Mars. Unfortunately this conference abstract does not include images, making it difficult to judge similarities to our features. This zone of brittle-ductile shearing includes pillow and flame structures along with drag folds and faults. Based on the descriptions given, the ductile folds observed are comparable to soft sediment tectonic structures in numerous terrestrial settings.

In a study of structural discontinuities, or deformation bands, in the Arabia Terra region of Mars, Okubo et al. (2009) identify other features that resemble those in Ganges Chasma as soft sediment deformation. The Arabia Terra features indicate the presence of groundwater in early Martian history and that the sediments present were water-saturated and deformed before

lithification [*Okubo, et al.,* 2009]. Figure 3.13 depicts different deformation features present in Arabia Terra area [*Okubo, et al.,* 2009]. The soft sediment deformation features shown in Figure 3.13 are easily distinguishable from the surrounding topography and resemble those found in Ganges due to their u-shaped form and overall large scale. These soft sediment deformation features are referred to as "harmonic crenulations" [*Okubo, et al.,* 2009]. Although similar in appearance and size, the Ganges features are not believed to be harmonic crenulations. Like the Ganges features, harmonic crenulations occur on a multibed scale (metres +), are associated with fine grained materials, and are typically bound by undeformed units above and below [*Chan, et al.,* 2007]. However, harmonic crenulations generally occur in groupings and are typically not isolated like the Ganges features. Hence it is not likely that the Ganges features are harmonic crenulations.

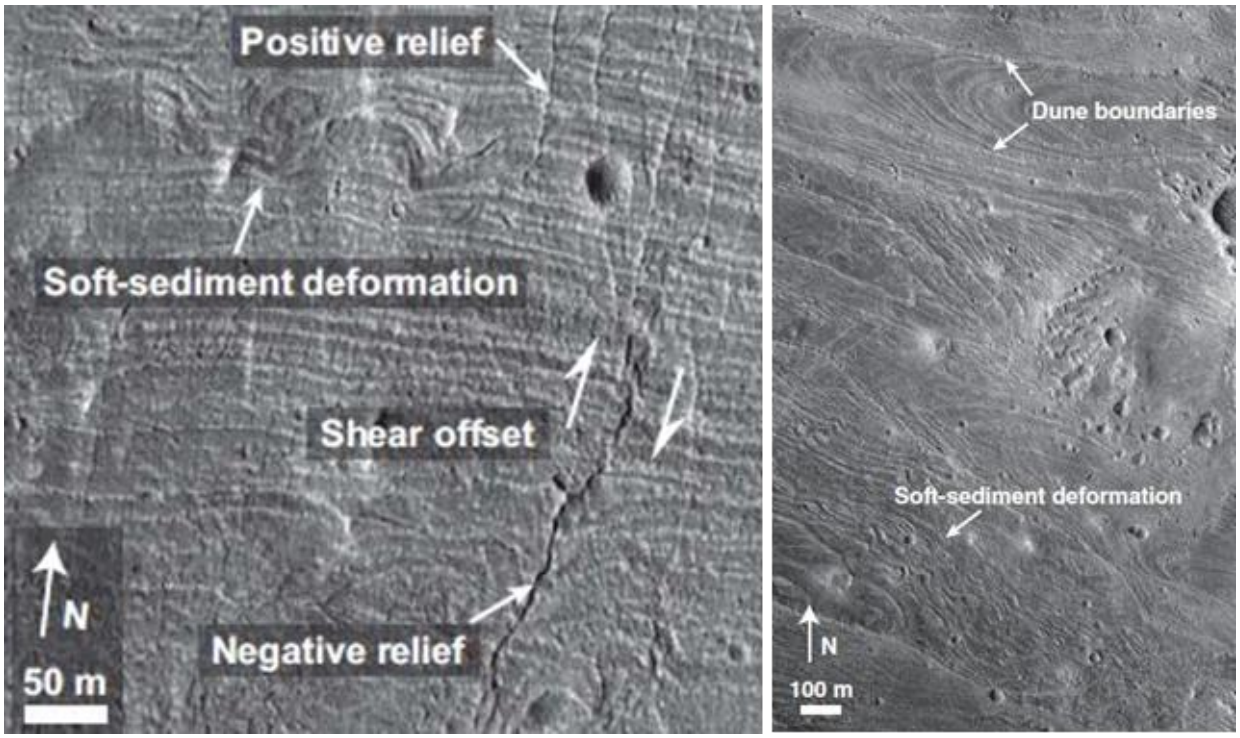

Figure 3.13: Soft Sediment Deformation present within Arabia Terra, Mars study site [Okubo, et al., 2009] Topography in both images is essentially flat and therefore the layer undulations are not expected to be due to topographic effects.

3.5.2 Terrestrial Features

Terrestrial analogs provide examples of slump features and soft sediment deformation features (Figure 3.14 A and B) that are similar to the features in Ganges Chasma (Figure 3.14 C and D). Figure 3.14 A is described as plastic deformation in contorted cross dune strata [*Chan, et al.*, 2007]. Contorted dune sets are constructed primarily from aeolian sediments, while, as discussed in chapter 2, there is no evidence for large quantities of aeolian sedimentation within the Ganges ILD mound. However, in appearance and size only, the contorted cross dune strata do resemble the Ganges features. Figure 3.14 B is classified as massive slump folding [*Gregory*, 1968]. The fracturing and crushing present in the Gregory [1968] feature is not evident in the Ganges features, likely due to differences in material properties.

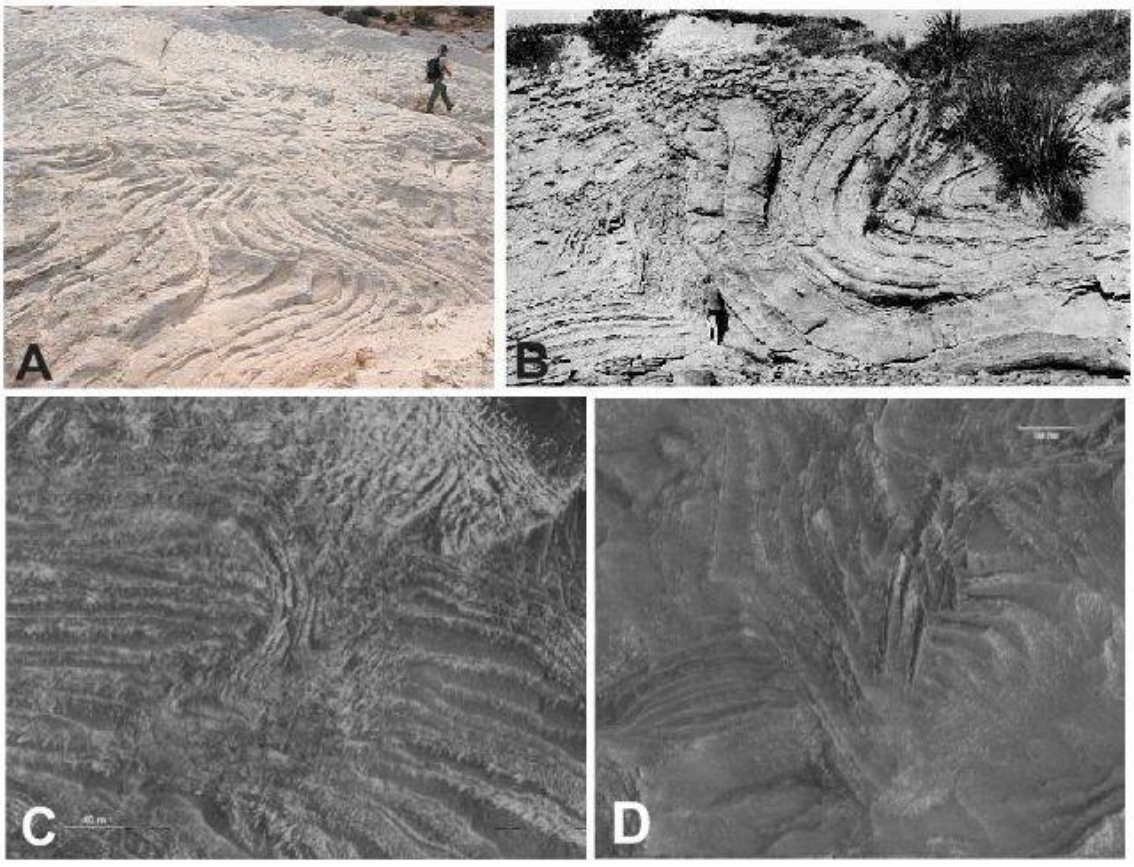

Figure 3.14: Comparisons of terrestrial features identified in the literature [A: *Chan, et al.*, 2007; B: *Gregory*, 1968] to the features identified in the Ganges ILD (C: Feature 1 & D: Feature 5).

In order to properly compare the terrestrial features to the Ganges features, a schematic cross section was constructed of the basic Ganges feature (Figure 3.7). The terrestrial features do not appear to be formed by the same mechanisms as the Ganges features (discussed in detail in section 3.6), but are still on the scale of 10's of metres and strongly resemble the Ganges features in overall appearance. These terrestrial examples are comparable to the Ganges features in appearance and size only; they do not appear to be comparable otherwise due to assumed differences in formation mechanisms.

In terrestrial settings, slumping can occur on very low slopes. Surface sediments (10-50 m thick) have slumped down bedding planes sloped at 1°- 4° [*Lewis*, 1971] suggesting that the sloping topography can be a controlling factor of slump direction and size even on shallow slopes. Additionally, there is evidence of slumping sediments 1-200 m thick in ancient submarine slopes of less than 5° [*Lewis*, 1971].

Along a continental slope in Israel, slump scars with widths up to 3 km and lengths up to 4 km were identified [*Almagor and Wiseman*, 1991]. Figure 3.15 depicts a bathymetric contour chart of these slumps. The topographic expressions of these features are currently large empty slump scars with a long dimension trending down the overall topographic slope.

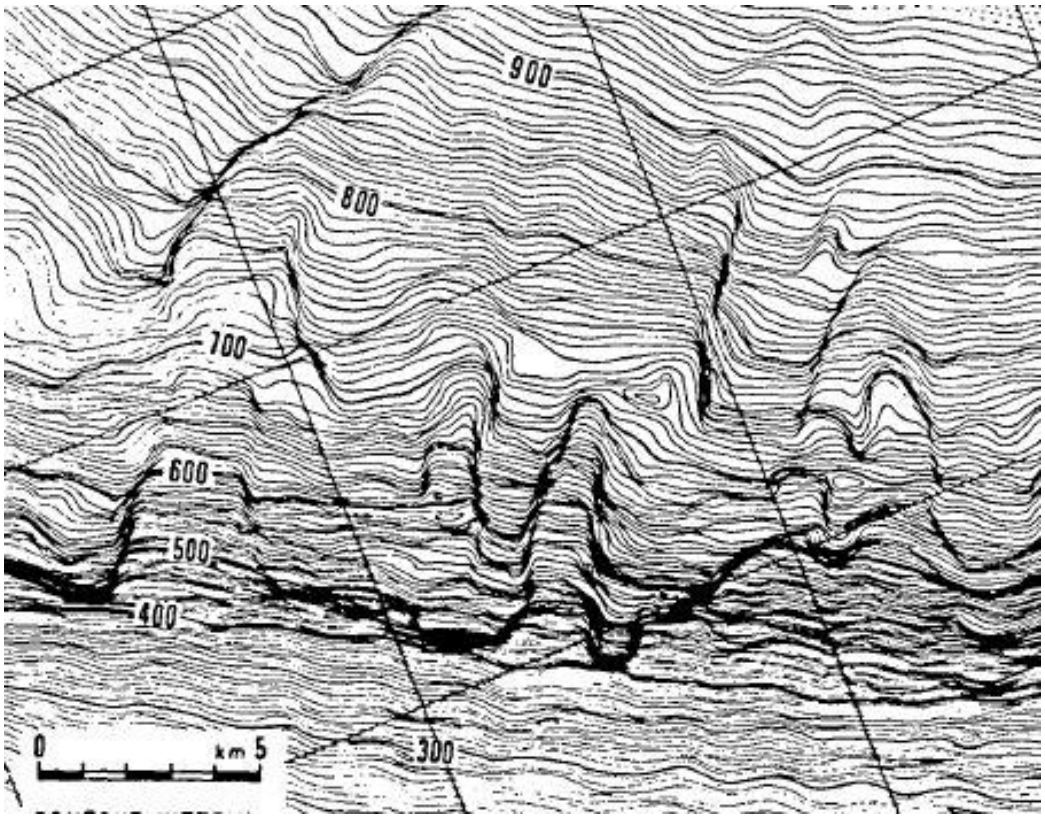

Figure 3.15: Bathymetric chart of the continental slope off southern Israel; 5 m contour interval (*Almagor and Wiseman*, 1991). The upward portion of the slope is the bottom of the image and points down towards the top of the image.

The slump scars have well defined boundaries and a steep slope wall of approximately 20º [*Almagor and Wiseman*, 1991]. The more recent slump scars found in Israel contain well-defined boundaries while the older scars are poorly preserved with hazy boundaries [*Almagor and Wiseman*, 1991]. These features are much larger in scale than other terrestrial analogs, and are generally larger than the Ganges features. Unlike the features identified on the Ganges ILD, which are isolated, the Israeli slumps can occupy up to 30% of the continental slope area and are found at water depths greater than 400 m [*Almagor and Wiseman*, 1991]. The Israeli slumps show the same general appearances and magnitudes as the channels of the features within Ganges, yet unlike the Ganges features, they are not filled with later sediments and occupy much larger areas. The Israeli features are on a tectonically active slope and the Ganges ILD was likely

deposited in a comparably tectonically active setting. It is unknown why the Ganges features are more isolated than the comparable Israeli features.

3.6 Discussion

The Almagor and Wiseman [1991] study on the Israeli slumps provides the closest examples to the channels observed in the Ganges features in both size and appearance (Figure 3.15). The Israeli slumps are found at great water depths (>400 m) and occupy a large amount of the continental slope area (up to 30%) [*Almagor and Wiseman*, 1991]. It is assumed that Ganges Chasma was occupied by standing water during formation of the ILD; the depth of the standing water is unknown, but due to the essentially horizontal and undisturbed layering of the ILD, it is presumed that the ILD sat below the wave-base of the standing water.

We suggest that the features identified on the Ganges ILD are filled in channels or slump scars, similar to those documented in Almagor and Wiseman [1991]. In this scenario, a three stage model for Ganges feature formation is proposed: 1) the formation of shallow erosional channels or troughs on the surface of the accreting ILD due to the erosion or slumping of sediments, 2) sediment deposition and draping of the eroded surface resulting in the infilling of the trough/channel, and 3) erosion of the ILD into current surface topography. These stages are represented by the schematic models in Figure 3.16.

To illustrate the model proposed, multiple tests were conducted using a modelling compound to visually represent the different stages of the feature formation. In the first stage, slumping or erosion of sediments on the ILD would have occurred through SSD and/or submarine slumping. This slumping would result in the erosion of u-shaped gullies, troughs and/or channels, similar to those seen in Almagor and Wiseman [1991] (Figure 3.17).

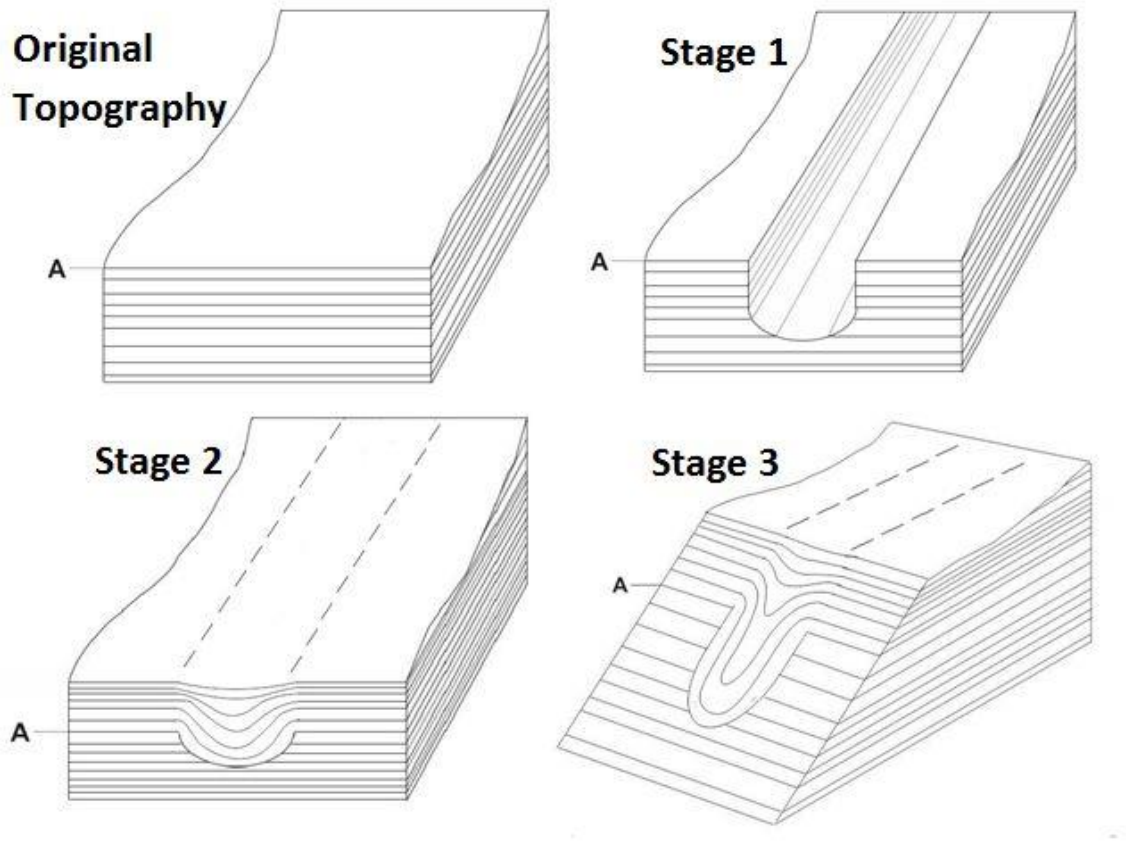

Figure 3.16: Schematic representation of the original topography and the 3 stages of the proposed feature formation model. Stage 1 is the formation of shallow, erosional channels; Stage 2 is the infilling of the channels with layered sediments; and Stage 3 is the erosion of the ILD to current surface topography.

After the troughs were formed, sediments were draped into the channel, filling the troughs with deposited sediment layers (Figure 3.18). Based on the consistent layer thicknesses in the enigmatic formations, it can be assumed that the same mechanisms that formed the initial layers also formed the layers that fill the gully formations. The way in which the layers conform to the channel walls is common in subaqeous channels (*Enos et al.*, 2008), and is referred to as an accretionary channel fill pattern (*Wen*, 2004). In the third stage, erosion of the feature to the current topographic slope was simulated by cutting the model, resulting in similar geometries as the features within Ganges (Figure 3.19).

Figure 3.17: Representation of the first stage of the proposed Ganges feature formation model. The normal layering (represented by the green, orange, white, purple and yellow modelling compound) undergoes slumping or erosion leading to the formation of gullies or channels.

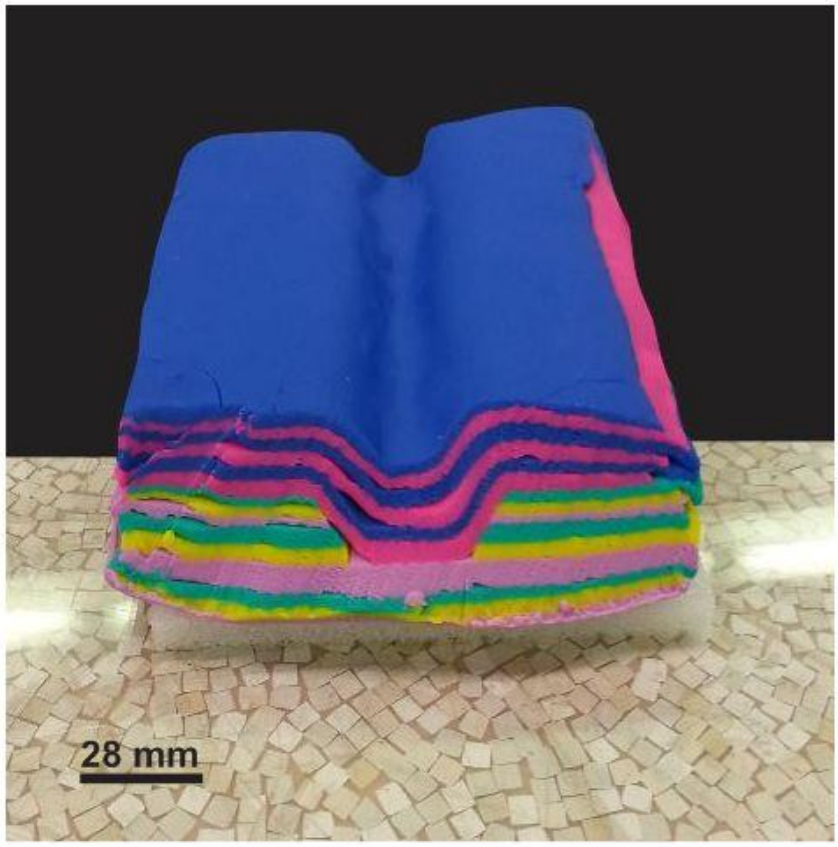

Figure 3.18: Representation of the second stage of the proposed formation model for the Ganges features. Green, purple and yellow modelling compounds represent the normal layering which was eroded into a channel; the pink and blue modelling compounds represent the sediments draped into the channel which form the Ganges features.

The model was cut at different angles to obtain different final geometries. In test 1, it is

assumed that the erosion that occurs after layer draping is in a consistent slope direction. The test 1 model was sliced multiple times at varying angles (40º, 30º, 15º, and 12º) to determine the resulting form at different topographic slopes (Figure 3.20). At all topographic angles, the model features had similar forms and were easily distinguished from the normal layering.

Figure 3.19: Representation of the third and final stage of the proposed Ganges feature model. After sediments are draped into the channels, the surface was eroded, resulting in the features currently observed.

As the tested angles became steadily shallower, the u-shaped form grew more stretched and altered (Figure 3.20). This model mimics the overall low topographic slope and flat topography present in the feature locations on the ILD.

Test 2 assumes non-consistent erosion occurred leading to a slight undulating topography (Figure 3.21). The result resembled two connecting formations facing one another (Figure 3.22), a geometry not seen among the Ganges features. However, similar topography variations may have led to the formation of the bi-directional forms (class 2) that were identified in Ganges. Additionally, remnants of multiple channels directly adjacent to one another and subsequently eroded and obscured in the same way as test 2 (similar to D and H in Figure 3.11) may have

resulted in the dual feature forms of class 2. Test 3 also assumes the occurrence of non-consistent erosion, leading to a dual bowl shaped profile (Figure 3.23).

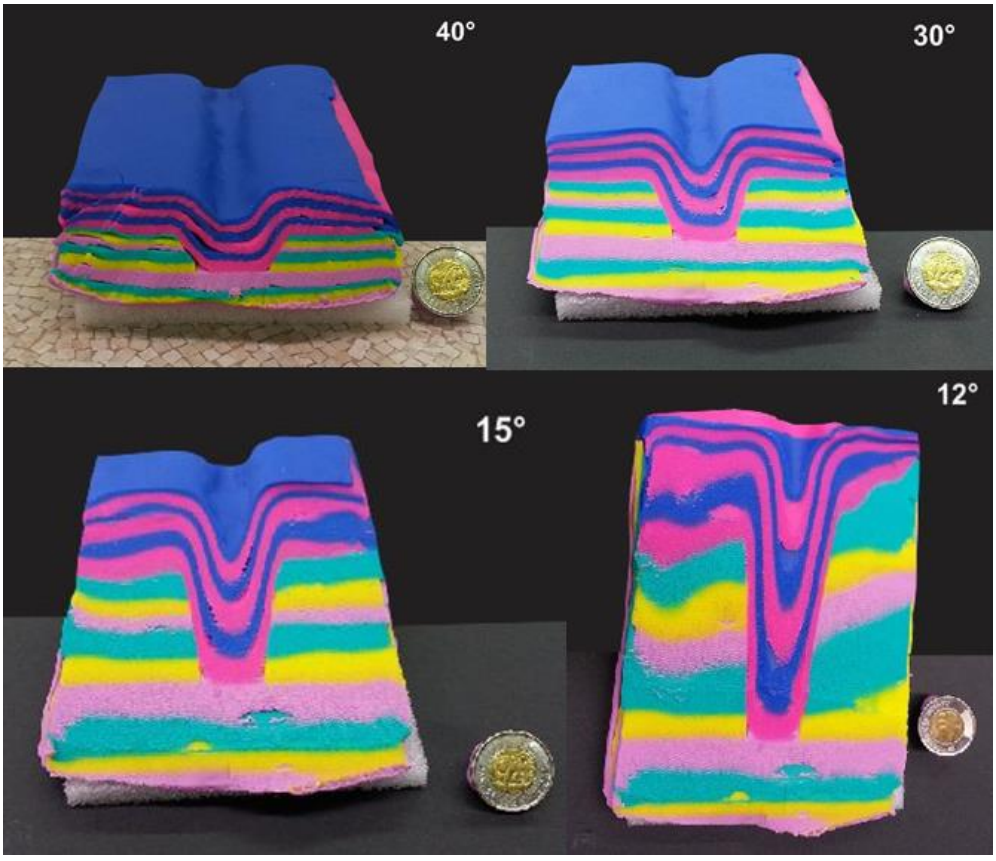

Figure 3.20: Resulting forms (test 1) at differing topographic slope angles. As the slope becomes progressively shallower, the forms became more stretched and distorted.

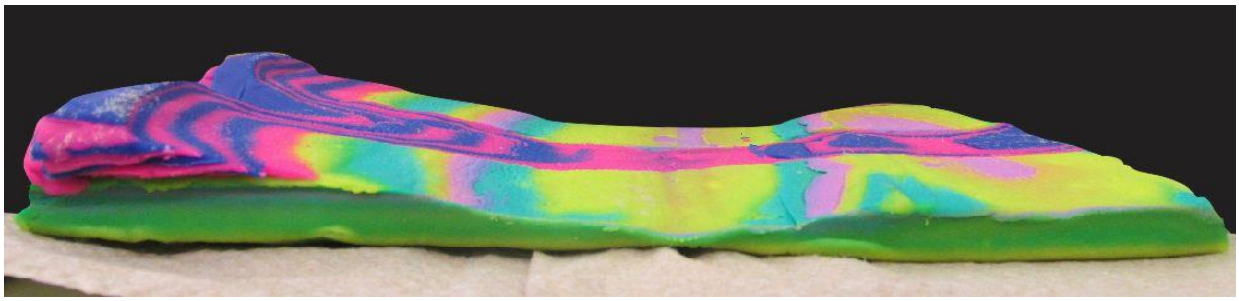

Figure 3.21: Representation of the profile view of test 2. The beginning of the profile erodes in a consistent manner; the central area experiences more erosion leading to the slight bowl appearance.

Figure 3.22: Plan view of the results from test 2.

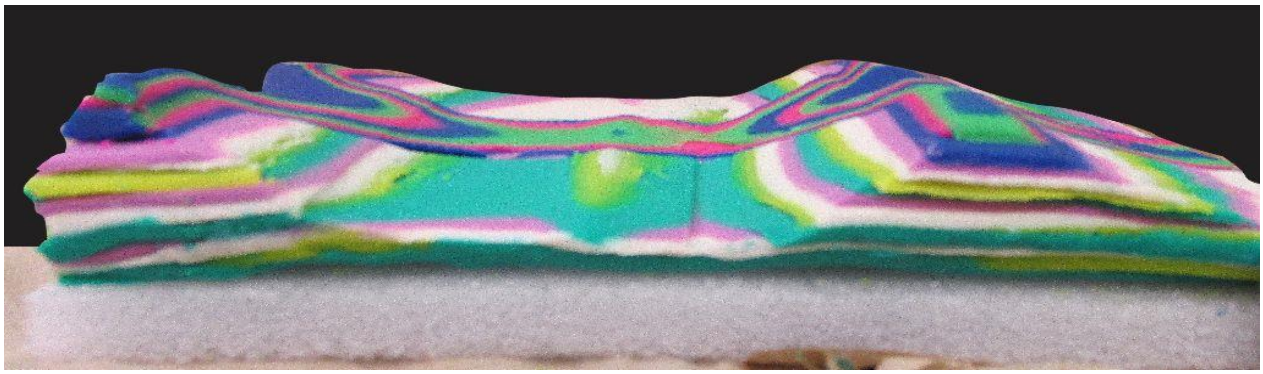

Figure 3.23: Representation of the profile view of test 3. The central areas experience more erosion leading to the dual bowl appearance. Two forms are created from this erosional method, orientated in the same direction (to the right of the image).

Once again, this topography resulted in dual formations occurring, this time both curving in the same direction (Figure 3.24). This result was also not observed in Ganges since all identified features were isolated from one another. However, if more erosion occurred between the two features, they could become isolated from one another, providing a possible explanation.

Figure 3.24: Plan view of the test 3 results.

3.6.1 Origins and Controls of Ganges Features

Terrigenous or pelagic slump and slide deposits are primarily formed in saturated sediments emplaced downslope through mass wasting processes [*Boggs*, 2001]. During the downslope movement, the slump layering is consistently disturbed, resulting in chaotic and contorted bedding and faulting [*Boggs*, 2001]. Channels or slump scars may be caused by large movements of mass wasted sediments [*Lewis,* 1971; *Almagor and Wiseman*, 1991] or by the

sliding of large chunks of sediments [*Almagor and Wiseman*, 1991]. Based on this data and the studies analyzed, we suggest that the Ganges features are filled channels or slump scars based on the curving nature of the feature layers, the disturbed layering surrounding each feature, and the overall u-shaped forms.

The overall form and composition of the Ganges features leads us to believe that soft sediment deformation is a probable mechanism for the formation of the original channels. Of the five main factors that contribute to the formation of soft sediment deformation features, liquefaction or fluidization [*Mills*, 1983], shear stresses [*Lewis*, 1971; *Mills*, 1983], and/or loosely packed/weak sediments [*Lewis*, 1971] are the most likely influences in the formation of the channels which led to the construction of the Ganges features. Liquefaction or fluidization processes are likely to have occurred due to the saturated conditions during ILD formation and emplacement, but it is unknown why the Ganges features are so isolated in nature. The large distance between Ganges Chasma and the center of the Tharsis Bulge may suggest that Tharsis related stresses played a role in the development of the Ganges features, but were not the primary influences. It is likely that significant localized shear stresses occurred during the infilling or subsidence phases of ILD development [*R. Stesky, Pers. Comm.*, 2014]. Based on the general North-South orientation of the features, localized tectonic activity, such as faulting, is a likely influence on the formation of the Ganges features. The mobilization of the sediments into these features could have also been a result of the critical amount of overburden pressure and corresponding pore pressure available [*R. Stesky, Pers. Comm.*, 2014]. Lastly, loosely packed sediments are known to constitute a large portion of ILD materials based on the presence of the dark capping layer and the presence of aeolian dune fields on the ILD.

The features in both Israel and New Zealand provide examples of features similar to those in Ganges in both appearance and size. The size and appearance similarities further strengthen the argument for standing water in Ganges Chasma, providing no tilting of the sediments occurred.

The Basic U-Shaped features do not appear to have size constraints due to the large range of sizes measured. The limited data available for Classes 2 and 3 do not allow for any conclusions to be drawn about possible size constraints.

Differences in erosion and infill mechanisms may have influenced the boundary appearance which is reflected in the definition between the first and third classifications. If in-filled with sediments rapidly after being created, the slump scar walls would remain fresh and would show distinct boundaries like those seen in the first classification (Basic U-Shaped). If the infilling of sediments occurred after a hiatus in deposition, or at a slower pace, the walls would have time to erode and degrade, resulting in the hazy boundaries seen in the third classification (Minimal/Understated). The features in the third classification most likely underwent larger amounts of erosion during the infilling process, leading to less distinct boundary definitions compared to the first and second classification features.

The identification of the features at distinct elevations and locations with respect to benches could indicate numerous controls: elevation or slope controls, identification issues, or overburden pressure. Slumping can occur on a large variety of slopes; shallow slopes can just as easily form slump features [*Lewis*, 1971] as steep slopes, indicating that these features may not be dictated by slope controls. However, since the long axes of the features approximately parallel the measured dip directions, it is possible that the estimated paleo-slope influenced feature formation.

The dark mesa unit largely found at the higher elevations of the ILD above bench 3 can obscure topographic and erosional features [*Malin and Edgett,* 2000] (Figure 3.8). It may be that sedimentary features exist above bench 3 but cannot be identified due to the large portion of the dark mesa layer present.

3.7 Conclusions

The enigmatic isolated features identified within the Ganges ILD are characterized by u-shaped channels cut into underlying layering. Comparisons to terrestrial and martian analogs led to identifying these features as filled slump scars or channels. Liquid water was likely present during feature formation.

After the sediment slumping and channel cutting occurred on the Ganges ILD, it is suggested that the channels were abruptly abandoned or channel cutting no longer occurred, quickly in-filled by draping sediments, and subsequently eroded to form the current topography. Of the three models presented, the first appears to be most accurate. In test 1, the features, as well as the surrounding topography, resemble the Ganges formations well. In test 1, the features became narrower in plan view down slope which contrasts with many of the actual Ganges features. The thicker layering at the bottom of the features observed in plan view could be due to different erosional patterns or inconsistent channel formations. In the tests, the channel created was linear and even, resulting in the consistency of the features.

Similar features are not identified in the Mars literature. The Ganges features maybe the first major slump-like features found on the Martian surface, especially in the VM region. A subaqueous slumping formation mechanism indicates that during the time that Ganges ILD was formed, the chasm would have been an ancient lake or a lake network.

3.7.1 Limitations and Assumptions with Research and Data

The features identified in Ganges Chasma suggest past water activity; yet the limited number of features found does not provide a large database to work with. Obtaining a larger data set within Ganges Chasma by acquiring further HiRISE coverage would help to substantiate patterns, correlations, and conclusions for any scientific study. For this study, it would have been optimal to have more identified slump features to analyze (20+). The larger data set would have made it easier to identify patterns such as elevation-width relationships, as well as expanding on possible elevation and/or bench controls. Expanding the study area to other VM ILDs could conclude whether or not these features occur throughout VM or are confined to the Ganges Chasma.

The literature and research studied throughout the analysis helped to provide martian and terrestrial comparisons with the Ganges slumps, but there were limitations. Few articles focused on the martian surface, with no Ganges Chasma focus. The Earth-based analogs provided possible deformational mechanisms. These mechanisms gave a base understanding of how deformation features are formed; however, without further Mars-based research, it is unknown whether the same processes occur on Mars or if they would result in the same formations.

3.7.2 Future Research

Further research would require analysis of additional HiRISE images that cover the Ganges ILD and additional areas of Mars. If more images were analyzed, it is possible that more features could be identified, enlarging the current database and thereby allowing for additional correlations to be made. If similar features are found in additional areas of Mars, a better understanding of the overall sedimentary record of Mars could be drawn.

In additional studies, the features that resembled the sedimentary features in appearance but did not disrupt the surrounding layering (Figure 3.11) should also be analyzed. These features were not included in this study because they did not appear to truncate or disrupt the underlying layering, but the overall appearance of these features did mimic the twelve features discussed in this report. It is possible that these additional features formed through the same methods as the features discussed in this study, but further research will have to be conducted for conclusions to be drawn.

3.8 References

Almagor, G., and G. Wiseman. (1991). Analysis of submarine slumping in the continental slope off the southern coast of Israel, *Marine Geotechnology, 10: 3-4*, 303-342.

Blue Marble Geographics. (1993-2014). *Global Mapper, LLC [computer software]*. Developed by Mike Childs in 2011, Gardiner, Maine.

Boggs, S. (2001). *Principles of Sedimentology and Stratigraphy (3rd Ed.)*. Upper Saddle River, New Jersey: Prentice-Hall Inc.

Broxton, M. J. and L. J. Edwards (2008). The Ames Stereo Pipeline: Automated 3D Surface Reconstruction from Orbital Imagery, *Lunar Planet Sci. XXXIX*, Abstract 2419.

Chan, M., D. Netoff, R. Blakey, G. Kocurek, and W. Alvarez. (2007). Clastic-injection Pipes and Syndepositional Deformation Structures in Jurassic Eolian Deposits: Examples from the Colorado Plateau, in *Sand Injectites: Implications for Hydrocarbon Exploration and Production*, pp. 233 – 244, AAPG Memoir.

Chojnacki, M., and B.M. Hynek. (2008). Geological Context of Water-Altered Minerals in Valles Marineris, Mars, *Journal of Geophysical Research, 113*, E12005, doi: 10.1029/2007JE003070.

Corel. (1989-2014). *CorelDRAW Graphics Suite X7 [computer software]*. Ottawa, Ontario, Canada.

Enos, P., R.D. Jefferson, and S.L. Goetz. (2008). Channels Ran Through It: The Lawrence Formation at Lone Star Lake, Douglas County, Kansas, *Kansas Geological Survey, Current Research in Earth Sciences, 254,* part 1.

Fueten, F., R.M. Stesky, and P. MacKinnon. (2004). Structural Attitudes of Large Scale Layering in Valles Marineris, Mars, Calculated from Mars Orbiter Laser Altimeter Data and Mars Orbiter Camera Imagery, *Icarus, 175*, 68-77, doi: 10.1016/j.icarus.2004.11.010.

Glennie, K. and A. Hurst. (2007). Fluidization and Associated Soft-sediment Deformation in Eolian Sandstones: Hopeman Sandstone (Permian), Scotland, and Rotliegend, North Sea, in *Sand Injectites: Implications for Hydrocarbon Exploration and Production,* pp. 245-252, AAPG Memoir 87.

Gregory, M.R. (1968). Sedimentary Features and Penecontemporaneous Slumping in the Waitemata Group, Whangaparaol Peninsula, North Auckland, New Zealand, *New Zealand Journal of Geology and Geophysics, 12*, 248-282.

Grotzinger, J.P. and R.E. Milliken. (2012). The Sedimentary Rock Record of Mars: Distribution, Origins, and Global Stratigraphy, in *Sedimentary Geology of Mars,* pp. 1-48, Society for Sedimentary Geology (SEPM), Oklahoma.

Guallini, L., F. Brozzetti, and L. Marinangeli. (2013). "Soft Sediment" and Deep-Seated Gravitational Slope Deformations Mechanisms in the South Polar Layered Deposits (Promethei Lingula, Mars): Geological and Climatic Implications, *Lunar Planet Sci. XLIV,* Abstract 1480.

Harland, D.M. (2005). *Water and the Search for Life on Mars,* Praxis Publishing, New York.

Ismailos, C., F. Fueten, R. Stesky, J. Flahaut, A. Rossi, and E. Hauber. (2012). Layer Thickness Determination of the Interior Layered Deposit within Ganges Chasma, Mars, *Lunar Planet. Sci. XLIII,* Abstract 1533.

Komatsu, G., G.G. Ori, P. Ciarcelluti, and Y.D. Litasov. (2003). Interior Layered Deposits of Valles Marineris, Mars: Analogous Subice Volcanism Related to Baikal Rifting, Southern Siberia, *Planetary and Space Science, 52,* 167-187, doi: 10.1016/j.pss.2003.08.003.

Lewis, K.B. (1971). Slumping on a Continental Slope Inclined at 1°- 4°. *Sedimentology, 16,* 97-110.

Lowe, D.R. (1975). Water Escape Structures in Coarse Grained Sediments. *Sedimentology, 22,* 157-204.

Lucchitta, B.K., N.K. Isbell, and A. Howington-Kraus. (1994). Topography of Valles Marineris: Implications for Erosional and Structural History, *Journal of Geophysical Research,99 (E2),* 3783-3798.

Malin, M.C., and K.S. Edgett. (2000). Sedimentary Rocks of Early Mars, *Science, 290,* 1927-1937, doi: 10.1126/science.290.5498.1927.

Microsoft Corporation. (2010). *Microsoft Office: Excel [Computer Software*]. Redmond, Washington.

Mills, P.C. (1983). Genesis and diagnostic value of soft-sediment deformation structures- A review, *Sedimentary Geology, 35,* 83-104.

Moratto, Z. M., M. J. Broxton, R. A. Beyer, M. Lundy, and K. Husmann (2010) Ames Stereo Pipeline, NASA's Open Source Automated Stereogrammetry Software, *Lunar Planet. Sci. XLI,* Abstract 2364.

Okubo, C.H., R.A. Schultz, M.A. Chan, G. Komatsu, and HiRISE Team. (2009). Deformation band clusters on Mars and Implications for Subsurface fluid flow, *Geological Society of America Bulletin, 121,* 474-482.

Pangaea Scientific (2006-2011). *Orion: Orientation Hunter [computer software]*. Supported by Canada Centre for Remote Sensing, Natural Resources Canada. Brockville, Ontario, Canada.

Tanaka, K.L. (1997). Origin of Valles Marineris and Noctis Labyrinthus, Mars, by Structurally Controlled Collapse and Erosion of Crustal Materials, *Lunar Planet. Sci. XXVIII*, Abstract 1169.

Wen, R. (2004). 3D Modeling of Stratigraphic Heterogeneity in Channelized Reservoirs: Methods and Applications in Seismic Attribute Facies Classification, *CSEG Recorder*, 29, N. 03.

Chapter 4: Overall Conclusions

4.1 Focus of Study

Analyses of the Ganges Interior Layered Deposit (ILD) have provided data for several possible new interpretations about the formation and evolution of the ILDs within Valles Marineris (VM). The investigation of layer attitudes and thicknesses, mineralogy, and deformational features in Chapter 2 revealed correlations between layering and elevation, bench morphology, and mineralogy. Chapter 3 investigated the irregular features seen throughout the Ganges ILD and hypothesized a formation mechanism for the development of the features.

4.2 Chapter 2 Conclusions

Layering is overall shallow and parallel, with dips generally coinciding with the downslope direction of the ILD. This indicates that the layers strike parallel the East-West orientated VM system and dip in primarily northerly and southerly directions. The general down slope dipping of ILD layers as well as the greater layer dips observed at the lower elevations suggests the draping of sediments over basement topography. Maximum dip decreased with increased elevation in the ILD indicating that layering becomes increasingly shallow at higher elevations and suggests the infilling of a basin with sediments.

Compared to other VM chasma, the layering within Ganges is consistently thin throughout the ILD with an average thickness of less than 2 m. The thickest layers identified were primarily found along the bench edge topography. A minor thinning of layers is observed at higher elevations. The thinner layers observed in Ganges Chasma could either be attributed to rapid depositional events or to a reduced volume of sediment influx.

Variations in elevation of the lower two benches (1 and 2) support draping, while the highest bench (3) is consistent with the infill of sediments based on the horizontal nature of the

bench. The benches parallel the measured ILD layering; however, the benches cannot be attributed to single layers. Moving average calculations of layer thickness indicate that an increase in thickness of ILD layers coincide with the ILD benches.

The large anomalous topographic features formed after ILD emplacement. Since bench morphology governs the length of the features as well as feature direction, it is assumed that the features were formed before erosion of the surface sediments. The visual appearances and linear natures of the features closely resemble dike formations but the north-south trend of the features runs perpendicular to the overall east-west trend of VM.

The different mineralogical compositions found throughout the ILD appear to correlate to the benches. The lower elevations of the ILD at the first and second benches are dominated by monohydrated sediments (MHS); the upper elevations of the ILD where the third bench is located were dominated by polyhydrated sediments (PHS). The PHS composition of bench 3 could be more resistant to erosional mechanisms, leading to the more sharply defined edges observed.

The wide presence of sulfate and water-altered minerals suggests the presence of lacustrine or snowmelt mechanisms during ILD formation. These mechanisms correlate well with the hypothesis of liquid filled basins prior to ILD formation proposed by Lucchitta et al. [1994]. Periodic melting of the lake surface could have also occurred, resulting in seasonal melting and deposition of trapped sediments. The thick layer packages seen at the bench locations could have been a result of substantial hiatus' in seasonal melts and deposited sediments.

4.3 Chapter 3 Conclusions

In Chapter 3, 12 enigmatic sedimentary features were identified and analyzed. All 12 features are isolated, large scale, and characterized by u-shaped channels. These features were identified as filled slump scars. The proposed formation model for the Ganges slump scars is a three stage process. These stages are: 1) the formation of shallow erosional channels or troughs on the surface of the accreting ILD due to the erosion or slumping of sediments, 2) sediment deposition and draping of the eroded surface resulting in the infilling of the trough/channel, and 3) erosion of the ILD into current surface topography. For these stages to occur, the ILD would have been submerged under water by a lake that filled the chasma. The erosion or slumping of sediments occurred under the wave base of the lake-filled chasma, leading to the formation of u-shaped gullies or troughs. These troughs were then infilled with deposited layers of sediments, which were draped into the trough. Lastly, after the lake was drained from the chasma, the surface sediments and enigmatic features were eroded to the current topography, resulting in the shallow features. Several tests were conducted with coloured modelling compound and it was determined that the resulting features of the model were visually similar to those identified on the Ganges ILD.

Differences in erosional and infill mechanisms could have led to the variations in boundary definitions between the three different feature classifications. If the draping of sediments occurred quickly in the gully formations, the feature boundaries would be well maintained and distinct from surrounding layering. However, if the walls of the gullies were eroded substantially before sediment deposition, more diffuse boundaries could develop.

The proposed model covers and explains the different aspects of the Ganges features, but would only work if located in a lacustrine setting with large amounts of water in liquid form or periodically frozen [*Glennie and Hurst,* 2007; *Koç Taşgın, et al.,* 2011].

4.4 Conclusions

Currently, the equatorial region of Mars does not have liquid or ice water at the surface, but past infilling of liquid water or periodic melting of a frozen lake in an enclosed basin at the time of ILD formation is highly likely. Periodic melting, or seasonal melts, could result in the formation of the thin, shallow layers seen throughout the ILD from sediments trapped in ice. Substantial melting hiatuses over time, massive melting periods, or varying water levels may explain the thicker layers observed at ILD benches. The thick layer packages indicate that multiple large-scale depositional events occurred during the formation of the Ganges ILD.

The presence of water-altered minerals as well as the enigmatic slump features required the presence of water. Without the presence of water, these minerals and features would not be present and therefore further support the theory where Ganges Chasma was once filled with water in early Martian history. The variability of features seen throughout the ILD indicates multi-stage deformation of the Ganges ILD where sediment influx varied over time.

This research aimed to further the understanding of the history of VM, specifically by examining the formation of the ILD within Ganges Chasma. Strong evidence was found for formation within a lacustrine environment. The thin layering and present mineralogy is highly indicative of lacustrine origins. Additionally, deformation features on the ILD surface suggest the presence of water during the erosion and alteration stages of the ILD.

With this research, a basic theory for the formation of the Ganges Chasma ILD can be drawn. The Ganges Chasma was most likely filled with a lake, in either a liquid or frozen state,

during early VM formation. During periodic sediment deposition, the thin layering found throughout the ILD was created, with substantial hiatus' resulting in the three benches identified (Chapter 2). The water present from the lake-filled chasma allowed for the slumping and deformation of surface sediments into the slump scars discussed in Chapter 3. After trough opening and after the wet period of VM ended, the ILD sediments cemented in place which allowed for erosion and shaping of the ILD sediments to occur. Lastly, the dark, unconsolidated capping material was aerial deposited from external sources, blanketing the ILD. Overall, this study indicates a multi-stage formation model for the Ganges ILD. A first stage dominated by lacustrine or glacial processes resulting in the deposition of the ILD sediments, a second stage dominated by saturated sediment deformation under the wave base of the lake-filled chasma resulting in the enigmatic feature formations, and a third stage dominated by chasma drainage and aerial deposited sediments.

The large scale cycles observed are highly significant due to their repetitive nature, isolation to Ganges Chasma, and resulting competent benches not seen elsewhere in VM. These cycles make the Ganges ILD a very interesting and significant study site when analyzing VM formation mechanisms.

4.5 References

Boggs, S. (2001). *Principles of Sedimentology and Stratigraphy (3rd Ed.)*. Upper Saddle River, New Jersey: Prentice-Hall Inc.

Glennie, K. and A. Hurst. (2007). Fluidization and Associated Soft-Sediment Deformation in Eolian Sandstones: Hopeman Sandstone (Permian), Scotland, and Rotliegend, North Sea, in *Sand Injectites: Implications for Hydrocarbon Exploration and Production,* pp. 245-252, AAPG Memoir 87.

Koç Taşgın, C., H. Orhan, I. Türkmen, and E. Aksoy. (2011). Soft-Sediment Deformation Structures in the Late Miocene Şelmo Formation around Adiyaman area, Southeastern Turkey, *Sedimentary Geology, 235,* 277-291.

Lucchitta, B.K., N.K. Isbell, and A. Howington-Kraus. (1994). Topography of Valles Marineris: Implications for Erosional and Structural History, *Journal of Geophysical Research,99 (E2),* 3783-3798.